

AD \_\_\_\_\_

Award Number: DAMD17-96-1-6131

TITLE: Vascular Functional Imaging and Physiological Environment  
of Hyperplasia, Non-Metastatic and Metastatic Breast  
Cancer

PRINCIPAL INVESTIGATOR: Zaver Bhujwalla, Ph.D.

CONTRACTING ORGANIZATION: Johns Hopkins University  
Baltimore, Maryland 21205-2196

REPORT DATE: October 1999

TYPE OF REPORT: Annual

PREPARED FOR: U.S. Army Medical Research and Materiel Command  
Fort Detrick, Maryland 21702-5012

DISTRIBUTION STATEMENT: Approved for public release;  
distribution unlimited

The views, opinions and/or findings contained in this report are  
those of the author(s) and should not be construed as an official  
Department of the Army position, policy or decision unless so  
designated by other documentation.

20001121 066

DTIC QUALITY INSPECTED 4

Public reporting burden for this collection of information is estimated to average 1 hour per response, including the time for reviewing instructions, searching existing data sources, gathering and maintaining the data needed, and completing and reviewing this collection of information. Send comments regarding this burden estimate or any other aspect of this collection of information, including suggestions for reducing this burden to Washington Headquarters Services, Directorate for Information Operations and Reports, 1215 Jefferson Davis Highway, Suite 1204, Arlington, VA 22202-4302, and to the Office of Management and Budget, Paperwork Reduction Project (0704-0188), Washington, DC 20503

<b>1. AGENCY USE ONLY (Leave blank)</b>	<b>2. REPORT DATE</b> October 1999	<b>3. REPORT TYPE AND DATES COVERED</b> Annual (1-Oct-98 - 30-Sep-99)
<b>4. TITLE AND SUBTITLE</b> Vascular Functional Imaging and Physiological Environment of Hyperplasia, Non-Metastatic and Metastatic Breast Cancer		<b>5. FUNDING NUMBERS</b> DAMD17-96-1-6131
<b>6. AUTHOR(S)</b> Zaver Bhujwalla, Ph.D.		
<b>7. PERFORMING ORGANIZATION NAME(S) AND ADDRESS(ES)</b> Johns Hopkins University Baltimore, Maryland 21205-2196		<b>8. PERFORMING ORGANIZATION REPORT NUMBER</b>
<b>E-MAIL:</b> zaver@mri.jhu.edu		
<b>9. SPONSORING / MONITORING AGENCY NAME(S) AND ADDRESS(ES)</b> U.S. Army Medical Research and Materiel Command Fort Detrick, Maryland 21702-5012		<b>10. SPONSORING / MONITORING AGENCY REPORT NUMBER</b>
<b>11. SUPPLEMENTARY NOTES</b>		
<b>12a. DISTRIBUTION / AVAILABILITY STATEMENT</b> Approved for public release; distribution unlimited		<b>12b. DISTRIBUTION CODE</b>
<b>13. ABSTRACT (Maximum 200 Words)</b>		
<p>Our technological developments of obtaining multi-slice data together with our novel software program for image analysis have allowed us to obtain comprehensive information of tumor vascular volume and permeability as well as histological morphology and examine the relationship between vascular volume and permeability. In year 3 we have used the significant technical developments implemented in year 2 to determine the vascular characteristics of human breast cancer cells preselected for differences in invasive and metastatic behavior. The results obtained demonstrate that the more metastatic cell lines are characterized by higher vascular volume and vascular permeability <i>in vivo</i>. The analysis was performed for regions of high vascular volume and permeability. We also confirmed our earlier observations that regions of high vascular volume and regions of high vascular permeability do not coincide spatially. The results indicate a potential use of MRI for evaluating 'metastatic risk' noninvasively.</p>		
<b>14. SUBJECT TERMS</b> Research, Breast Cancer, vascularization, Magnetic Resonance Imaging, metastasis		<b>15. NUMBER OF PAGES</b> 20
		<b>16. PRICE CODE</b>
<b>17. SECURITY CLASSIFICATION OF REPORT</b> Unclassified	<b>18. SECURITY CLASSIFICATION OF THIS PAGE</b> Unclassified	<b>19. SECURITY CLASSIFICATION OF ABSTRACT</b> Unclassified
		<b>20. LIMITATION OF ABSTRACT</b> Unlimited

NSN 7540-01-280-5500

Standard Form 298 (Rev. 2-89)  
Prescribed by ANSI Std. Z39-18  
298-102

FOREWORD

Opinions, interpretations, conclusions and recommendations are those of the author and are not necessarily endorsed by the U.S. Army.

       Where copyrighted material is quoted, permission has been obtained to use such material.

       Where material from documents designated for limited distribution is quoted, permission has been obtained to use the material.

       Citations of commercial organizations and trade names in this report do not constitute an official Department of Army endorsement or approval of the products or services of these organizations.

X In conducting research using animals, the investigator(s) adhered to the "Guide for the Care and Use of Laboratory Animals," prepared by the Committee on Care and use of Laboratory Animals of the Institute of Laboratory Resources, national Research Council (NIH Publication No. 86-23, Revised 1985).

X For the protection of human subjects, the investigator(s) adhered to policies of applicable Federal Law 45 CFR 46.

N/A In conducting research utilizing recombinant DNA technology, the investigator(s) adhered to current guidelines promulgated by the National Institutes of Health.

N/A In the conduct of research utilizing recombinant DNA, the investigator(s) adhered to the NIH Guidelines for Research Involving Recombinant DNA Molecules.

N/A In the conduct of research involving hazardous organisms, the investigator(s) adhered to the CDC-NIH Guide for Biosafety in Microbiological and Biomedical Laboratories.

3

PL - Signature

Date

*Ram M. Bhujwala* Oct. 29, 1999

## **TABLE OF CONTENTS**

	<u>Page No.</u>
<b>1. FRONT COVER</b>	1
<b>2. STANDARD FORM (SF) 298, REPORT DOCUMENTATION PAGE</b>	2
<b>3. FOREWORD</b>	3
<b>4. TABLE OF CONTENTS</b>	4
<b>5. INTRODUCTION</b>	5
<b>6. BODY</b>	6
<b>7. CONCLUSIONS</b>	15
<b>8. KEY RESEARCH ACCOMPLISHMENTS</b>	16
<b>9. REPORTABLE OUTCOMES</b>	17
<b>10. REFERENCES</b>	19
<b>11. APPENDICES</b>	21

## INTRODUCTION

Vascularization plays a key role in the growth and metastasis of solid tumors [1-6]. In two recent clinical studies, breast cancer patients whose tumors had a high vascular density subsequently went on to develop metastases over a follow up period of 2.5 years [7, 8]. Statistical analyses of these patients showed that vascular density was the single most important factor ( $p<0.006$ ) associated with subsequent formation of metastasis [8]; the other factors examined were epidermal growth factor receptor status ( $p<0.01$ ), node status ( $p<0.02$ ), estrogen receptor status ( $p<0.05$ ), tumor size ( $p<0.06$ ), tumor grade ( $p<0.5$ ), c-erb-2 expression ( $p<0.7$ ), p53 ( $p<0.8$ ) and tumor type ( $p<0.8$ ). Studies correlating vascularization with metastasis have so far been performed with histological evaluation of excised tissue specimens [7, 8] as a result of which information regarding functioning of vessels is lost. Similarly, the physiological environment of these tumors, in terms of acidity and lactate production remains unknown. Thus a lack of noninvasive methods has left some vital questions about the precise nature of the relationship between vascularization and metastasis unanswered. Tumor neovascularization is induced by the secretion of angiogenic factors which act as chemotactic factors and mitogens for endothelial cells [1, 4-6]. One of the most potent of these is vascular endothelial growth factor (VEGF). VEGF also increases vascular permeability which in turn may allow cancer cells greater access to the vasculature [9]. In glioblastoma multiformae areas of necrosis and hypoxia show a higher expression of VEGF [10, 11]. Poorly functioning vessels and the associated hypoxia and necrosis may play a role in attracting further vascularization. Areas of hypoxia are also associated with accumulation of lactate and low pH. These two physiological factors attract neovascularization by stimulating the secretion of angiogenic factors from macrophages [12-15]. The secretion of enzymes which degrade the basement membrane in the metastatic process increases at low pH [16, 17]. Thus, vascularization, the physiological environment, and formation of metastases are highly interdependent. An understanding of the role of the physiological environment in vascularization and metastasis, and the dependence of this environment on metastatic phenotype are essential to delineate the relationship between vascularization and metastasis. Questions which are central to understanding this relationship are - (1) does the metastatic phenotype induce a higher degree of vascularization and is this mediated by modulation of the physiological environment ? (addressed in Specific Aims 1 and 3) (2) If so, do nonmetastatic tumors and preneoplastic tissue exhibit proportionately lower vascularization ? (addressed in Specific Aims 1 and 2) (3) Which particular property of the vascularization e.g. permeability, or vascular volume is the dominant factor in the dependence of metastasis on vascularization ? (addressed in Specific Aims 1 and 2) (4) Is a significant fraction of the vessels observed in the histological studies non-functional and does the resultant unsuitable environment induce expression of signals or substances which prompt and enable the cells to metastasize ? (addressed in Specific Aim 1). The overall goal of this research proposal is to use noninvasive Magnetic Resonance (MR) Imaging (I) and Spectroscopy (S) to answer the questions posed above.

## **BODY**

- The research proposed consists of three closely related aims designed to unravel the complex relationship between vascularization and metastasis. Our overall goal in this project is to determine key vascular and physiological properties which result in the close relationship between vascular density and metastasis as this information may ultimately be used to prevent tumor metastasis. We had proposed the following three aims:

Aim 1: To investigate the relationship between metastatic phenotype and the development of vascularization and evaluate the functionality of the developing vascularization in terms of vascular volume, vascular permeability and relative perfusion.

Hypothesis #1: More metastatic lines will exhibit a higher level of vascularization and permeability for similar volumes. A significant number of vessels detected by immunoperoxidase staining will not be functional and this number will increase with the size of the tumor.

Aim 2: To investigate the effect of increasing (a) tumor vascularization and (b) tumor vascularization and permeability on the formation of metastases.

Hypothesis #2: Higher vascularization and permeability will lead to an increase or an earlier incidence of metastases for all the lines.

(Aims 1 and 2 are related to questions 1-4 outlined in background)

Aim 3: To determine the relationship between metastatic phenotype and intra- and extracellular pH and lactate production.

Hypothesis #3: More metastatic lines will be more glycolytically active *in vivo*, creating an environment of high lactate and low extracellular pH for volume matched lesions.

(Aim 3 is related to question 1 outlined in background)

In the progress report for Year 1 we had presented preliminary data which demonstrated that there were significant differences in the vascular volume generated by a invasive metastatic human breast cancer line MDA-MB-231 and a nonmetastatic animal cancer line RIF-1. Studies correlating VEGF distribution with MRI maps of vascular volume and permeability demonstrated that areas around necrosis showed high expression of VEGF and were more permeable. In Year 1 we also presented data to demonstrate that there were significant differences in pH regulation and the phospholipid metabolism in solid tumors growing *in vivo* in SCID mice for a highly metastatic and a less metastatic human breast cancer line. We had therefore made significant progress in Aim 1 and Aim 3 by the end of the first year of the grant.

In Year 2 we had the following achievements. First we showed that the alterations in phospholipid metabolism observed for a highly metastatic and less metastatic tumor could be generalized to an entire panel of human mammary epithelial cells, ranging from normal to highly malignant and metastatic. We also demonstrated that lactate levels significantly increased in malignant cells compared to normal and immortalized hyperplastic human mammary epithelial cells. In addition we developed an implemented multi-slice imaging pulse sequences instead of the originally proposed single slice studies of tumors to determine the vascular characteristics over the entire tumor. In addition we developed a visualization software program which would allow us to interactively relate MRI information with histological maps.

In Year 3 we have used the significant technical advances made in year 2 to comprehensively characterize vascular patterns for three human breast cancer lines, MDA-MB-435, MDA-MB-231 and MCF-7 inoculated in the mammary fat pad of SCID mice.

The technical objectives outlined in our statement of work continue to remain the same and these are: Delineate the role of vascular volume, permeability and perfusion and tumor physiological environment in the formation of metastasis from human breast cancer lines with preselected invasive and metastatic potential grown in SCID (severe combined immune deficient) mice.

### EXPERIMENTAL METHODS USED FOR YEAR 3

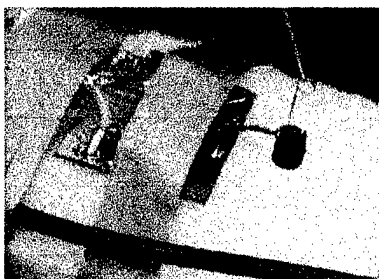
Imaging studies were performed on a GE Omega 4.7T instrument with a solenoidal coil placed around the tumor (volumes 200-300mm<sup>3</sup>) for human breast cancer models MCF-7, MDA-MB-231 and MDA-MB-435 inoculated in the mammary fat pad or flank of SCID mice. The tail vein of the anesthetized animal was catheterized before it was placed in the magnet. Animal body temperature was maintained at 37°C by heat generated from a warm water pad. Multi-slice relaxation rates ( $T_1^{-1}$ ) in tumors were obtained by a saturation recovery method combined with fast T<sub>1</sub> SNAPSHOT-FLASH imaging (flip angle of 7°, echo time of 2ms). Images of 8 slices (slice thickness of 1mm) acquired with an in-plane spatial resolution of 125 µm (128 x 128 matrix, 16mm field of view, NS=8) were obtained for 3 relaxation delays (100ms, 500ms, and 1s) for each of the slices. Thus, 5-8 T<sub>1</sub> maps (depending upon the size of the tumor) were acquired within 7 minutes. An M<sub>0</sub> map with a recovery delay of 7s was acquired once at the beginning of the experiment. Images were obtained before i.v. administration of 0.2ml of 60 mg/ml albumin-GdDTPA in saline (dose of 500mg/kg) and repeated every 8 minutes, starting 10 minutes after the injection, up to 32 minutes. Relaxation maps were reconstructed from data sets for three different relaxation times and the M<sub>0</sub> data set. At the end of the imaging studies, the animal was sacrificed, 0.5 ml of blood was withdrawn from the inferior vena cava, and tumors were marked for referencing to the MRI images, excised, and fixed in 10% formalin for sectioning and staining.

Another technical advance we made this year was to implement a coil which allowed us to determine blood T<sub>1</sub> concentrations from a couple of drops of blood obtained from the tail vein (shown in Figure 1). The advantage of this development is that it is not necessary to sacrifice the animal to determine blood T<sub>1</sub>'s and therefore it is possible to obtain repeated measurements of vascular volume and permeability over a period of time. This would be very useful for determining the effects of therapeutic interventions of vascular characteristics in the same tumor before and after treatment.

Vascular volume and permeability product surface area (PS) maps were generated from the ratio of  $\Delta(1/T_1)$  values in the images to that of blood. The slope of  $\Delta(1/T_1)$  ratios versus time in each pixel was used to compute (PS) while the intercept of the line at zero time was used to compute vascular volume. Thus, vascular volumes were corrected for permeability of the vessels. Ten pairs of adjacent 5µm thick histological sections were obtained at 500 µm intervals

through the tumor were stained with hematoxylin eosin or immunostained for VEGF expression. Sections were digitized with a Sanyo CCD camera attached to an optical microscope.

Blood T<sub>1</sub> measurements can be obtained at 4.7T on a 18  $\mu$ l sample using drops of blood from the tail vein without sacrificing animal



*Coil designed by V. P. Chacko*

T<sub>1</sub> from 18  $\mu$ l sample = 119 msec

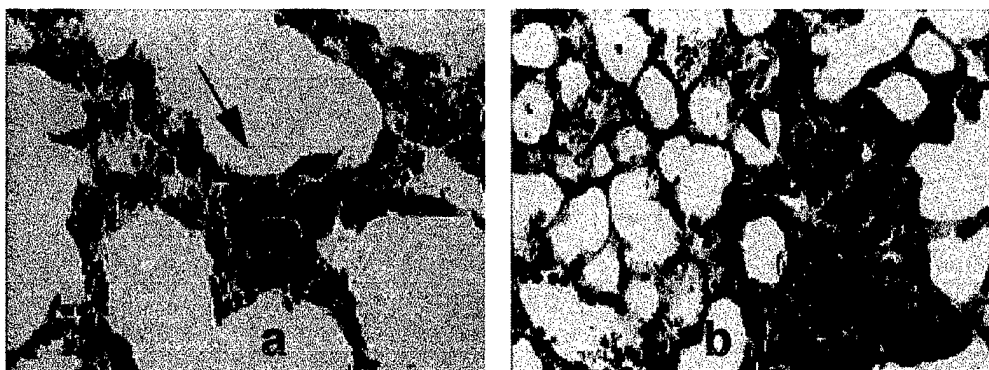
T<sub>1</sub> from 0.3 ml sample taken five minutes after from same animal = 124 msec

Figure 1: Coil design used to determine blood T1's from a couple of drops of blood.

3-D reconstruction of both MRI and histological sections was performed using the Clinical Microscope Visualization software that we are developing as a research tool for use in our investigation. The software consists of two parts, the first part forms the volume image from 2-D images and the second part performs visualization of the volumetric model in suitable 3-D perspective. The high resolution image 'tiles' representing the histological sections acquired from the microscope are stitched along the overlapping borders to produce a large 'virtual' field of view image that represents the full cross section which could not be acquired otherwise in a single actual field of view at the selected high resolution. Such a virtual field of view image can be panned around, zoomed in, to look at selected regions at the full resolution in which they are acquired. Each crosssection is then layered one over the other, to compose the 3-D volume. The volume image is then interactively rendered using the volumetric visualization software, to adjust the transfer functions that control the voxel transparency and intensity characteristics of various structures of interest, to delineate it from the surrounding structures. The software system is developed around Silicon Graphics Inc., Workstation systems, taking full advantage of the hardware accelerated graphics capabilities such as 2- and 3- D Textures to provide interactive rendering results.

## RESULTS

Since we are evaluating the role of vascularization in metastasis it was critical to establish that our human breast cancer models were indeed metastasizing. Shown in Figure 2 are examples of lung sections obtained from mice bearing MDA-MB-435 and MDA-MB-231 breast tumors in the mammary fat pad, demonstrating the presence of metastatic nodules. Metastasis from MDA-MB-231 was less frequent than from MDA-MB-435 supporting observations made by other investigators [18].



**Figure 2:** High power photomicrographs demonstrating metastatic nodules in 5  $\mu$ m thick H & E stained lung sections obtained from mice bearing (a) an MDA-MB-435 tumor and (b) an MDA-MB-235 tumor. Metastatic nodules are marked by arrows.

The MRI method used to generate maps of vascular volume and permeability is based on the assumption that the concentration of the contrast agent remains constant within the vascular system over the period of observation. Although this has been demonstrated in larger animals such as rats and rabbits [19] this has not been demonstrated in mice. We therefore canulated the mouse carotid and used our miniature coil to estimate T1's in blood in the same animal over a period of time. The data obtained for three different animals are presented in Figure 3 and demonstrate that the concentration of albumin-GdDTPA remains constant in the vascular system upto 35 minutes. Our MRI studies are completed within 32 minutes.

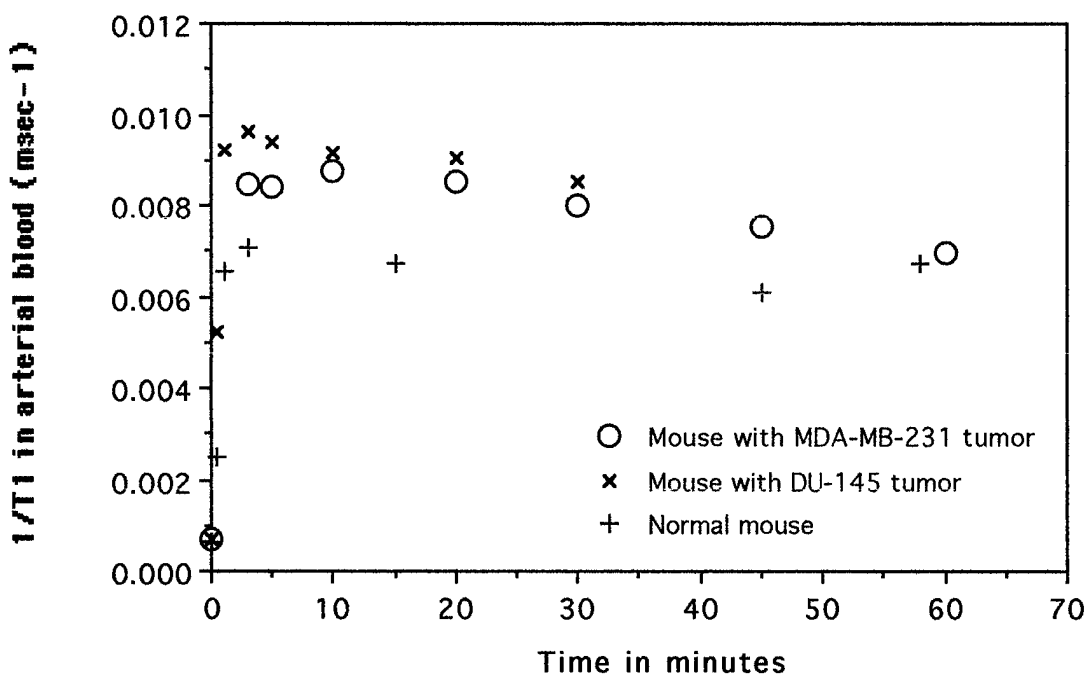


**Figure 3:** Blood relaxation rates following administration of 500mg/kg albumin-GdDTPA.

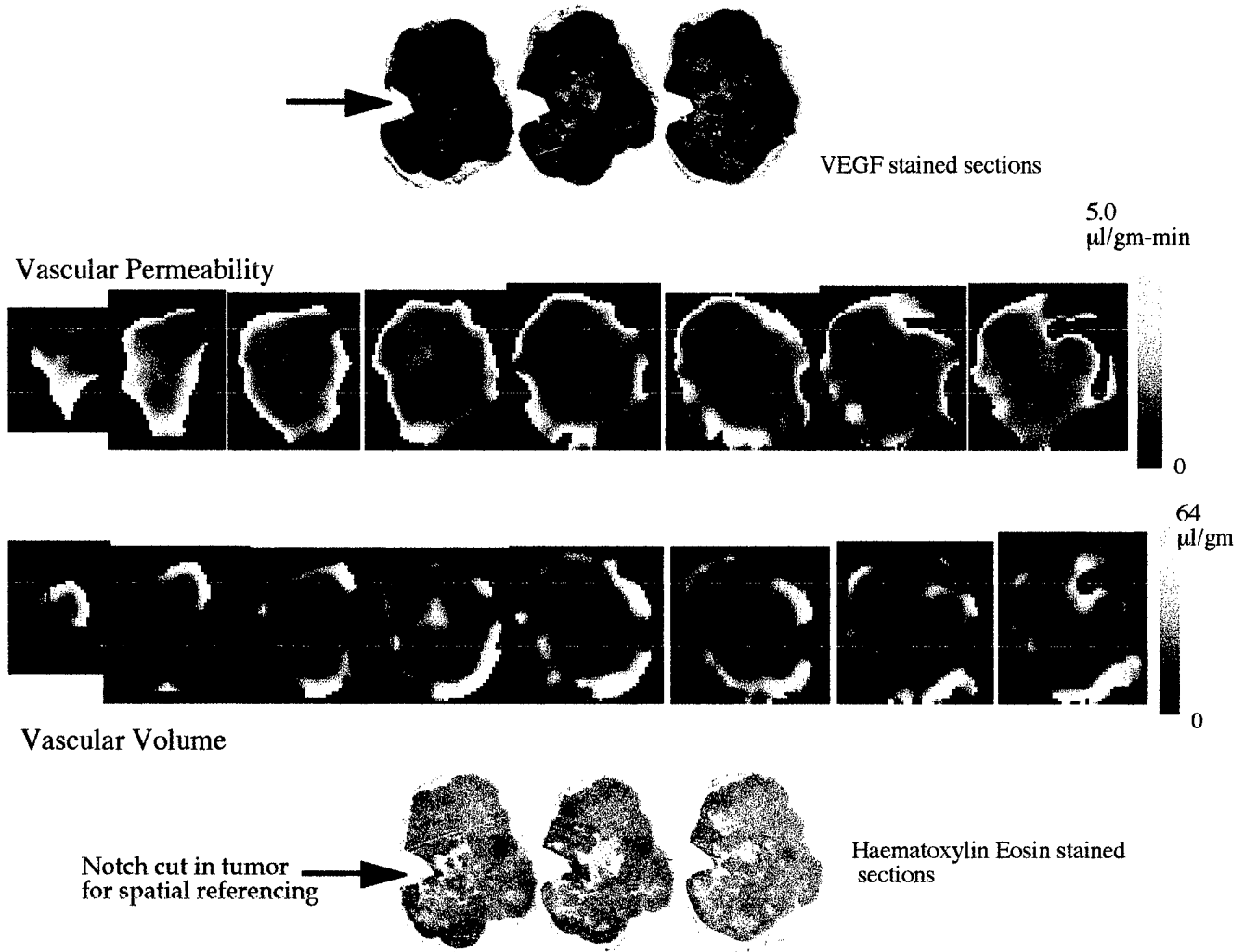


Figure 4: Representative multi-slice data obtained from a human breast cancer model.

Typical multi-slice data of vascular volume and permeability together with histological sections stained with hematoxylin and eosin and VEGF expression, obtained from an MDA-MB-435-1 $\beta$  tumor are shown in Figure 4. The 3D reconstructed maps obtained from these data are shown in Figure 5.

Another major effort of this year was to develop a software program for volumetric analysis of regions of interest within the tumor such as regions of high vascular volume, or permeability and the relationship between the two for the different tumor models. An example of this software analysis is shown in Figure 6.

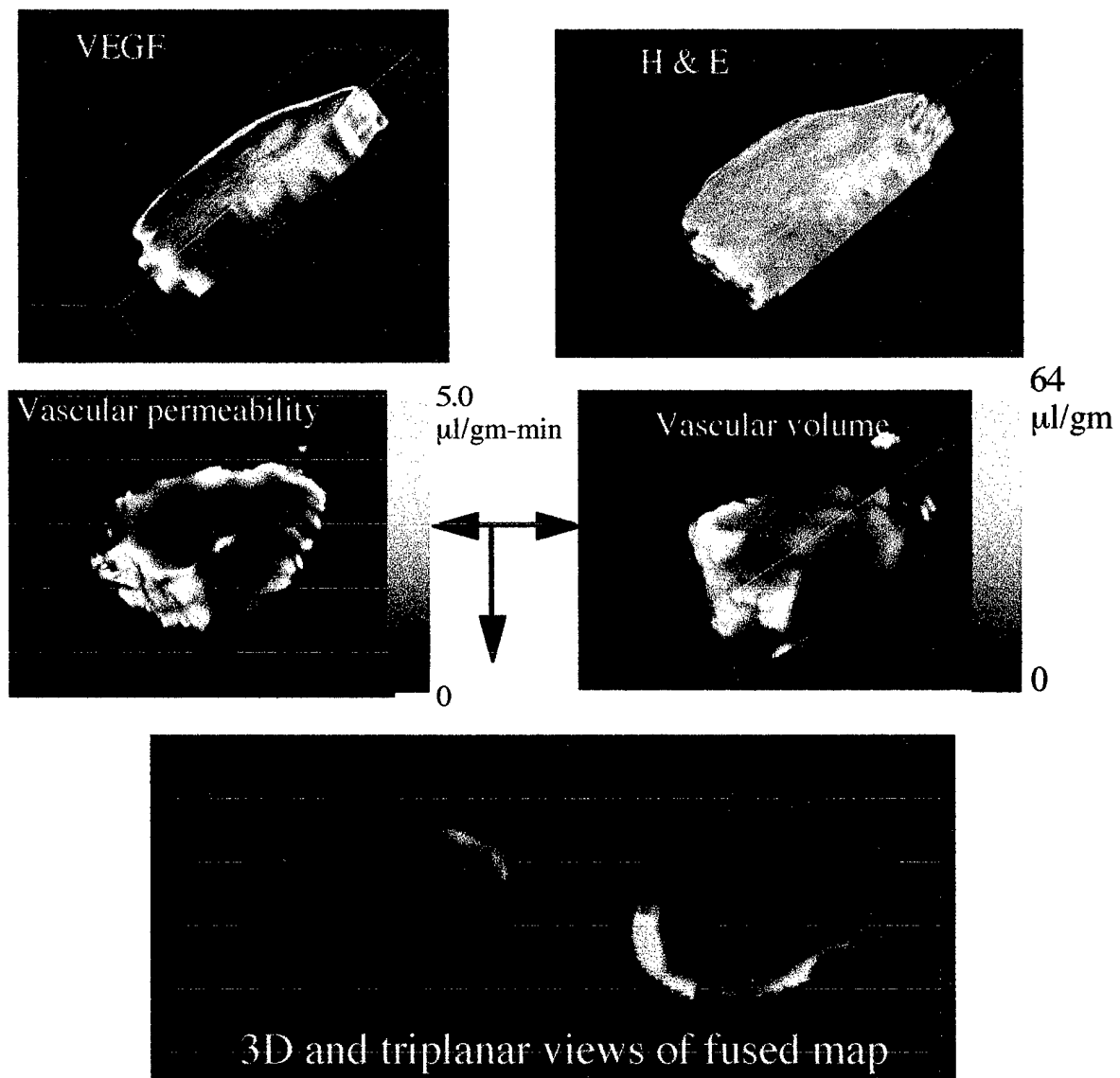
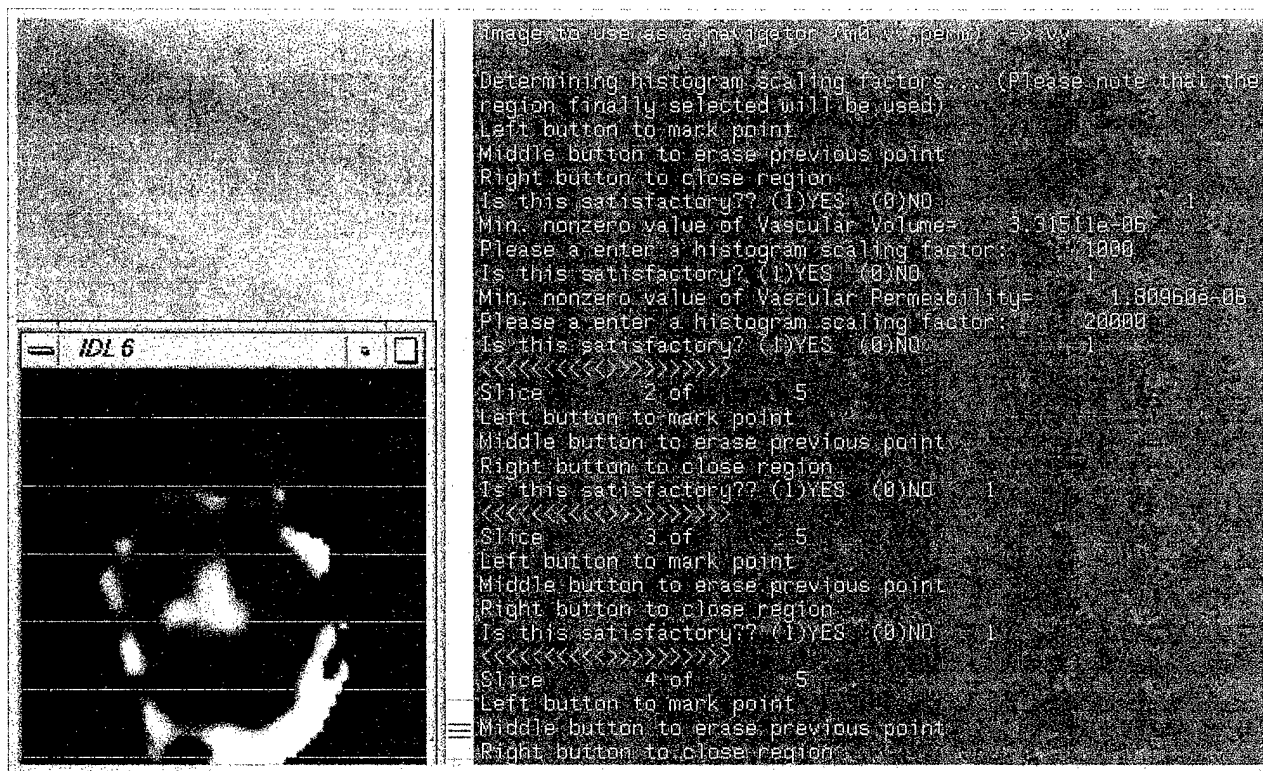


Figure 5: 3D reconstructed maps of vascular volume and permeability. The fused map is obtained by displaying vascular volume through a green channel and vascular permeability through the red channel. The absence of yellow in the fused images demonstrate that there is hardly any overlap of regions of high vascular volume with high permeability.



M0 map  
to navigate

Permeability map  
to navigate

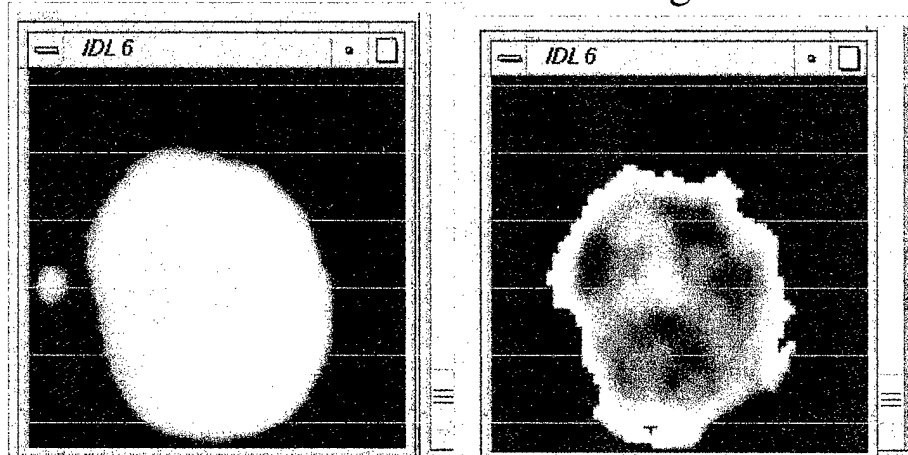
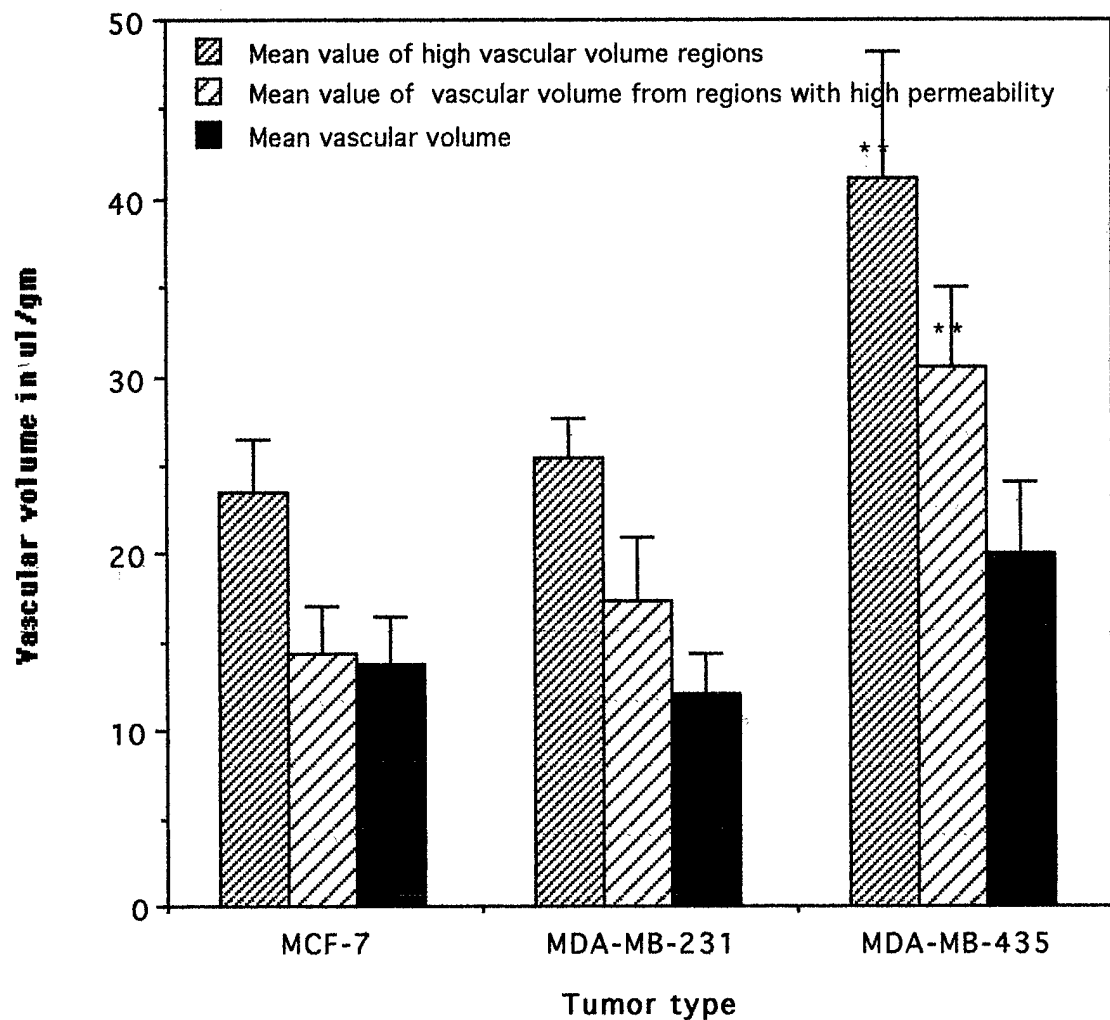


Figure 6: Example of software analysis.

Data obtained from MCF-7, MDA-MB-231 and MDA-MB-435 tumors are summarized below.

### Vascular volume profile



**Figure 7:** Analysis of different vascular categories within the human breast cancer models. Approximately five to eight slices were obtained from each tumor and five to eight tumors were studied for each group. \*\* represents significantly different from MCF-7 tumors. Statistical analysis was performed using Analysis of Variance (ANOVA) with a multi-comparison significance level of 95%. Tumor volumes were size matched and were of the order of  $200\text{-}300 \text{ mm}^3$ .

### Vascular permeability profile

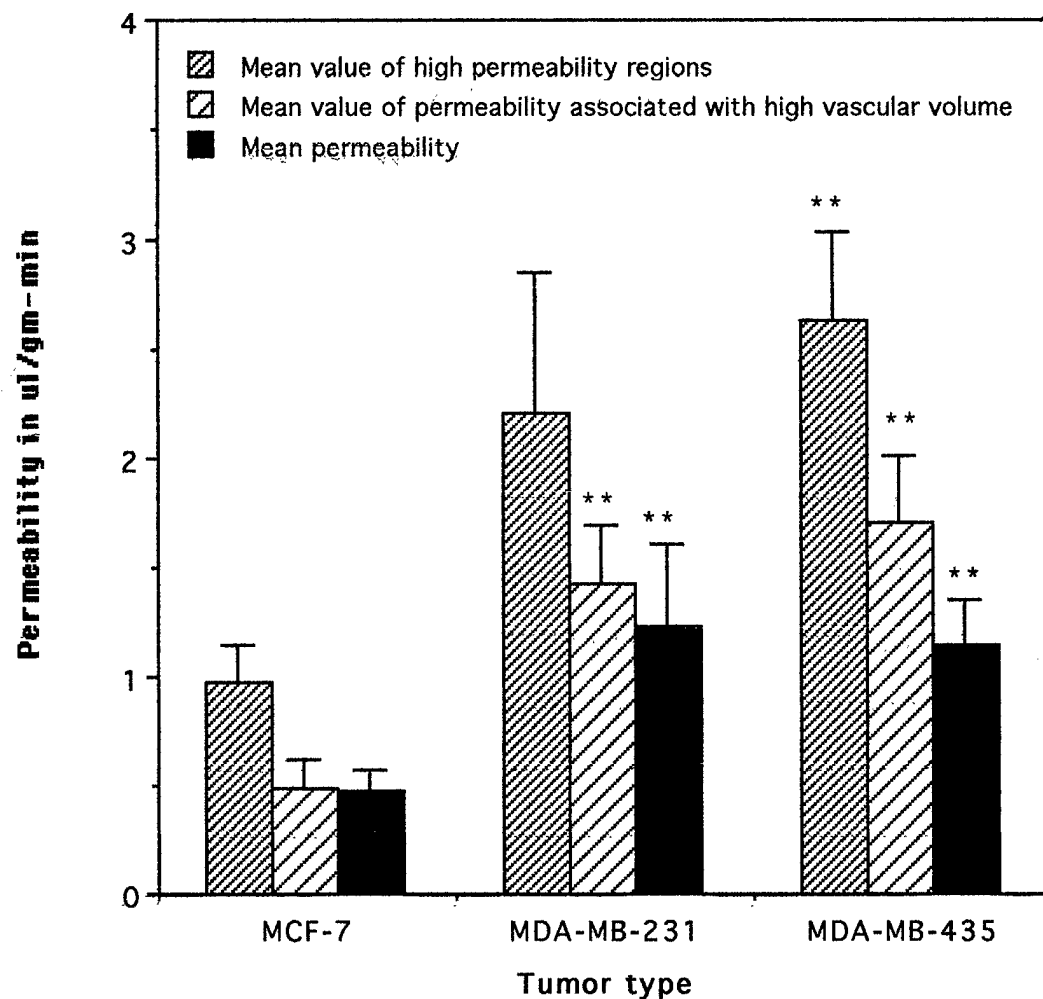


**Figure 8:** Analysis of different permeability categories within the human breast cancer models. Approximately five to eight slices were obtained from each tumor and five to eight tumors were studied for each group. \*\* represents significantly different from MCF-7 tumors. Statistical analysis was performed using Analysis of Variance (ANOVA) with a multi-comparison significance level of 95%. Tumor volumes were size matched and were of the order of  $200\text{-}300 \text{ mm}^3$ .

**CONCLUSIONS:** The results obtained demonstrate that there are significant differences in vascular characteristics between the metastatic and non or less metastatic lines. High vascular volume and high vascular permeability characterized the most metastatic breast cancer line. The non metastatic human breast cancer line MCF-7 exhibited a lower vascular volume as well as lower vascular permeability. We are currently in the process of determining the relationship between vascular volume and permeability and the number and size of metastatic lung nodules in individual animals. Also apparent from the data are the observations that it is essential to characterize the vasculature of the regions of high vascular volume or permeability, since the significance disappears or is less apparent when averaging the measurements over the entire tumor. This demonstrates the necessity of techniques which can detect vascular characteristics with spatial information. In addition, this study further confirmed our previous observations that regions of high vascular volume and high vascular permeability do not coincide spatially. Regions of low vascular volume were usually associated with foci of necrosis in the histological sections. High permeability was related to a higher expression of VEGF. We are now in the process of performing studies for Aim 2 which is to investigate the effect of increasing (a) tumor vascularization and (b) tumor vascularization and permeability on the formation of metastases.

### **KEY RESEARCH ACCOMPLISHMENTS:**

The major findings to emerge from the research studies performed thus far are :

- NMR spectra of primary tumors in SCID mice revealed a dramatic and consistent difference in the phospholipid composition of control and transgene tumors formed by derivatives of MDA-MB-435 human breast carcinoma cells transfected with nm23 constructs. Significant differences in intra and extracellular pH were also detected for solid tumors derived from these lines. This was one of the first *in vivo* observations to link the activity of a putative metastasis suppressor gene to metabolic processes. The data also demonstrate the potential of noninvasive NMR spectroscopy to detect forms of gene therapy which may involve transfection of cells with nm23.
- Choline phospholipid metabolite levels progressively increased in cultured HMEC as cells become more malignant. We therefore propose that carcinogenesis in human breast epithelial cells results in progressive alteration of membrane choline phospholipid metabolism. This work is relevant to diagnosis of breast cancer and also provides a rationale for selective pharmacological intervention.
- Lactate levels increase significantly in cultured HMEC following malignant transformation. However, following malignant transformation, there did not appear to be a close dependence between lactate levels observed in malignant cell lines and the metastatic potential of these lines. The increased lactate production may result in an acidic environment which may promote invasive behavior and contribute to metastasis.
- 3-dimensional interactive analysis of vascular volume and permeability and histological morphology demonstrates that areas of low vascular volume are associated with cell death and increasingly permeable vasculature. Regions of high vascular volume and high vascular permeability do not coincide spatially.
- The more metastatic cell lines are characterized by higher vascular volume and vascular permeability *in vivo* for analysis performed for regions of high vascular volume and permeability. The results indicate a potential use of MRI for evaluating 'metastatic risk' noninvasively.

## **REPORTABLE OUTCOMES**

### **Peer reviewed manuscripts**

1. Aboagye, E. and Bhujwalla, Z. M. Malignant Transformation Alters Membrane Phospholipid Metabolism of Human Mammary Epithelial Cells. *Cancer Research*, 59, 80-84, 1999.
2. van Sluis R, Bhujwalla Z, Raghunand N, Ballesteros P, Alvarez J, Cerdan S Gillies RJ. Imaging of extracellular pH of tumors using <sup>1</sup>H MRSI. *Magnetic Resonance in Medicine*, 41: 743-750, 1999.
3. Bhujwalla, Z. M., Aboagye, E. O., Gillies, R. J., Chacko, V. P., Mendola, C. E., Backer, J. M. Nm23-transfected MDA-MB-435 human breast carcinoma cells form tumors with altered phospholipid metabolism and pH. A <sup>31</sup>P NMR study *In vivo* and *In vitro*. *Magnetic Resonance in Medicine*, 41: 897-903, 1999.
4. Aboagye, E., Artemov, D., Senter, P. D. and Bhujwalla, Z. M. Intratumoral Conversion of 5-Fluorocytosine to 5-Fluorouracil by Monoclonal Antibody-Cytosine Deaminase Conjugates: Noninvasive detection of prodrug activation by Magnetic Resonance Spectroscopy and Spectroscopic Imaging. *Cancer Research*, 58, 4075-4078, 1998.

### **Invited Review**

5. Bhujwalla, Z. M., Artemov, D., Glockner, J. Tumor angiogenesis, vascularization and contrast enhanced MRI. *Topics in Magnetic Resonance Imaging*, (in press), 1999.

### **Review article**

6. Gillies, R. J., Bhujwalla, Z. M., Evelhoch, J., Garwood, M., Neeman, M., Robinson, S. P., Ronen, S. M., Sotak, C. H., van der Sanden, B. Applications of Magnetic Resonance in Model Systems I: Tumor Biology and Physiology. *Neoplasia*, in press (1999).

### **Published abstracts from presentations at conferences**

7. Artemov, D., Solaiyappan, M., Bhujwalla, Z. M. 3-Dimensional Interactive Registration of MRI Images and Histological Data. Proceedings of the Seventh Scientific Meeting of the ISMRM, Philadelphia, 1999.
8. Bhujwalla, Z. M., Artemov, D. A., Solaiyappan, M., Mao, D., Backer, J. P. Comparison of Vascular Volume and Permeability for Tumors derived from Metastatic human breast cancer cells with and without the metastasis suppressor gene nm23. Proceedings of the Seventh Scientific Meeting of the ISMRM, Philadelphia, 1999.

9. Aboagye, E. O. and Bhujwalla, Z. M. Characterization of lactate levels in normal and malignant human mammary epithelial cells. Proceedings of the Seventh Scientific Meeting of the ISMRM, Philadelphia, 1999.
10. Bhujwalla, Z. M., Natarajan, K., Aboagye, E. O., Mori, N., Artemov, D., Pilatus, U. and Chacko, V. P. The anti-inflammatory agent indomethacin reduces the malignant phospholipid phenotype of metastatic human breast cancer cells. Proceedings of the Seventh Scientific Meeting of the ISMRM, Philadelphia, 1999.

Funding awarded based on work supported by this award

**NIH (Bhujwalla, Z.M., P.I.)**

07/01/99-06/30/04

1 R01 CA82337-01

*'Hostile Environments Promote Invasion and Metastasis'*

The aim of these studies is to identify the interaction between the physiological environment and inflammatory signaling and vascularization in breast cancer invasion and metastasis and the ability of anti-inflammatory agents to prevent invasion and metastasis.

## **REFERENCES**

1. Folkman, J., Watson, K., Ingber, D. and Hanahan, D., Induction of angiogenesis during the transition from hyperplasia to neoplasia. *Nature* 339 : 58-61, 1989.
2. Liotta, L.A., Steeg, P.S., Stetler-Stevenson, W.G., Cancer metastases and angiogenesis: an imbalance of positive and negative regulation. *Cell* 64 : 327-336, 1991.
3. Liotta, L., J. Kleinerman, and G. Saidel, Quantitative relationships of intravascular tumor cells, tumor vessels and pulmonary metastases following tumor implantation. *Cancer Research* 34 : 997-1004, 1974.
4. Folkman, J., The vascularization of tumors. *Scientific American* 234 : 59-73, 1976.
5. Folkman, J., How is blood vessel growth regulated in normal and neoplastic tissue ? *Cancer Research* 46 : 467-473, 1986.
6. Moses, M.A., The role of vascularization in tumor metastasis, in "Microcirculation in cancer metastasis", F. William Orr Buchanan, M.R., Weiss, L., Eds. 1991, CRC Press: p. 257-276.
7. Weidner, N., Semple, J.P., Welch, W.R. and Folkman, J., Tumor angiogenesis and metastasis - correlation in invasive breast carcinoma. *New England Journal of Medicine* 324 : 1-8, 1991.
8. Horak, E.R., Leek, R., Klenk, N., LeJeune, S., Smith, K., Stuart, N., Greenal, M., Stepniewska, K. and Harris, A.L. , Angiogenesis, assessed by platelet/endothelial cell adhesion molecule antibodies, as indicator of node metastases and survival in breast cancer. *Lancet* 340 : 1120-1124, 1992.
9. Mareel, M.M., Baetselier, P., van Roy, F.M., Mechanisms of Invasion and Metastasis. 1991, CRC Press.
10. Shweiki, D., Itin, A., Soffer, D. and Kesbet, E., Vascular endothelial growth factor induced by hypoxia may mediate hypoxia-initiated angiogenesis. *Nature* 359 : 843-845, 1992.
11. Plate, K.H., Breier, Weich, H. and Risau, W., Vascular endothelial growth factor is a potential tumor angiogenesis facotr in human gliomas in vivo. *Nature* 359 : 845-848, 1992.
12. Cooper, R.G., Taylor, C.M., Choo, J.J. and Weiss, J.B., Elevated endothelial-cell stimulating angiogenic factor activity in rodent glycolytic skeletal muscles. *Clinical Science* 81 : 267-270, 1991.
13. Knighton, D.R., Hunt, T.K., Scheuenstuhl, H. and Banda, M., Oxygen tension regulates the expression of angiogenesis factor by macrophages. *Science* 221 : 1283-1285, 1983.

14. Knighton, D., Schumerth, S., and Fiegel, V., Environmental regulation of macrophage angiogenesis., in "Current Communications in Molecular Biology, Angiogenesis: Mechanisms in Pathobiology.", D.B. Rifkin Klagsbrun, M., Eds. 1987, Cold Spring Harbor Laboratory: p. 150-157.
15. Jensen, A.J., Hunt, B., Scheuenstuhl, B. and Banda, M.J., Effect of lactate, pyruvate and pH on secretion of angiogenesis and mitogenesis factors by macrophages. *Laboratory Investigations* 56 : 574-578, 1986.
16. Rozhin, J., Sameni, M., Ziegler, G. and Sloane, B.F., Pericellular pH affects distribution and secretion of Cathepsin B in Malignant cells. *Cancer Research* 54 : 6517-6525, 1994.
17. Kato, Y., Nakayama, Y., Umeda, M. and Miyazaka, K., Induction of 103kDa gelatinase/type IV collagenase by acidic culture conditions in mouse metastatic melanoma cell lines. *J. Biol. Chem.* 267 : 11424-11430, 1992.
18. Price, J.E., Polyzos, A., Zhang, R.D. and Daniels, L.M., Tumorigenicity and metastasis of human breast carcinoma cell lines in nude mice. *Cancer Research* 50 : 717-721, 1990.
19. Schmiedl, U., Ogan, M., Moseley, M.E., Brasch, R.C., Comparison of the contrast-enhancing properties of albumin-(Gd-DTPA) and Gd-DTPA at 2.0T: an experimental study in rats. *A.J.R.* 147 : 1263-1270, 1986.

# Malignant Transformation Alters Membrane Choline Phospholipid Metabolism of Human Mammary Epithelial Cells<sup>1</sup>

Eric O. Aboagye and Zaver M. Bhujwalla<sup>2</sup>

The Johns Hopkins University School of Medicine, Division of Magnetic Resonance Research–Oncology Section, Department of Radiology, Baltimore, Maryland 21205

## ABSTRACT

Transduction of mitogenic signals in cells can be mediated by molecules derived from the synthesis and breakdown of the major membrane phospholipid, phosphatidylcholine. Studies were performed on human mammary epithelial cells in culture to understand the impact of malignant transformation and progression on membrane phospholipid metabolism. In the model system used here, phosphocholine levels and total choline-containing phospholipid metabolite levels increased with progression from normal to immortalized to oncogene-transformed to tumor-derived cells. These changes occurred independently of cell doubling time. A “glycerophosphocholine to phosphocholine switch” was apparent with immortalization. This alteration in phenotype of increased phosphocholine relative to glycerophosphocholine was observed in oncogene-transformed and for all human breast tumor cell lines analyzed. The results demonstrate that progression of human mammary epithelial cells from normal to malignant phenotype is associated with altered membrane choline phospholipid metabolism.

## INTRODUCTION

PtC<sup>3</sup> is the most abundant phospholipid in biological membranes and together with other phospholipids, such as phosphatidylethanolamine and neutral lipids, form the characteristic bilayer structure of cells and regulate membrane integrity (1, 2). MCPM (Fig. 1), i.e., biosynthesis and hydrolysis of PtC, are essential processes for mitogenic signal transduction events in cells (3–6). There is now increasing evidence to suggest that products of MCPM such as PCho, diacylglycerol, and arachidonic acid metabolites may function as second messengers essential for the mitogenic activity of growth factors particularly in the activation of the *ras-raf-1-MAPK* cascade and protein kinase C pathway (3–6). Together with inositol phospholipid metabolism, MCPM can also provide a sustained activation of mitogenic signal transduction via a positive feedback interaction (4, 7).

The regulation of MCPM can occur through growth factor stimulation (4, 5) or requirements for eicosanoid production.<sup>4</sup> There is now increasing evidence to suggest that the activity of key enzymes involved in MCPM are regulated by receptor tyrosine kinase cascade downstream of the *ras/raf* interaction (8, 9). This assertion is supported by the fact that activation of receptor tyrosine kinase growth factor-mediated signal transduction at the level of growth factor, *ras*, or *raf* produces an enhanced MCPM (8, 9). Because signal transduction events and genetic alterations involving amplification of oncogenes such as *erbB2* play a crucial role in the development of the normal breast, carcinogenesis of its epithelium, and progression of breast cancer, it is possible that regulation of the levels of choline-

containing metabolites may be linked to malignant transformation and progression of the breast epithelium.

NMR has been used to study choline phospholipid metabolism in cells or excised tissues, as well as noninvasively *in vivo* (10–13). Depending on the experimental conditions, <sup>1</sup>H NMR methods can detect either individual choline phospholipid metabolites or a peak corresponding to total choline-containing metabolites. Using <sup>1</sup>H NMR, invasive cancer could be distinguished from benign breast lesions by the high total choline phospholipid metabolite levels in the former (10). In another study, increased choline phospholipid metabolite levels characterized two cancer cell lines (MCF-7 and T47D) compared with that of a normal HMEC line; there were no distinct differences in high energy phosphates and the rates of glucose consumption and aerobic glycolysis (14). These studies support the existence of differences in phosphatidylcholine metabolism between normal epithelial cells and cancer cells *in vitro* and between benign and malignant cells *in vivo*. The possibility of differential regulation of MCPM in normal *versus* tumor cells suggests a diagnostic role for enhanced MCPM and has implications for therapeutic intervention.

Despite the indication of an altered MCPM in breast cancer cells, no attempt has been made to systematically relate the multistep process of carcinogenesis to altered MCPM in mammary epithelial cells. To address this issue, we have assessed PCho, GPC, and choline levels in a number of epithelial cell lines derived from reduction mammoplasty (normal) tissues and neoplastic lesions and also investigated the effects of immortalization and oncogene transformation on MCPM. Such a model has been used previously by other workers to evaluate the stepwise progression in mammary epithelium from normal to malignant phenotype (15–20). Our data suggest that phenotypic changes in MCPM probably commence early in carcinogenesis and may, as with most other neoplastic phenotypes, be regulated by an interplay of cellular immortalization and oncogene transformation.

## MATERIALS AND METHODS

**Cell Lines.** HMECs used in this study include finite life span HMEC strains 184 and 48, derived from reduction mammoplasty tissues; nontumorigenic immortal cell lines 184A1 and 184B5, derived from benzo(a)pyrene-treated 184 cells; and the 184B5-*erbB2* cell line, derived from 184B5 by transfection with the *erbB2* oncogene. All of the above cell lines were obtained from Dr. Martha Stampfer (Lawrence Berkeley National Laboratory, Berkeley, CA) and cultured in MCDB 170 media supplemented as described previously (21, 22). MCF-12A, a spontaneously immortalized cell line established from MCF-12M mortal cells (23), was obtained from American Type Culture Collection (Rockville, MD) and cultured in DMEM-Ham's F12 medium supplemented as described previously (23). All of the human breast cancer cell lines were derived from pleural effusions in patients with breast cancer and were obtained from American Type Culture Collection. The tumor-derived cell lines were all cultured in DMEM-Ham's F12 medium supplemented with 10% fetal bovine serum.

**Growth Rate and Cell Size.** The growth rate of the cell lines used in this study were determined using the MTT assay (24). Briefly, cells ( $5 \times 10^3$ ) were plated in 24-well plates in 1 ml of media and incubated under normal culture conditions for up to 6 days. To estimate cell number, the cells were incubated with MTT (Sigma Chemical Co., St. Louis, MO) for 4 h. MTT was then removed, and the resulting formazan crystals were dissolved in 1 ml of DMSO and 125  $\mu$ l of glycine buffer (pH 10.5; Ref. 24). The UV absorbance of the

Received 6/18/98; accepted 10/28/98.

The costs of publication of this article were defrayed in part by the payment of page charges. This article must therefore be hereby marked *advertisement* in accordance with 18 U.S.C. Section 1734 solely to indicate this fact.

<sup>1</sup> This work was supported by USAMRMC Grant DAMD-17-96-16131.

<sup>2</sup> To whom requests for reprints should be addressed, at The Johns Hopkins University School of Medicine, Division of Magnetic Resonance Research–Oncology Section, Department of Radiology, 208C Traylor Building, 720 Rutland Avenue, Baltimore, MD 21205.

<sup>3</sup> The abbreviations used are: PtC, phosphatidylcholine; MCPM, membrane choline phospholipid metabolism; PCho, phosphocholine; GPC, glycerophosphocholine; NMR, nuclear magnetic resonance; HMEC, human mammary epithelial cell; MTT, 3-(4,5-dimethylthiazol-2-yl)-2,5-diphenyltetrazolium bromide; TSP, trimethylsilylpropionate.

<sup>4</sup> Z. M. Bhujwalla and E. O. Aboagye, unpublished data.

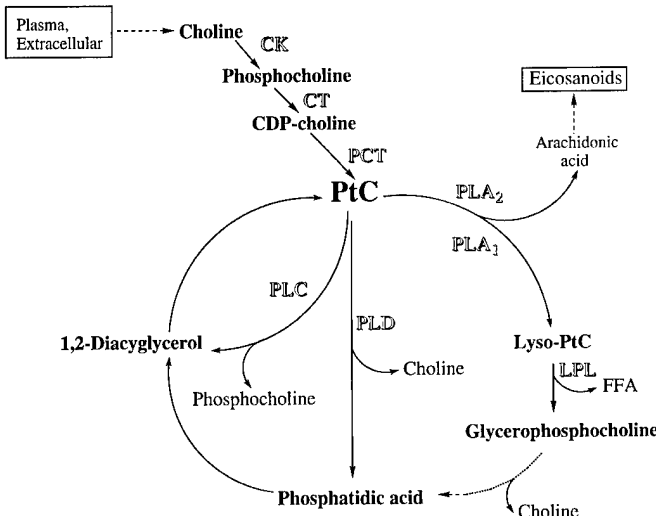


Fig. 1. Biosynthesis and hydrolysis of PtC. Phosphorylation of choline to PCho by choline kinase (CK) is the first step in the biosynthesis of PtC. PCho is then converted to PtC via intermediates involving the rate-limiting enzyme CTP: phosphocholine cytidyltransferase (CT) and phosphocholine transferase (PCT). Hydrolysis of PtC is effected by three major PtC-specific enzymes, phospholipase C (PLC), phospholipase D (PLD), and phospholipase A<sub>1</sub> and A<sub>2</sub> (PLA<sub>1</sub> and PLA<sub>2</sub>). FFA, free fatty acid.

formazan solution was recorded at 553 nm ( $\lambda_{\text{max}}$ ). Four replicates were used to calculate the cell doubling time for each cell line. Because the cells had different morphologies and diameters, the cell size was determined for each cell line by trypsinizing the cells and counting the diameter of 20 random cells using an optical microscope.

**Extraction.** To determine the choline phospholipid metabolite content, cells growing in culture were fed with fresh media 24 h before extraction and used at 70–80% confluence. Cells ( $10^7$  to  $10^8$ ) were trypsinized, washed twice with normal saline, and homogenized with ice-cold 8% perchloric acid (5 ml). The homogenates were centrifuged (15000 rpm for 15 min at 4°C), and the supernatants were neutralized with 3 M  $\text{K}_2\text{CO}_3$ /1 M KOH buffer. The samples were again clarified by centrifugation, treated with ~50 mg Chelex (Sigma) to remove divalent ions, lyophilized, and resuspended in 0.5 ml of  $\text{D}_2\text{O}$  for NMR analysis. Trimethylsilyl propionate (5  $\mu\text{l}$ ) was used as an internal standard.  $^1\text{H}$  NMR spectra of the extracts were acquired on a 11.7T Bruker NMR spectrometer with a 5-mm probe. Fully relaxed spectra (without saturation effects) were obtained using the following acquisition parameters: 30° flip angle, 6000 Hz sweep width, 4.7 s repetition time, 32 K block size, and 512 scans. The data were analyzed using an in-house software, Soft Fourier Transform (P. Barker, The Johns Hopkins University). PCho, GPC, and total choline-containing (PCho + GPC + choline) metabolite levels were determined and normalized to cell size. Between three and five independent extracts were analyzed per cell line.

The reason for normalizing metabolite levels to cell size was due to differences in cell size between the cell lines used in this study. This necessitated normalization to either cell size or protein concentration. The former requires fewer cells and is therefore suited to experiments with mortal cells, which senesce after 5 to 18 passages. To determine concentrations, peak amplitudes for choline PCho, GPC, and total choline-containing metabolites (PCho + GPC + choline) were compared with that of the internal standard TSP according to the equation:

$$[\text{metabolite}] = \text{Amplitude}_{(\text{metabolite})}$$

$$\times \frac{[\text{TSP}]}{\text{Amplitude}_{(\text{TSP})} \times \text{cell number} \times \text{cell volume}}$$

where [metabolite] is concentration of the metabolite expressed as fmol/ $\mu\text{m}^3$ , [TSP] is the molar concentration of TSP used, and cell volume ( $\mu\text{m}^3$ ) was calculated from the radius of the cell according to the equation, volume =  $4/3 \times \pi r^3$ . For this equation to be valid, it is necessary that spectra are fully relaxed, as was the case here, or to correct for saturation.

**Statistical Analysis.** Statistical analysis of the data were performed using StatView II version 1.04, 1991 (Abacus Concepts, Inc., Berkeley, CA). The statistical significance of differences in metabolite levels between cell lines was determined using the Mann-Whitney *U* test. *P*s of  $\leq 0.05$  were considered to be significant.

## RESULTS

**Identification of Phospholipid Metabolites by  $^1\text{H}$  NMR.**  $^1\text{H}$  NMR of perchloric acid extracts demonstrated the presence of three water-soluble, choline-containing [-N(CH<sub>3</sub>)<sub>3</sub>] metabolites, *i.e.*, choline, PCho, and GPC (Fig. 2). These metabolites resonate at ~3.2 ppm downfield of the internal standard and chemical shift reference TSP. Peak assignments were performed with authentic compounds. Ten epithelial cell lines of mammary origin were characterized by this method; the phenotype and cell size of these cell lines are indicated in Table 1.

**The “GPC to PCho Switch” in Mammary Epithelial Cells.** Analysis of individual choline metabolites uncovered an early alteration in MCPM that was linked to immortalization and malignant transformation, the “GPC to PCho switch” (Fig. 3). In Fig. 3 it is evident that GPC was the major choline metabolite in the finite life span HMEC strains 48 and 184. Thus, these cells showed a low PCho:GPC ratio of  $<1$ . Immortalization of cells, however, resulted in variable effects. The spontaneously immortalized cell line MCF-12A showed a similar phenotype (PCho:GPC) as the finite life span cells; we do not have the finite life span cells from which MCF-12A was established for comparison. In contrast, the benzo(a)pyrene-immortalized cell lines showed a GPC to PCho switch, *i.e.*, PCho was now the major choline metabolite. Of interest, the two immortal lines derived from the 184 strain showed variable degrees of this altered MCPM; 184A1 had a higher PCho:GPC level compared with 184B5. Forced overexpression of normal *erbB2* gene into 184B5 cells dramatically increased the PCho:GPC ratio in this cell line. The altered GPC to PCho switch was detected in all breast cancer cell lines analyzed.

**Breast Cancer Cells Have a High Choline Content.** Fig. 4 shows that there was a gradual increase in both PCho levels and total choline-containing metabolite levels as cells progressed from normal to malignant phenotype (normal < immortal < oncogene-transformed < tumor-derived). GPC levels also increased, albeit to a lesser extent than PCho levels and total choline-containing metabolite levels. It is worth noting that despite the GPC to PCho switch, total choline-

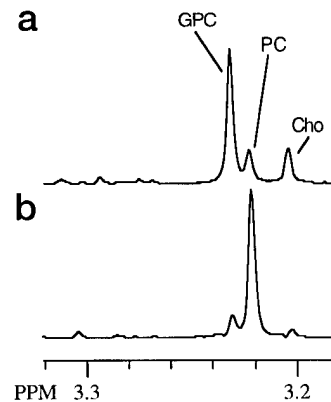


Fig. 2. Typical  $^1\text{H}$  NMR spectra obtained from perchloric acid extracts of MCF-12A (a) and MDA-MB-231 (b) breast cancer cells grown in culture. The spectra, expanded to show the choline-containing metabolite region, represent qualitative differences between the two cell lines, *i.e.*, not normalized to display comparable signal-to-noise levels. Spectral assignments include GPC (3.234 ppm), PCho (3.225 ppm), and free choline (Cho; 3.207 ppm).

Table 1 Phenotype and size of cell lines used in this study

Cell types	Phenotype <sup>a</sup>	Cell volume <sup>b</sup> ( $\times 10^3 \mu\text{m}^3$ )
Normal HMECs		
184	Senescent, ADG	36.5 $\pm$ 6.8
48	Senescent, ADG	11.1 $\pm$ 3.1
Spontaneously immortalized HMECs		
MCF-12A	Immortal, ADG	9.8 $\pm$ 1.8
Benz(a)pyrene-immortalized HMECs		
184A1	Immortal, ADG	7.1 $\pm$ 0.9
184B5	Immortal, ADG	7.7 $\pm$ 0.9
Oncogene-transformed HMECs		
184B5-erbB2	Immortal, AIG, forms low frequency, high latency tumors	7.0 $\pm$ 0.8
Breast cancer cells		
SKBR3	AIG, tumorigenic, low metastaticity	21.9 $\pm$ 7.3
MCF7	AIG, tumorigenic, low metastaticity	6.7 $\pm$ 1.5
MDA-MB-231	AIG, tumorigenic, highly metastatic	8.4 $\pm$ 1.4
MDA-MB-435	AIG, tumorigenic, highly metastatic	3.5 $\pm$ 0.4

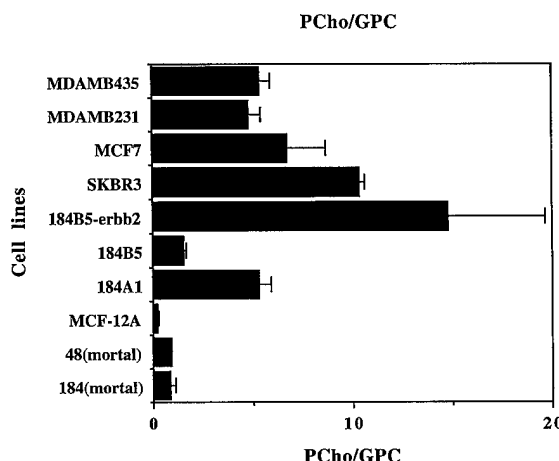
<sup>a</sup> ADG, anchorage-dependent growth; AIG, anchorage-independent growth.<sup>b</sup> Mean  $\pm$  SE.

Fig. 3. PCho:GPC ratios in a panel of cell lines representing various stages of breast carcinogenesis. There was a statistically significant difference in PCho:GPC ratio ( $P < 0.05$ ) between finite life span versus tumor-derived cells, 184 strain versus 184A1 cell line, and 184B5 versus 184B5-erbB2 cell lines. The  $P$  for 184 strain versus 184B5 cell line was 0.1. Bars, SE.

containing metabolite levels and PCho levels in immortalized cell lines such as 184A1, which was nontumorigenic, and 184B5-erbB2, which exhibited low tumorigenicity, were significantly lower than any of the tumorigenic breast cancer cells.

**Are the High Choline Phospholipid Metabolite Levels in Breast Cancer Cells a Function of Their Rate of Cellular Proliferation?** It is generally thought that the increase in phosphomonoester (mainly PCho and phosphoethanolamine) metabolite levels in cancer cells is due to their intensified cell membrane synthesis to cope with rapid growth and proliferation (12, 25). This assertion is supported, for instance, by the work of Smith *et al.* (26), where an increase in PCho and a decrease in GPC correlated strongly with tumor growth rate. Thus, we tested the hypothesis that increased PCho:GPC levels, PCho, GPC, or total choline-containing metabolite levels may be the result of high proliferation. A systematic measurement of cell doubling time in all of the cell lines revealed that there was no overall correlation between cell doubling time and PCho:GPC ratio, PCho levels, GPC levels, or total choline-containing metabolite levels (Fig. 5;  $r < 0.2$ ;  $P > 0.1$ ). For instance, MCF-12A cells exhibited a doubling time in culture comparable with the tumorigenic cell line MDA-MB-435. However, MCF-12A cells exhibited a significantly lower PCho:GPC

ratio, a low level of total choline-containing metabolites, and low PCho compared with MDA-MB-435 cells.

## DISCUSSION

Carcinogenesis of the mammary epithelium occurs through a multistep process involving genetic alterations, amplification of oncogenes, and loss of tumor suppressor function (27, 28). The stages of

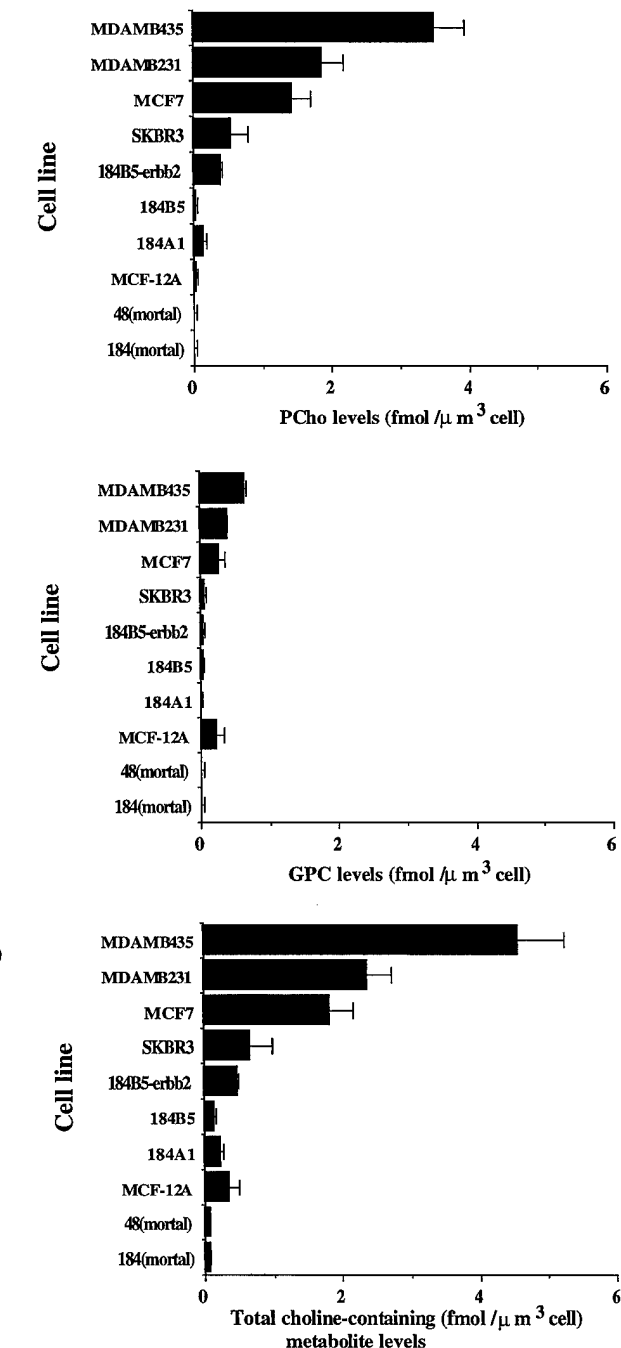


Fig. 4. PCho levels (a), GPC levels (b), and total choline-containing metabolite (PCho + GPC + choline) levels (c) in a panel of cell lines representing various stages of breast carcinogenesis. There was a statistically significant difference in total choline-containing metabolite levels and PCho levels ( $P < 0.05$ ) for finite life span cells versus tumor-derived cells; 184 strain versus 184A1; 184B5 versus 184B5-erbB2; MDA-MB-435 versus MDA-MB-231, MCF7, and SKBR3; MDA-MB-231 versus SKBR3; and MCF7 versus SKBR3. There was a statistically significant difference in GPC levels for finite life span cells, 184A1, 184B5 and 184B5-erbB2, and SKBR3 versus MDA-MB-435, MDA-MB-231, MCF7, and MCF-12A cells. Bars, SE.

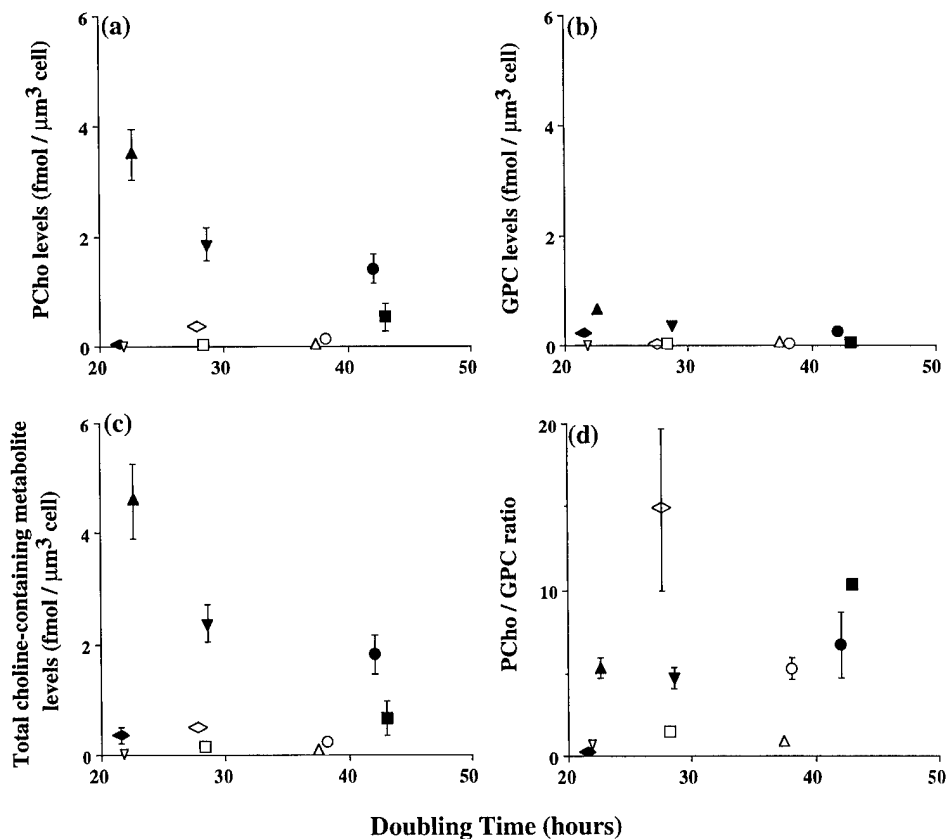


Fig. 5. The relationship between doubling time and PCho levels (*a*), GPC levels (*b*), total choline-containing metabolite levels (PCho + GPC + choline; *c*), and PCho:GPC ratio (*d*). Doubling times were measured by the MTT assay (see "Materials and Methods") and increased in the order MCF-12A > 48 (mortal) > MDA-MB-435 > 184B5-erbB2 > 184B5 > MDA-MB-231 > 184 (mortal) > 184A1 > MCF-7 > SKBR3; ▲, MDA-MB-435; ▼, MDA-MB-231; ●, MCF-7; ■, SKBR3; ♦, MCF-12A; Δ, 184 (mortal); ▽, 48 (mortal); ○, 184A1; □, 184B5; ◇, 184B5-erbB2. Bars, SE.

carcinogenesis can broadly be classified as transformation of normal cells to benign hyperplasia followed by atypical hyperplasia, which progresses to carcinoma *in situ* and finally to infiltrating carcinoma with or without metastasis to distant sites. *In vitro* models based on immortalization and oncogene transformation of normal HMECs have been developed to study mammary carcinogenesis (15–20). These immortalized, oncogene-transformed, and cancer cells show differences in phenotypes that differentiate normal cells from immortal/malignant cells, such as karyotype, vimentin/uvomorulin expression, responsiveness to transforming growth factor  $\beta$ , telomere length/telomerase expression, activating protein 1 transcription factor activity, as well as anchorage-dependent/independent growth, and ability to form tumors in immune-deficient mice.

We have investigated the association between malignant carcinogenic processes and MCPM by monitoring the three choline phospholipid metabolites (choline, PCho, and GPC) in 10 cell lines, which represent different stages of malignant progression. Our findings suggest that normal human mammary epithelium has low steady-state levels of total choline-containing metabolites. In addition to their low total choline-containing metabolite levels, we also demonstrated that GPC was the major metabolite in the normal HMECs. A GPC to PCho switch appeared to be an early phenotypic change during carcinogenesis, as observed in benzo-(*a*)pyrene-immortalized cells and where instead of GPC, PCho became the major choline phospholipid metabolites. However, despite this "switch," total choline-containing metabolite levels remained low in these immortalized cells. Transformation of 184B5 immortal cells by forced overexpression of the *erbB2* oncogene, however, resulted in a dramatic increase in both PCho:GPC ratio and total choline levels compared with the benzo-(*a*)pyrene-immortalized cells. However, total choline-containing metabolites and PCho levels were still less than those of tumor-

derived cells. *erbB2* is an important (proto)oncogene that is amplified in 20–30% of breast cancer cases and is associated with poor prognosis; amplification of this oncogene is thought to occur late in tumor progression (27–30). Transformation of 184B5 by this gene results in the ability of these cells to form colonies in semisolid medium and to form small, low frequency tumors with high latency *in vivo* (16). Our data with *erbB2* demonstrate a new and heretofore unknown metabolic role for *erbB2* and support the possibility that growth factor-mediated activation of the tyrosine kinase cascade (involving receptor-grb 2-sos-ras-raf-1-MEK-MAPK) can lead to an increase in PCho levels (6–9). In general, the levels and expression of receptors and proteins involved in the growth factor receptor-tyrosine kinase pathway tend to increase with malignancy. For instance, levels of epidermal growth factor receptor are low in the 184 strain, moderately high in 184A1, 184B5, and 184B5-*erbB2* cells, and very high in MDA-MB-231 cells (19, 31). In addition, Daly *et al.* (32) reported up-regulation of *grb2* mRNA/protein and the *ras* signaling pathway in MCF-7 and MDA-MB-231 cells compared with normal HMECs.

All of the breast tumor cell lines showed the GPC to PCho switch. In addition to this switch, all breast tumor cells showed significantly higher total choline-containing metabolite levels ( $P < 0.05$ ). The increased total choline-containing metabolite levels were mainly due to an increase in PCho levels and, to a lesser and variable extent, an increase in GPC levels. There was a gradual increase in both total choline-containing metabolite levels and PCho levels as the cells acquired malignant phenotype (normal < immortal < oncogene-transformed < tumor-derived), with the highly invasive metastatic cell lines showing the highest levels. The high total choline content in the tumorigenic cells may be related to the multiple genetic changes that are associated with the multistep process of carcinogenesis (28) and may explain the progressive ability of these cells to gain

anchorage-independent growth, form primary tumors in immune compromised mice, and finally to metastasize. Our studies confirm the work of Ting *et al.* (14), who showed for a limited number of cell lines that levels of choline-containing metabolites were low in a normal mammary epithelial strain and high in two tumor-derived cell lines. Our results also support recent clinical observations that the total choline peak is higher for malignant lesions than for benign ones (10).

It has been postulated that the rapid growth and proliferation of cancer cells and increased membrane/fatty acid requirements may be responsible for the high choline phospholipid metabolite levels in cancer *versus* normal tissues (12, 25, 26); the same argument could be made for benign lesions *versus* invasive cancers. However, the data presented here and that of Ting *et al.* (14) show that choline-containing metabolite levels remain low in normal HMECs in culture when the cells are proliferating at approximately similar rates as tumor-derived cells and suggest that although proliferation-related changes may occur (26), the rate of proliferation *per se* cannot completely account for the increased choline phospholipid metabolism. In this study, we have demonstrated that an alteration in MCPM is linked to malignant transformation and progression of mammary epithelium. Presently, the exact mechanisms underlying the altered metabolism are unknown. Possible mechanisms include activation of enzymes involved in MCPM, such as via enhanced receptor tyrosine kinase cascade (9), or differential induction of choline kinase isozymes, as reported previously for carcinogen-treated rat liver (33). Other possible mechanisms that need to be investigated include amplification of choline kinase, phospholipase C, phospholipase D, and phospholipase A genes during carcinogenesis.

To conclude, the major finding to emerge from the present study is that choline phospholipid metabolite levels progressively increase in cultured HMECs as cells become more malignant. We therefore propose that carcinogenesis in human breast epithelial cells results in progressive alteration of membrane choline phospholipid metabolism. This work is relevant to diagnosis of breast cancer and also provides a rationale for selective pharmacological intervention.

## ACKNOWLEDGMENTS

We are very grateful to Dr. Martha Stampfer of Berkeley National Laboratory (Berkeley, CA) for kindly donating the HMECs used in this study and for very useful suggestions. We gratefully acknowledge the expert technical assistance of Dr. V. P. Chacko in performing the NMR spectroscopy experiments, and we thank N. Mori for assistance with the cell doubling time measurements.

## REFERENCES

- Cullis, P. R., and Hope, M. J. Physical properties and functional roles of lipids in membranes. In: D. E. Vance and J. Vance (ed.), *Biochemistry of Lipids, Lipoproteins and Membranes*, pp. 1–41. Amsterdam: Elsevier Science Publishers, 1991.
- Mountford, C. E., and Wright, L. C. Organization of lipids in the plasma membranes of malignant and stimulated cells: a new model. *Trends Biochem. Sci.*, **13**: 172–177, 1988.
- Cuadrado, A., Carnero, A., Dolfi, F., Jimenez, B., and Lacal, J. C. Phosphorylcholine: a novel second messenger essential for mitogenic activity of growth factors. *Oncogene*, **8**: 2959–2968, 1993.
- Exton, J. H. Phosphatidylcholine breakdown and signal transduction. *Biochim. Biophys. Acta*, **1212**: 26–42, 1994.
- Pelech, S. L., and Vance, D. E. Signal transduction via phosphatidylcholine cycles. *Trends Biochem. Sci.*, **14**: 28–30, 1989.
- Cai, H., Erhardt, P., Troppmair, J., Diaz-Meco, M. T., Sithanandam, G., Rapp, U. R., Moscat, J., and Cooper, G. M. Hydrolysis of phosphatidylcholine couples Ras to activation of Raf protein kinase during mitogenic signal transduction. *Mol. Cell. Biol.*, **13**: 7645–7651, 1993.
- Exton, J. H. Cell signalling through guanine-nucleotide-binding regulatory proteins (G proteins) and phospholipases. *Eur. J. Biochem.*, **243**: 10–20, 1997.
- Carnero, A., Cuadrado, A., del Peso, L., and Lacal, J. C. Activation of type D phospholipase by serum stimulation and ras-induced transformation in NIH3T3 cells. *Oncogene*, **9**: 1387–1395, 1994.
- Ratnam, S., and Kent, C. Early increase in choline kinase activity upon induction of the H-ras oncogene in mouse fibroblast cell lines. *Arch. Biochem. Biophys.*, **323**: 313–322, 1995.
- Mackinnon, W. B., Barry, P. A., Malycha, P. L., Gillett, D. L., Russell, P., Lean, C. L., Doran, S. T., Barraclough, B. H., Bilous, M., and Mountford, C. Fine-needle biopsy specimen of benign breast lesions distinguished from invasive cancer *ex vivo* with proton MR spectroscopy. *Radiology*, **204**: 661–666, 1997.
- Podo, F. Detection of phosphatidylcholine-specific phospholipase C in NIH-3T3 fibroblast and H-ras transformants: NMR and immunochemical studies. *Anticancer Res.*, **19**: 1399–1412, 1996.
- Ruiz-Cabello, J., and Cohen, J. S. Phospholipid metabolites as indicators of cancer cell function. *NMR Biomed.*, **5**: 226–233, 1992.
- Rutter, A., Mackinnon, W. B., Huschtscha, L. I., and Mountford, C. E. A proton magnetic resonance spectroscopy study of aging and transformed human fibroblasts. *Exp. Gerontol.*, **31**: 669–686, 1996.
- Ting, Y-L. T., Sherr, D., and Degani, H. Variations in energy and phospholipid metabolism in normal and cancer human mammary epithelial cells. *Anticancer Res.*, **16**: 1381–1388, 1996.
- Stampfer, M. R., and Bartley, J. C. Induction of transformation in continuous cell lines from normal human mammary epithelial cells after exposure to benzo(a)pyrene. *Proc. Natl. Acad. Sci. USA*, **82**: 2394–2398, 1985.
- Pierce, J. H., Arnstein, P., DiMarco, E., Artrip, J., Kraus, M. H., Lonardo, F., DiFiore, P. P., and Aaronson, S. A. Oncogenic potential of erbB-2 in human mammary epithelial cells. *Oncogene*, **6**: 1189–1194, 1991.
- Thompson, E. W., Torri, J., Sabol, M., Sommers, C. L., Byers, S., Valverius, E. M., Martin, G. R., Lippman, M. E., Stampfer, M. R., and Dickson, R. B. Oncogene-induced basement membrane invasiveness in human mammary epithelial cells. *Clin. Exp. Metastasis*, **12**: 181–194, 1994.
- Valverius, E., Bates, S. E., Stampfer, M., Clark, R., McCormick, F., Salomon, D. S., Lippman, M. E., and Dickson, R. B. Transforming growth factor  $\alpha$  and its receptor in human mammary epithelial cells: modulation of epidermal growth factor receptor function with oncogenic transformation. *Mol. Endocrinol.*, **3**: 203–214, 1989.
- Smith, L. M., Birrer, M. J., Stampfer, M. R., and Brown, P. H. Breast cancer cells have lower activating protein 1 transcription factor activity than normal mammary epithelial cells. *Cancer Res.*, **57**: 3046–3054, 1997.
- Stampfer, M. R., Bodnar, A., Garbe, J., Wong, M., Pan, A., Villeponteau, B., and Yaswen, P. Gradual phenotypic conversion associated with immortalization of cultured human mammary epithelial cells. *Mol. Biol. Cell*, **8**: 2391–2405, 1997.
- Stampfer, M. R. Isolation and growth of human mammary epithelial cells. *J. Tissue Culture Methods*, **9**: 107–116, 1985.
- Stampfer, M. R., and Yaswen, P. Culture systems for study of human mammary epithelial cell proliferation, differentiation and transformation. *Cancer Surv.*, **18**: 7–34, 1994.
- Paine, T. M., Soule, H. D., Pauley, R. J., and Dawson, P. J. Characterization of epithelial phenotypes in mortal and immortal human breast cells. *Int. J. Cancer*, **50**: 463–473, 1992.
- Plumb, J. A., Milroy, R., and Kaye, S. B. Effects of pH dependence of 3-(4,5-dimethylthiazole-2-yl)-2,5-diphenyltetrazolium bromide-formazan absorption on chemosensitivity determined by a novel tetrazolium-based assay. *Cancer Res.*, **49**: 4435–4440, 1989.
- Negendank, W. Studies of human tumors by MRS: a review. *NMR Biomed.*, **5**: 303–324, 1992.
- Smith, T. A. D., Eccles, S., Ormerod, M. G., Tombs, A. J., Titley, J. C., and Leach, M. O. The phosphocholine and glycerophosphocholine content of oestrogen-sensitive rat mammary tumor correlates strongly with growth rate. *Br. J. Cancer*, **64**: 821–826, 1991.
- Dickson, R. B., Salomon, D. S., and Lippman, M. E. Tyrosine kinase receptor-nuclear protooncogene interaction in breast cancer. *Cancer Treat. Res.*, **61**: 249–273, 1992.
- Beckman, M. W., Niederacher, D., Schnurch, H. G., Guesterson, B. A., and Bender, H. G. Multistep carcinogenesis of breast cancer and tumor heterogeneity. *J. Mol. Med.*, **77**: 429–437, 1993.
- Adnane, J., Gaudray, P., Simon-Lafontaine, J., Jeanteur, P., and Theillet, C. Proto-oncogene amplification and breast cancer phenotype. *Oncogene*, **4**: 1389–1395, 1989.
- Slamon, D. J., Clark, G. M., Wong, S. G., Levin, W. J., Ullrich, A., and McGuire, W. L. Human breast cancer: correlation of relapse and survival with amplification of the HER-2/neu oncogene. *Science (Washington DC)*, **235**: 177–182, 1987.
- de Cremoux, P., Gauville, C., Closson, V., Linares, G., Calvo, F., Tavitian, A., and Olofsson, B. EGF modulation of the *ras*-related *rhoB* gene expression in human breast cancer cell lines. *Int. J. Cancer*, **59**: 408–415, 1994.
- Daly, R. J., Binder, M. D., and Sutherland, R. L. Overexpression of the *Grb* gene in human breast cancer cell lines. *Oncogene*, **9**: 2723–2727, 1994.
- Tadokoro, K., Ishidate, K., and Nakazawa, Y. Evidence for the existence of isozymes of choline kinase and their selective induction in 3-methylcholanthrene- or carbon tetrachloride-treated rat liver. *Biochim. Biophys. Acta*, **835**: 501–513, 1985.

# In Vivo Imaging of Extracellular pH Using $^1\text{H}$ MRSI

• Robert van Sluis,<sup>1</sup> Zaver M. Bhujwalla,<sup>2</sup> Natarajan Raghunand,<sup>1</sup> Paloma Ballesteros,<sup>3</sup> José Alvarez,<sup>4</sup> Sebastián Cerdán,<sup>4</sup> Jean-Philippe Galons,<sup>1</sup> and Robert J. Gillies<sup>1\*</sup>

**Tumor pH is physiologically important since it influences a number of processes relevant to tumorigenesis and therapy.** Hence, knowledge of localized pH within tumors would contribute to understanding these processes. The destructiveness, poor spatial resolution, and poor signal-to-noise ratio (SNR) of current technologies (e.g., microelectrodes,  $^{31}\text{P}$  magnetic resonance spectroscopy) have limited such studies. An extrinsic chemical extracellular pH ( $\text{pH}_e$ ) probe is described that is used in combination with  $^1\text{H}$  magnetic resonance spectroscopic imaging to yield  $\text{pH}_e$  maps with a spatial resolution of  $1 \times 1 \times 4 \text{ mm}^3$ . The principle of the technique is demonstrated on a phantom. Further data are shown to demonstrate its application *in vivo*, and results agree with previously reported pH values. The accuracy of the reported pH measurements is  $<0.1 \text{ pH}$  units, as derived from a detailed analysis of the errors associated with the technique, the description of which is included. *Magn Reson Med* 41:743–750, 1999. © 1999 Wiley-Liss, Inc.

**Key words:** cancer; imidazole; MRSI; pH; tumor

Since the discovery of lactic acid production in tumors more than 50 years ago (1), it has generally been assumed that the pH of tumors is acidic. Indeed, numerous microelectrode measurements have shown that extracellular tumor pH ( $\text{pH}_e$ ) is acidic (2). This acidic  $\text{pH}_e$  of tumors has been confirmed with less invasive  $^{31}\text{P}$  magnetic resonance spectroscopy (MRS) measurements (3). Although the intracellular pH ( $\text{pH}_i$ ) of tumors remains neutral to alkaline (4,5), it is somewhat influenced by the  $\text{pH}_e$  (6).

An acidic pH<sub>e</sub> of tumors is physiologically important since it influences a number of processes relevant to carcinogenesis and therapy. Knowledge of localized pH within tumors, both intra- and extracellular, would allow more detailed study of these processes and relate them to intratumoral pH heterogeneity. For example, it has been found that low  $\text{pH}_e$  *in vitro* causes tumorigenic transformation of primary Syrian hamster embryo cells (7) and can lead to chromosomal rearrangements in Chinese hamster embryo cells (8,9). Furthermore, culturing cells at low pH causes them to be more invasive *in vitro* (10) and metastatic *in vivo* (11). Finally, the orientation of the pH

gradient across the cell membrane may influence cell drug resistance (6,12).

Previously reported measurements of extracellular pH using either microelectrodes or  $^{31}\text{P}$  MRS of 3-aminopropylphosphonate (3-APP) (3) have drawbacks. Microelectrodes are invasive and can destroy the membrane integrity, thereby disrupting the mechanism for maintaining the  $\text{pH}_e$ .  $^{31}\text{P}$  MRS does not suffer this drawback and has the additional advantage of permitting simultaneous measurements of intracellular pH. However, the limited sensitivity of  $^{31}\text{P}$  MRS allows measurements of  $\text{pH}_e$  only from relatively large tissue volumes. Hence,  $^{31}\text{P}$  MRS provides measurements of pH ranges rather than different pH values for discrete spatial locations (13).

The use of  $^1\text{H}$  MRS, inherently more sensitive than  $^{31}\text{P}$  MRS, would allow measurements of pH over smaller tissue volumes. For example, the imidazole protons of histidine have long been useful as intracellular pH indicators in NMR (14,15).

Rabenstein and Isab (16) first proposed using imidazoles as extrinsic  $\text{pH}_e$  indicators. Gil et al (17) suggested several modifications of the basic structure of the imidazole molecule to improve its performance as an extrinsic pH probe. To date, the most promising candidate for a  $^1\text{H}$  nuclear magnetic resonance (NMR)-sensitive  $\text{pH}_e$  indicator is the H2 resonance of ( $\pm$ ) 2-imidazole-1-yl-3-ethoxycarbonyl propionic acid (IEPA), which has been shown to remain in the extracellular environment (17). Results from toxicity studies and preliminary *in vivo* data using IEPA have been reported previously (18,19).

Here, we present both phantom and *in vivo* data that demonstrate the feasibility of localized, multi-voxel  $\text{pH}_e$  measurements using  $^1\text{H}$  magnetic resonance spectroscopic imaging (MRSI). Furthermore, a detailed discussion of the sources and (where possible) the quantification of errors associated with the proposed measurement technique is included.

## MATERIALS AND METHODS

### Titration of IEPA

Titration data for IEPA were obtained from bovine serum containing 20 mM IEPA, to which 20 mM EDTA and 10% v/v deuterium oxide ( $\text{D}_2\text{O}$ ) were added for preservation and shimlock purposes, respectively. As a chemical shift reference, 10 mM 3-(trimethylsilyl) tetradecanoate (TSP) was also added. The pH of the solution was adjusted at 37°C using 5 N solutions of NaOH and HCl to 19 pH values between 4.7 and 8.0 and the chemical shift of the H2 IEPA resonance was measured at 37°C in the spectrum for each pH value. Figure 1 shows the chemical structure and a high-resolution (9.4 T)  $^1\text{H}$  spectrum of IEPA at pH 7.0.

<sup>1</sup>Departments of Biochemistry and Radiology, The University of Arizona, Tucson, Arizona.

<sup>2</sup>Department of Radiology, Johns Hopkins University School of Medicine, Baltimore, Maryland.

<sup>3</sup>Department of Chemistry, UNED, Madrid, Spain.

<sup>4</sup>Magnetic Resonance Laboratory, IIB CSIC, Madrid, Spain.

Grant sponsor: US Army Breast Cancer Initiative; Grant numbers: DAMD17-94-J-4368, DAMD17-96-1-6131, PB93-0037, and PB94-011.

Presented in part at the 1998 meeting of the ISMRM, Sydney, Australia, poster #1642.

\*Correspondence to: Robert J. Gillies, The University of Arizona Health Sciences Center, PO Box 245042, Tucson, AZ 85724-5042.

E-mail: gillies@u.arizona.edu

Received 19 June 1998; revised 5 October 1998; accepted 5 October 1998.

© 1999 Wiley-Liss, Inc.

The Henderson-Hasselbalch equation for IEPA is given by

$$\text{pH} = \text{pK}_a - \log_{10} \left( \frac{\delta_{\text{obs}} - \delta_{\text{acid}}}{\delta_{\text{base}} - \delta_{\text{obs}}} \right), \quad [\text{Eq. 1}]$$

where pH is the observed pH,  $\text{pK}_a$  is the negative  $\log_{10}$  of the acid dissociation constant, and  $\delta_{\text{obs}}$ ,  $\delta_{\text{acid}}$ , and  $\delta_{\text{base}}$  are the chemical shifts of the observed, the fully protonated, and the fully deprotonated IEPA peaks, respectively. The experimental data were fitted to Eq. [1] through nonlinear regression (SigmaPlot 3.0, Jandel), and the results are shown in Fig. 2. The fit is characterized by the following set of parameters and their respective standard errors:

$$\text{pK}_a = 6.49 \pm 0.02;$$

$$\delta_{\text{acid}} = 8.92 \pm 0.01;$$

$$\delta_{\text{base}} = 7.77 \pm 0.01.$$

### MRSI Experiments

All MRSI experiments were performed on a 4.7 T GE Omega scanner, using the BASSALE sequence (20) and a two-turn  $^1\text{H}$  surface coil. Two-dimensional (2D) water-suppressed MRSI data were obtained from a 4 mm coronal slice, phase-encoding dimensions of  $2 \times 2 \text{ mm}^2$  and 16  $\times$  16 steps. The fields of view (FOVs) in all imaging and MRSI studies were  $32 \times 32 \text{ mm}^2$ .

A three-compartment phantom was constructed, consisting of two 5 mm NMR tubes inside a larger, 12 mm glass cylinder. The two inner tubes were filled with 20 mM IEPA at pH values of 6.5 and 7.5, respectively. The third, outer compartment was filled with saline.  $^1\text{H}$  MRSI data were acquired with a TE of 100 msec, TR of 2 sec, 512 points, spectral width (SW) of 6000 Hz, 4 averages. A separate data set was obtained without water suppression to correct for susceptibility effects.

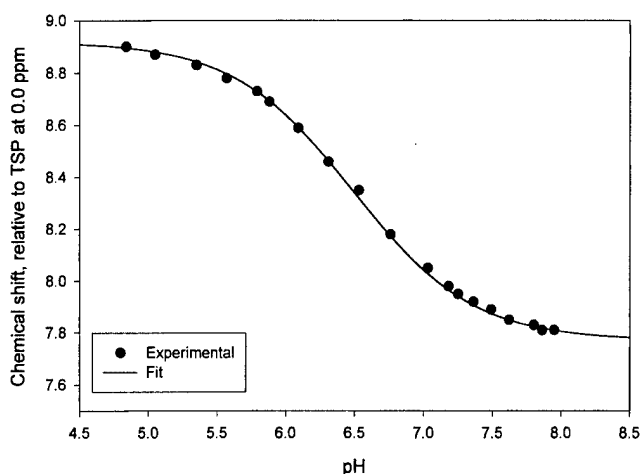


FIG. 2. Chemical shift of the H2-IEPA resonance relative to TSP, as a function of pH in bovine serum at 37°C. Measured data are shown as points, and the curve results from a nonlinear regression of the experimental data to Eq. [2].

In vivo studies were performed on human breast cancer cells (MCF-7 and MDA<sup>mb</sup>-435), grown in the mammary fat pad of severe combined immunodeficient (SCID) mice. Tumor volumes studied were 300–600 mm<sup>3</sup>. The mice were anesthetized with ketamine (50 mg/kg) and acepromazine (5 mg/kg), and 0.15 ml of a 310 mM IEPA solution was injected intra-peritoneally. The animals were immobilized on a home-built MR cradle, and body temperature was maintained using a warm water blanket.  $^1\text{H}$  MRSI data were acquired with a TE of 32 msec, TR of 2 sec, 128 points, SW of 6000 Hz, and 8 averages. The total measurement time was 34 min. A separate data set was obtained without water suppression to correct for susceptibility effects.

All data were processed using an MRSI processing program, developed in-house and written in Interactive Data Language (IDL, Research Systems, Boulder, CO). The raw  $^1\text{H}$  MRSI data were Hanning filtered in  $k$ -space, and zero filled once in both  $k$ -space and in the time domain prior to 3D Fourier transformation.

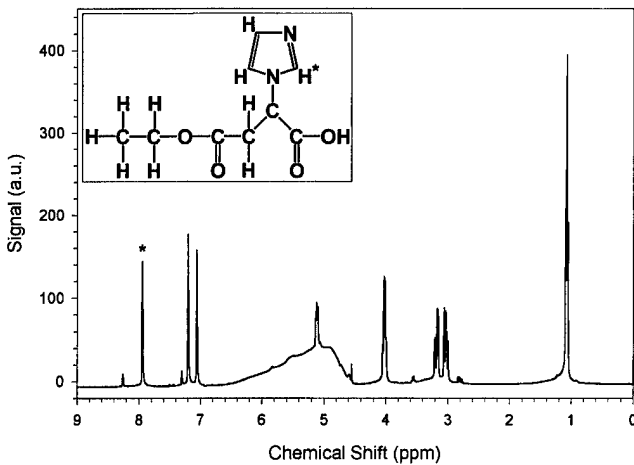


FIG. 1. Structure and 9.4 T  $^1\text{H}$  NMR spectrum of IEPA in solution (pH 7.0). The pH-sensitive resonance and the C2 proton from which it originates are indicated by asterisks. The broad resonance in the center of the spectrum is due to residual water.

### RESULTS AND DISCUSSION

#### Phantom Data

The chemical shift of the H2 resonance of IEPA was determined for the maximum peak occurring between 7.77 and 8.92 ppm (the H2 proton titratable range) in each of the MRSI spectra. Chemical shifts in each voxel were referenced to unsuppressed water at 4.7 ppm to correct for susceptibility effects, and converted to pH values using Eq. [1]. The pH values from each voxel were color-encoded. Peaks lower than 10% of the maximum IEPA intensity were discarded, and results are shown in Fig. 3.

It is clear from Fig. 3b that the pH imaging technique allows the two compartments of the phantom to be distinguished. Furthermore, the reported pH values are in good agreement with the calibration values of 6.5 and 7.5 pH units. Note that the pH 6.5 compartment is spread over more voxels than the pH 7.5 compartment. Over the pH range 5–8, the  $T_2$  of the C2 proton of IEPA decreases from  $101 \pm 12$  msec to  $61 \pm 4$  msec. In spin-echo sequences like

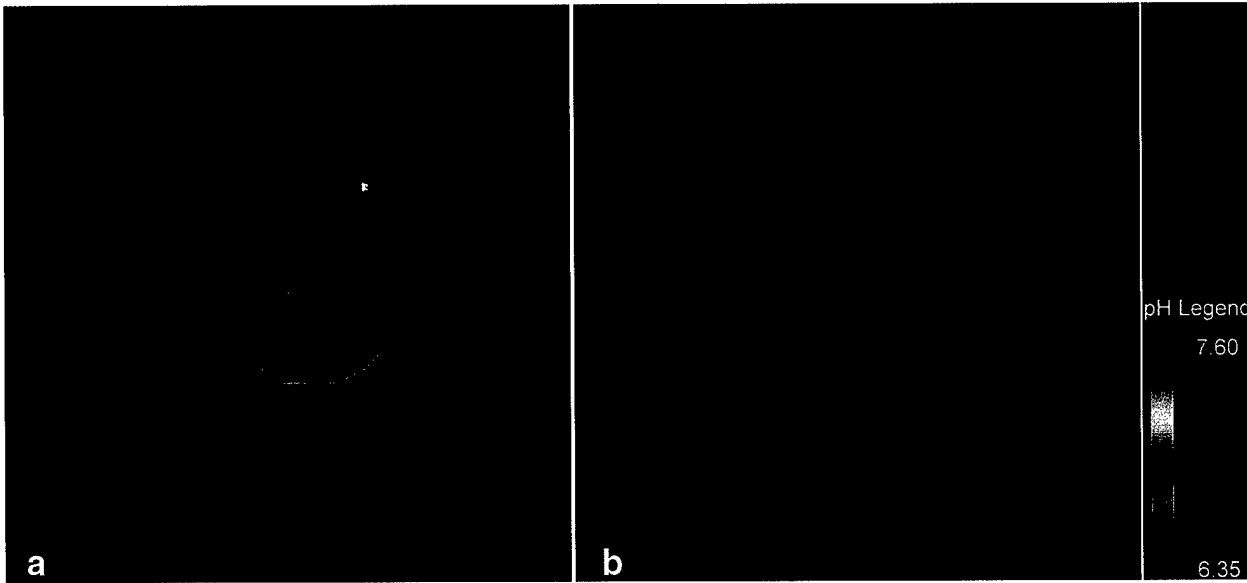


FIG. 3. **a:** Coronal image through the three compartment phantom, showing the two tubes with pH 6.5 (bottom left) and pH 7.5 (top right). The bright spot is a capillary filled with Gd-DTPA, used for orientation purposes. **b:** pH map and legend for the phantom. The pixel size in the pH map is 1 mm<sup>2</sup>.

BASSALE, resonances with a longer  $T_2$  will have a higher signal intensity than resonances with a shorter  $T_2$ . Since the  $T_2$  of the C2 proton of IEPA decreases with increased pH, the H2-IEPA resonance from the lower pH compartment will have a higher intensity than the H2-IEPA resonance from the higher pH compartment. The degree of contamination due to the point spread function (PSF) is proportional to the intensity of the signal from which the contamination arises (21). As a result the contamination for the pH 6.5 compartment extends over more neighboring voxels compared with the pH 7.5 compartment. Furthermore, this  $T_2$  weighting could lead to an underestimate of the reported pH value. The decrease of  $T_2$  with increasing pH is consistent with the known increase in the exchange rate with solvent of protons from primary and secondary amines and amides (22). Increasing solvent exchange rate would tend to decrease  $T_2$  values of the imidazolic protons because of an increased magnetization transfer to the surrounding solvent. Regardless of the exact underlying mechanisms of the  $T_2$  dependence on pH, it is clear that <sup>1</sup>H MRSI of the H2 proton of IEPA allows us to produce a pH map of the phantom and distinguish between the two compartments, as shown in Fig. 3.

#### In Vivo Data

An illustration of the quality of our in vivo MRSI data, an array of 7 × 7 spectra, is shown in Fig. 4. These data demonstrate that the H2 resonance of IEPA is observable with good SNR in 15–20 voxels in the tumor. Pre-injection spectra contain a small resonance in the 7–9 ppm region corresponding to endogenous imidazole (data not shown). This resonance was smaller than that in, for example, voxel (9,12), and did not affect subsequent measurements.

Some voxels, in particular [10,8], [10,9], and [10,10], bracketed in Fig. 4, show the presence of a complex H2-IEPA resonance, which may result from the presence of two or more pools of distinct  $pH_e$  values. In all spectra, the

H2-IEPA resonance is rather broad. The short  $T_2^*$  of this resonance in vivo does not allow a finer sampling of the spectrum without ramifications for the SNR. At present, the optimum spectral sampling interval is 0.23 ppm/point, which is coarse. Clearly, this is an aspect of the work that needs improvement.

For construction of the  $pH_e$  map from the in vivo data, the chemical shift of the H2 resonance of IEPA was determined using a center of gravity (COG) calculation (23) over the titratable chemical shift range for this proton. The calculation was weighted by the shape of the titration curve to correct for its non-linearity (24). Over the titratable range of the IEPA C2 proton, the weighting function is the partial derivative of the observed chemical shift with respect to the pH for Eq. [1], and is given by:

$$\frac{\partial \delta_{\text{obs}}}{\partial \text{pH}} = \frac{2.3(\delta_{\text{acid}} - \delta_{\text{obs}})(\delta_{\text{obs}} - \delta_{\text{base}})}{(\delta_{\text{acid}} - \delta_{\text{base}})} \quad [\text{Eq. 2}]$$

Outside the titratable range, the weighting function is zero. As before, chemical shift values were references to unsuppressed water at 4.7 ppm to correct for susceptibility effects and the calculated pH values were color-encoded. Peaks lower than 10% of the maximum IEPA intensity were discarded. Results are shown in Fig. 5.

The intensity of the H2-IEPA resonance is the largest in the center of the tumor (Fig. 5a). Since tumor perfusion is generally worse in the center of a tumor than in the periphery, one would expect to find a higher concentration of IEPA in the periphery of the tumor compared with the center. However, the observed intensity distribution is likely to be caused by the application of the Hanning filter to the raw data. This filter reduces the signal intensity at the edges of the FOV, to reduce ringing artifacts. As a result, data in the center of the FOV appear to be at a higher intensity.

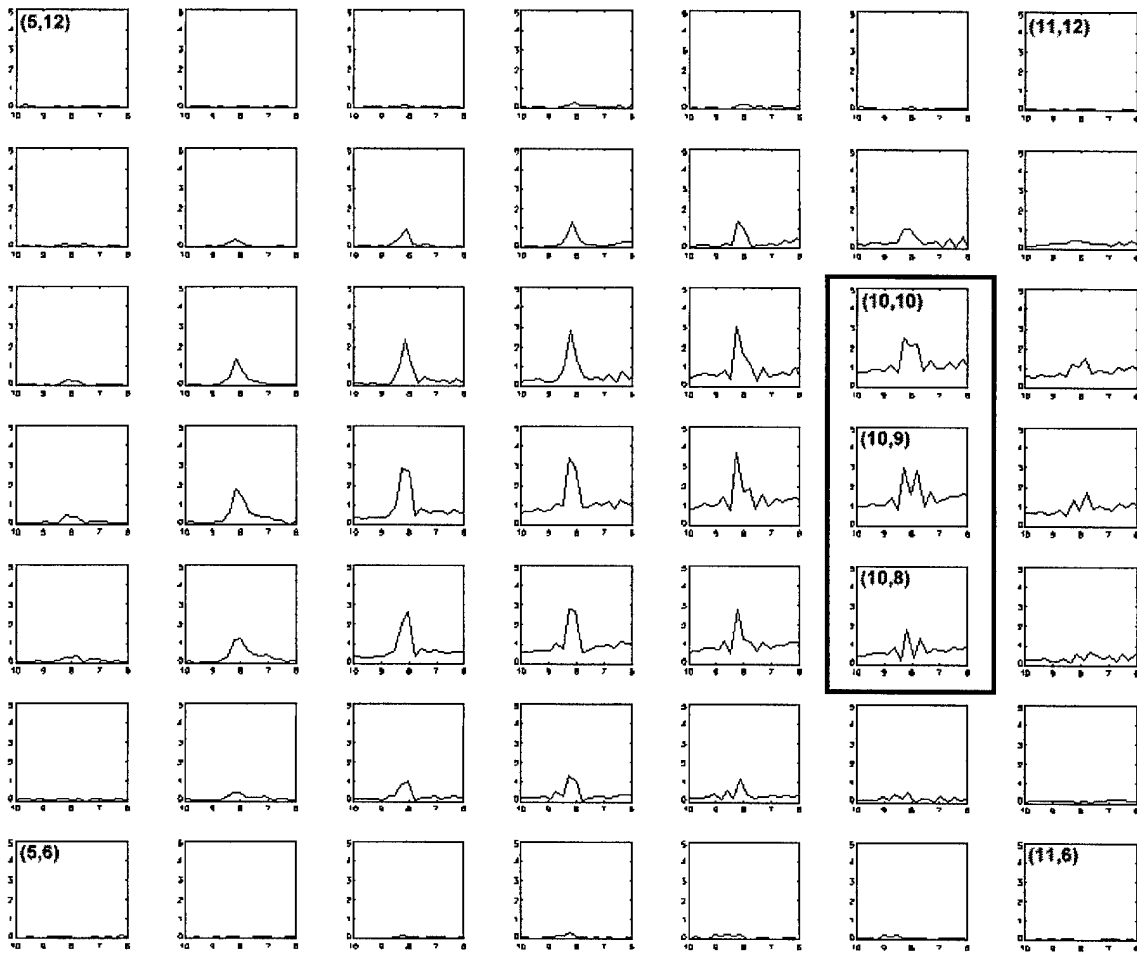


FIG. 4. Array of  $7 \times 7$  *in vivo*<sup>1</sup>H MRSI spectra used for the determination of  $pH_e$  in the tumor. The H<sub>2</sub>-IEPA resonance is clearly visible in the majority of the spectra. The displayed chemical shift range is 10–6 ppm. Note that for these spectra, the voxel size is  $2 \times 2 \text{ mm}^2$ . For construction of the  $pH_e$  map, data were interpolated in  $k$ -space to yield a voxel size of  $1 \text{ mm}^2$ . The boxed spectra, [10,8], [10,9], and [10,10] are discussed in detail in the text.

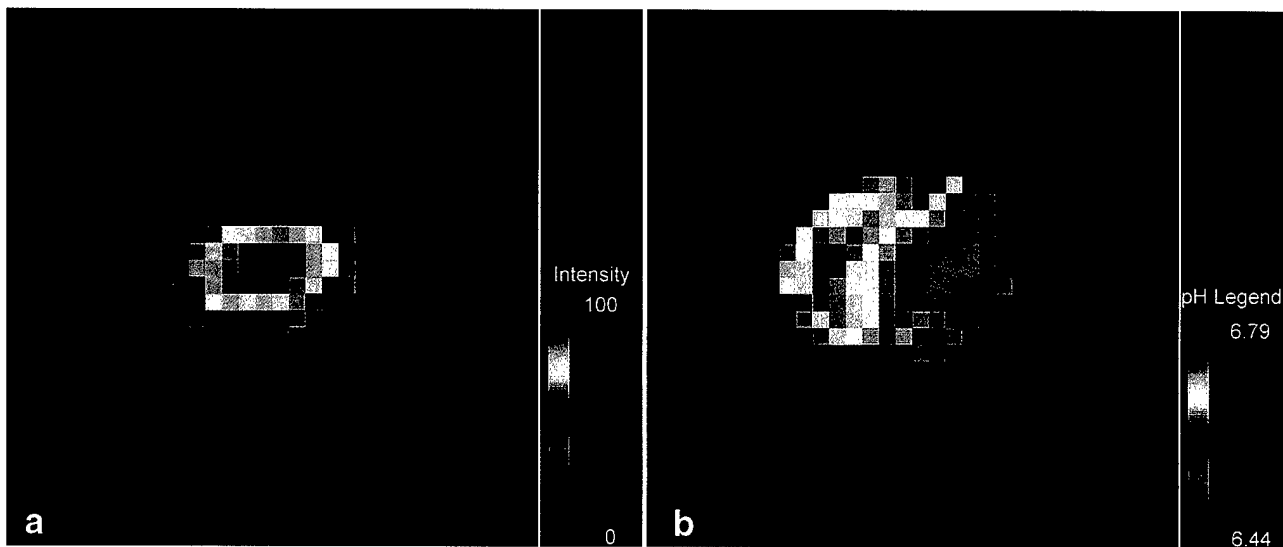


FIG. 5. **a:** Intensity map of the H<sub>2</sub>-resonance of IEPA in a coronal slice through an MDA<sup>mb</sup>-435 tumor. **b:** Corresponding  $pH_e$  map. In both the intensity and  $pH_e$  map, the pixel size is  $1 \text{ mm}^2$ .

As expected, the data show a good correlation between the signal intensity distribution and the extent of the  $pH_e$  map (cf. Fig. 5a and b). Across the tumor, the observed extracellular pH in the tumor is heterogeneous and acidic ( $6.44 < pH_e < 6.79$ ), with a volume average  $pH_e$  of  $6.64 \pm 0.07$ . This is in good agreement with previous studies (13). Furthermore, it is seen that there are several discrete areas of fairly homogeneous  $pH_e$  within the tumor, with areas between 4 and  $9\text{ mm}^2$  (Fig. 5b). The largest continuous area within the tumor appears to have an average  $pH_e$  of 6.6, as read from the legend.

### Error Analysis

The pH ranges as reported in Figs. 3b and 5b have associated errors resulting from artifacts in the measurement technique. The errors associated with the calibration of the  $pH_e$  are relatively small (see above), so that the measurement technique proposed above has two remaining sources of error to be considered. First, the COG method used in determining the peak position will have an accuracy dependent on the linewidth and SNR of the peak under observation. Second, signal modulation due to the PSF, an inherent source of error in any MRSI measurement (21), will cause signals to "bleed" into adjacent voxels. This voxel bleed artifact depends on the intensity and chemical shift differences existing between adjacent voxels. Intensity differences may be caused by changes in the IEPA relaxation times with pH or by differences in IEPA concentration between adjacent voxels. Chemical shift differences between voxels may be caused by  $pH_e$  differences. These sources of error will be described in more detail below.

### Accuracy of the COG Method

To study the accuracy of the COG method for determination of pH from our spectra, we simulated C2 IEPA resonances for pH values 6.0, 6.5, 7.0, and 7.5, with a spectral resolution of 0.23 ppm/point. Resonances were simulated with different linewidths as defined by the full width at half-maximum (FWHM). Gaussian noise was added to the IEPA resonance to yield SNRs of approximately 20, 10, and 5. The pH as determined by the COG method was compared with the pH as entered into the simulation and the absolute error gives a measure of the accuracy of the COG method in determining the pH. Results are shown in Fig. 6.

The error in the reported pH increases with decreasing SNR, for all linewidths, as expected. Furthermore, the pH is reported more accurately near the  $pK_a$  of the C2 IEPA proton, which is 6.49. This is due to the nonlinearity of the titration curve.

It is also observed that the error in the reported pH increases as the H<sub>2</sub>-IEPA resonance linewidth decreases (see Fig. 6a and 6c). This is directly related to the spectral resolution in the simulated data (0.23 ppm/point). As peaks narrow, the lines are defined by fewer and fewer points, and with the FWHM approaching the spectral resolution, the determination of the position of the maximum peak intensity by the COG method becomes stochastic. However, for reasonable SNRs (>5) and broader peaks (FWHM > 0.16 ppm), as observed in our in vivo spectra,

the accuracy of the COG method is better than 0.1 pH units in the range from pH 6.0 to pH 7.0.

### Modeling PSF Artifacts

Wang et al (25) have proposed a model to calculate voxel bleed artifacts due to concentration differences alone. Here, we have modified their model to study the combined effects of inhomogeneities in both  $pH_e$  and IEPA concentration.

For simulations, an  $8 \times 8$  grid of IEPA free induction decays (FIDs) was established, with voxel coordinates running from [0,0] to [7,7]. In the descriptions below, voxel [4,4] was used as the "center voxel". Initial simulations demonstrated that the worst contamination occurs in the center voxel when the signal intensity ratio is maximum, i.e., an empty voxel surrounded by voxels of non-zero IEPA concentration. Also, the contamination is worst between nearest neighbor voxels, i.e., the main contributors to the contamination in the center voxel are the 8 voxels immediately surrounding it. These results are in agreement with those of Wang et al (25).

Quantitative estimates of the actual degrees of IEPA concentration and  $pH_e$  inhomogeneities *in vivo* are required before continuing analysis of their effects on the precision of the proposed pH imaging technique.

### Estimating IEPA Concentration Inhomogeneity

Since voxel bleed artifacts prevent direct derivation of quantitative information on IEPA concentration inhomogeneity from the MRSI data, studies of the uptake of dimeglumine gadopentetate (Gd-DTPA, Schering, Germany) in MCF-7 tumors were monitored by T<sub>2</sub>-weighted imaging as a model for the IEPA concentration distribution. IEPA and Gd-DTPA are comparable in terms of partition coefficient and charge. Both molecules are about the same size, and their charges are -2 for Gd-DTPA (Gd +3, DTPA -5) and 0 to -1 for IEPA (acid group -1, imidazolic nitrogen +0 to +1).

One precontrast ( $t = 0$ ) and 16 Gd-DTPA-enhanced images (17 mm surface coil, FOV 25 mm<sup>2</sup>, 128 × 128 pixels, slice thickness 4 mm) were obtained at regular intervals over the course of 110 min from three consecutive sagittal slices through MCF-7 tumors. Gd-DTPA-enhanced images were subtracted from the precontrast image to yield images of the Gd-DTPA enhancement only, which to a first approximation is linear with Gd-DTPA concentration (26). These subtraction images were rebinned to 16 × 16 pixels to yield a pixel size of 1.56 mm<sup>2</sup>, approximating the 2 mm<sup>2</sup> spatial resolution used when acquiring the IEPA MRSI data. Examples of a high-resolution (128 × 128) and rebinned (16 × 16) images of Gd-DTPA enhancement are shown in Fig. 7.

In each of the rebinned subtraction images, 6 pixels were identified that represent the Gd-DTPA distribution in the tumor and, for these 6 pixels, the intensity ratios between nearest neighbors were calculated. The highest and the average nearest neighbor intensity ratios were determined for each image and plotted as a function of time, as shown in Fig. 8. It can be seen that once a steady-state Gd-DTPA concentration has been reached (after 6–8 min), the highest and average intensity ratios stabilize at about 1:3.0 and 1:1.5, respectively. Using these values as a measure of the

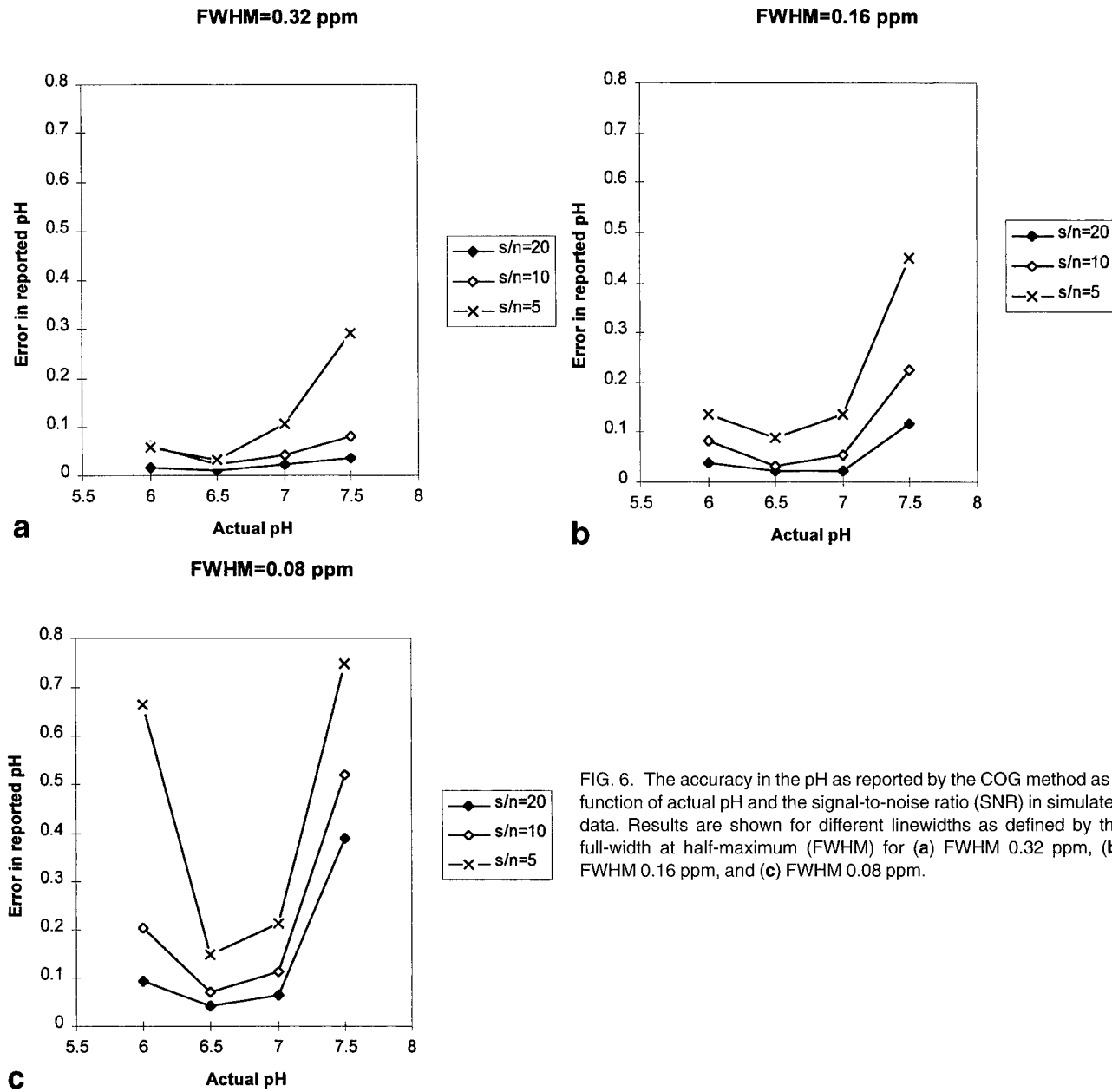


FIG. 6. The accuracy in the pH as reported by the COG method as a function of actual pH and the signal-to-noise ratio (SNR) in simulated data. Results are shown for different linewidths as defined by the full-width at half-maximum (FWHM) for (a) FWHM 0.32 ppm, (b) FWHM 0.16 ppm, and (c) FWHM 0.08 ppm.

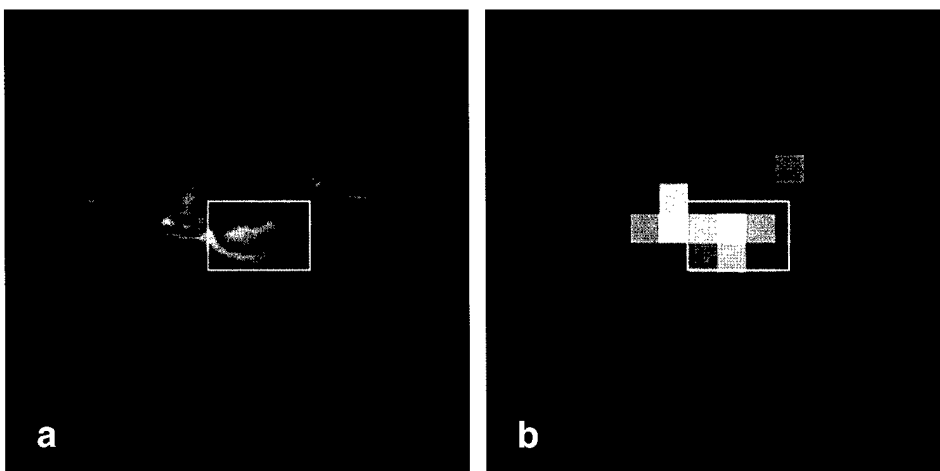


FIG. 7. **a:** High-resolution ( $128 \times 128$  pixels) subtraction image of Gd-DTPA uptake in an MCF-7 tumor *in vivo*. **b:** The same image, rebinned to  $16 \times 16$  pixels. The resulting pixel size ( $1.56 \text{ mm}^2$ ) approximates the  $2 \text{ mm}^2$  spatial resolution used when acquiring IEPA MRSI data. In both images, the white box indicates the location of the tumor. The six pixels entirely within the tumor in **b** were used to calculate concentration differences between adjacent voxels.

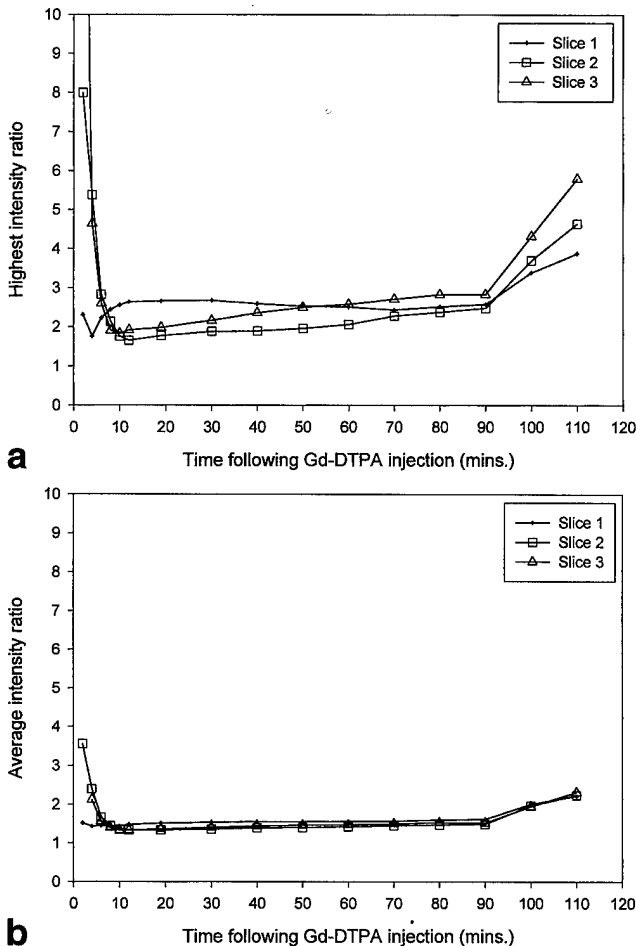


FIG. 8. The nearest neighbor highest (a) and average (b) intensity ratio as a function of time following Gd-DTPA injection in MCF-7 tumors.

IEPA intensity ratios between adjacent voxels, a simulated IEPA distribution was set up over the previously mentioned grid of  $8 \times 8$  voxels.

#### Quantifying $pH_e$ Inhomogeneity

Information on the maximum spatial  $pH_e$  gradient expected for adjacent voxels in the MRSI data was obtained through the work of Helmlinger et al (27), who reported a 0.7 unit  $pH_e$  difference between well-oxygenated (near the blood vessel) and nonoxygenated regions (away from the blood vessel) in tumors, over a distance of 400  $\mu\text{m}$ . This is in good agreement with work by Raghunand et al (13), who found that 85% of tumor  $pH_e$  values are within  $\pm 0.4$  pH units of the mean  $pH_e$ . To observe a pH difference of 0.7 pH units between adjacent  $16 \text{ mm}^3$  voxels in our MRSI data, it is necessary to have a fully oxygenated voxel (i.e., full of capillaries) immediately next to nonoxygenated voxels (i.e., no capillaries). It would be possible to find completely nonoxygenated voxels *in vivo*, for example, in necrotic areas. However, since in general tumor cells divide faster than their surrounding vasculature, the presence of a voxel consisting entirely of capillaries would be less likely. Therefore, we have chosen to work with the average  $pH_e$  range observed by both Helmlinger et al and

Raghunand et al (i.e., 0.4 pH unit), as the maximum pH gradient between adjacent voxels.

#### Combined Effect of IEPA Concentration and $pH_e$ Inhomogeneity on COG Precision

The maximum pH differences, with signal intensity ratios of either 1:3.0 or 1:1.5, were inserted into the simulation program. The reported pH for the center and surrounding voxels were compared with the actual values. The difference between the actual pH value and the pH value reported by the simulation program expresses the error due to the voxel bleed artifact, as shown in Fig. 9. As expected, when the center voxel is surrounded by more acidic voxels, the reported pH for the center voxel is underestimated and vice versa.

The error in the reported pH for the center voxel over the physiological pH range (6.8–7.6 pH units) is less than 0.15 pH units for a *maximum* intensity ratio of 1:3.0, and less than 0.10 pH units for an *average* intensity ratio of 1:1.5, as shown in Fig. 9. This is an encouraging result for the

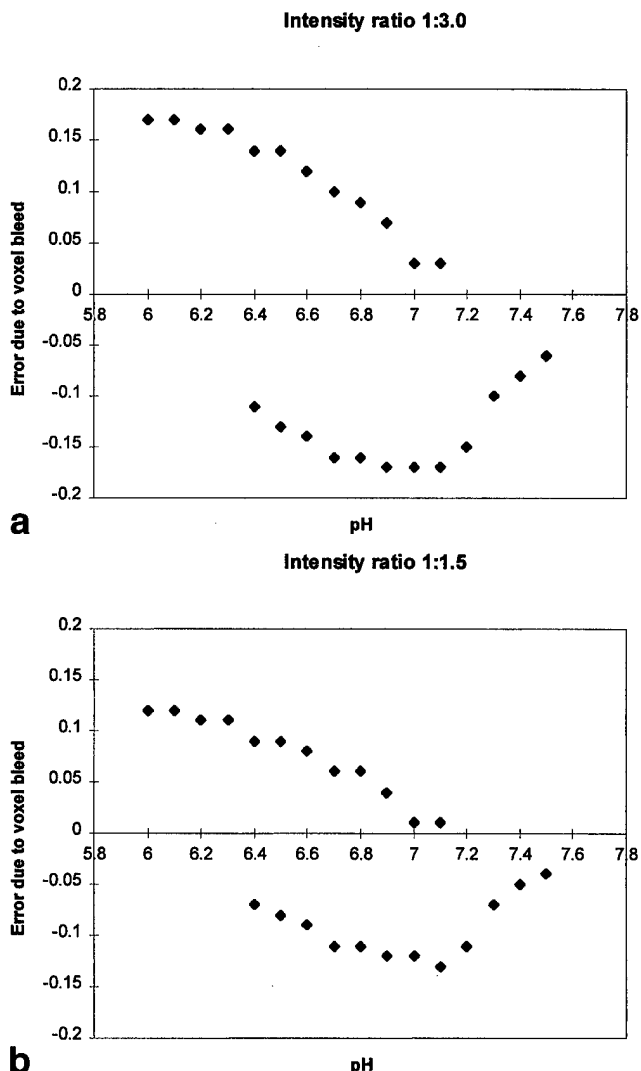


FIG. 9. The error due to the voxel bleed artifact for the center voxel as a function of pH and signal intensity ratio for (a) a signal intensity ratio of 1:3.0 and (b) 1:1.5.

precision of the proposed technique. Additionally, it must be remembered that these are worst-case scenarios. In practice, it is likely that the pH difference between adjacent voxels is less than 0.4 pH units, thus further reducing the error due to the voxel bleed artifact.

## CONCLUSIONS AND FUTURE DIRECTIONS

Using phantom and in vivo data, we have demonstrated the feasibility of imaging extracellular pH using  $^1\text{H}$  MRSI. The possible sources of error associated with the technique were analyzed in detail. It was found that the COG method leads to an error of <0.1 pH units for broader lines and reasonable SNR. For narrower lines, the poor spectral resolution increasingly reduces this accuracy. From simulations, it was found that artifacts due to voxel bleed in MRSI will introduce a maximum error of 0.1 pH units in the reported pH values. Finally, it was observed that the  $T_2$  of the proposed  $\text{pH}_e$  indicator is pH dependent. This dependence, its cause, and the effect on reported pH values are currently under investigation.

## ACKNOWLEDGMENTS

The authors thank D.C. Shungu, V.P. Chacko, and B. Baggett for their invaluable help with this work. Support from the US Army Breast Cancer Initiative DAMD17-94-J-4368 (to R.J.G.) and DAMD17-96-1-6131 (to Z.M.B.) and grants PB93-0037 (to P.B.) and PB94-011 (to S.C.) is gratefully acknowledged.

## REFERENCES

1. Warburg O. On the metabolism of tumors. Cambridge: Cambridge University Press; 1930.
2. Wike-Hooley JL, Haveman J, Reinhold HS. The relevance of tumor pH to the treatment of malignant disease. *Radiother Oncol* 1984;2:343–366.
3. Gillies RJ, Liu Z, Bhujwalla Z.  $^{31}\text{P}$  MRS measurement of extracellular pH of tumor using 3-aminopropylphosphonate. *Am J Physiol* 1994;267: C195–C203.
4. Negendank W. Studies of human tumors by MRS: a review. *NMR Biomed* 1992;5:303–324.
5. Griffiths JR. Are cancer cells acidic? *Br J Cancer* 1991;64:425–427.
6. Raghunand N, He X, van Sluis R, Bhujwalla ZM, Gillies RJ. Plasmalemmal pH gradients in drug-sensitive and drug-resistant MCF-7 human breast carcinoma tumors measured by  $^{31}\text{P}$  MRS. In: Proceedings of the ISMRM 6<sup>th</sup> Annual Meeting, Sydney, 1998. p 1644.
7. LeBoeuf RA, Kerckaert GA, Aardema MJ, Gibson DP. Multistage neoplastic transformation of Syrian hamster embryo cells cultured at pH 6.70. *Cancer Res* 1990;50:3722–3729.
8. Morita T, Takeda K, Okumura K. Evaluation of clastogenicity of formic acid, acetic acid and lactic acid on cultured mammalian cells. *Mutat Res* 1990;240:195–202.
9. Morita T, Nagaki T, Fukuda I, Okumura K. Clastogenicity of low pH to various cultured mammalian cells. *Mutat Res* 1992;268:297–305.
10. Martínez-Zaguirén R, Seftor EA, Seftor REB, Chu Y-W, Gillies RJ, Hendrix MJC. Acidic pH enhances the invasive behavior of human melanoma cells. *Clin Exp Metast* 1996;14:176–186.
11. Schlappack OK, Zimmermann A, Hill RP. Glucose starvation and acidosis: effect on experimental metastatic potential, DNA content and MTX resistance of murine tumour cells. *Br J Cancer* 1991;64:663–670.
12. Gerweck LE, Seetharaman K. Cellular pH gradient in tumor versus normal tissue: potential exploitation for the treatment of cancer. *Cancer Res* 1996;56:1194–1198.
13. Raghunand N, Altbach MI, Bhujwalla ZM, Gillies RJ. Extracellular pH excursions in drug-sensitive and drug-resistant MCF-7 human breast carcinoma cells: a  $^{31}\text{P}$  MRS study. In: Proceedings of the ISMRM 5<sup>th</sup> Annual Meeting, Vancouver, 1997. p 1096.
14. Brown FF, Campbell ID, Kuchel PW, Rabenstein DL. Human erythrocyte metabolism studies by  $^1\text{H}$  spin echo NMR. *FEBS Lett* 1977;82:12–16.
15. Pan JW, Hamm JR, Rothman DL, Shulman RG. Intracellular pH in human skeletal muscle by  $^1\text{H}$  NMR. *Proc Natl Acad Sci USA* 1998;85: 7836–7839.
16. Rabenstein DL, Isab AA. Determination of the intracellular pH of intact erythrocytes by  $^1\text{H}$  NMR spectroscopy. *Anal Biochem* 1992;121:423–432.
17. Gil S, Zaderenzo P, Cruz F, Cerdán S, Ballesteros P. Imidazol-1-ylalkanoic acids as extrinsic  $^1\text{H}$  NMR probes for the determination of intracellular pH, extracellular pH and cell volume. *Bioorg Med Chem* 1994;2:305–314.
18. Gillies RJ, Raghunand N, Bhujwalla ZM, Ballesteros P, Alvarez J, Cerdán S. Measurement of extracellular pH in tumors by  $^1\text{H}$  MRSI. In: Proceedings of the Proc. ISMRM, 5<sup>th</sup> Annual Meeting, Vancouver, 1997. p 1099.
19. van Sluis R, Bhujwalla ZM, Raghunand N, Ballesteros P, Alvarez J, Cerdán S, Gillies RJ. Imaging of extracellular pH using  $^1\text{H}$  MRSI. In: Proceedings of the ISMRM 6<sup>th</sup> Annual Meeting, Sydney, 1998. p 1642.
20. Shungu DC, Glickson JD. Band-selective spin echoes for in vivo localized  $^1\text{H}$  NMR spectroscopy. *Magn Reson Med* 1994;32:277–284.
21. Brown TR. Practical applications of chemical shift imaging. *NMR Biomed* 1992;5:238–243.
22. Wüthrich K, Wagner G. Nuclear magnetic resonance of labile protons in the basic pancreatic trypsin inhibitor. *J Mol Biol* 1979;130:1–18.
23. Madden A, Leach MO, Sharp JC, Collins DJ, Easton D. A quantitative analysis of the accuracy of in vivo pH measurements with  $^{31}\text{P}$  NMR spectroscopy: assessment of pH measurement methodology. *NMR Biomed* 1991;4:1–11.
24. Graham RA, Taylor AH, Brown TR. A method for calculating the distribution of pH in tissues and a new source of pH error from the  $^{31}\text{P}$  NMR spectrum. *Am J Physiol* 1994;266:R638–R645.
25. Wang Z, Bolinger L, Subramanian VH, Leigh JS. Errors of Fourier chemical shift imaging and their corrections. *J Magn Reson* 1991;92: 64–72.
26. Roberts TPL. Physiologic measurements by contrast-enhanced MR imaging: expectations and limitations. *J Magn Reson Imaging* 1997;7: 82–90.
27. Helmlinger G, Yuan F, Delian M, Jain RK. Interstitial pH and  $\text{pO}_2$  gradients in solid tumors in vivo: high-resolution measurements reveal a lack of correlation. *Nature Med* 1997;3:177–182.

# Nm23-Transfected MDA-MB-435 Human Breast Carcinoma Cells Form Tumors With Altered Phospholipid Metabolism and pH: A $^{31}\text{P}$ Nuclear Magnetic Resonance Study In Vivo and In Vitro

Zaver M. Bhujwalla,<sup>1\*</sup> Eric O. Aboagye,<sup>1</sup> Robert J. Gillies,<sup>2</sup> V.P. Chacko,<sup>1</sup> Charmaine E. Mendola,<sup>3</sup> and Joseph M. Backer<sup>3</sup>

**Nm23 genes are involved in the control of the metastatic potential of breast carcinoma cells. To understand the impact of nm23 genes on tumor physiology and metabolism, a  $^{31}\text{P}$  nuclear magnetic resonance (NMR) spectroscopic study was performed on tumors formed in the mammary fat pad of severe combined immunodeficiency mice by MDA-MB-435 human breast carcinoma cells transfected with cDNA encoding wild type nm23-H1 and nm23-H2 proteins. Tumors formed by MDA-MB-435 cells transfected with vector alone were used as controls. All transgene tumors exhibited significantly higher levels of phosphodiester (PDE) compounds relative to phosphomonoester (PME) compounds in vivo compared with control tumors. Similar differences in PDE and PME also were observed for spectra obtained from cells growing in culture. Intracellular pH was significantly lower and extracellular pH was significantly higher for transgene tumors compared with control tumors. Histologic analysis of lung sections confirmed reductions in incidence, number, and size of metastatic nodules for animals bearing transgene tumors. These results suggest that nm23 genes may affect suppression of metastasis through phospholipid-mediated signaling and cellular pH regulation.** *Magn Reson Med* 41:897–903, 1999. © 1999 Wiley-Liss, Inc.

**Key words:** human breast carcinoma metastasis; nonmetastatic 23 transfection; phospholipid metabolism and pH;  $^{31}\text{P}$  nuclear magnetic resonance spectroscopy

The ability of solid tumors to metastasize and establish colonies at distant sites is one of the most life-threatening aspects of cancer. Despite continuing advances in the molecular characterization of events promoting metastasis, little impact has been made on therapy or survival for patients with advanced metastatic tumors (1). This is due partly to the lack of identifiable targets against which to design antineoplastic agents to control the metastatic spread of cancer. Multinuclear magnetic resonance (multi-NMR) methods have a unique role to play in answering this

challenge by providing an understanding of the biochemical and physiologic mechanisms involved in invasion and metastasis. Such an understanding can identify rational targets for therapy.

Recently it was shown that the nm23 (nonmetastatic) gene is related to suppression of metastasis; the metastasis suppression function of the nm23 gene was proposed on the basis of correlation and transfection studies in murine and human systems (2,3). Two highly homologous and evolutionary conserved nm23 genes, nm23-1 and nm23-2, have been identified in rodents (4,5), and two nm23 genes (nm23-H1 and nm23-H2) have been identified in humans (6,7). The two murine nm23 genomic DNAs have been cloned and sequenced (8,9). The human nm23-H1 and nm23-H2 genes have been localized to chromosome 17q21 (10,11). These genes encode 17-kDa proteins identified as nucleoside diphosphate kinase A (NDPK A) and NDPK B, which form homomers and heteromers. In addition, NDPK B displays an increasing list of other activities that apparently are unrelated to its catalytic functions (4). However, the cellular mechanisms by which the nm23 protein suppresses metastatic phenotypic expression is still unknown. In the current study, we have used  $^{31}\text{P}$  NMR spectroscopy to study metabolic and physiologic characteristics of tumors induced in severe combined immunodeficiency (SCID) mice by MDA-MB-435 human breast carcinoma cells transfected with wild type cDNA of nm23-H1 and nm23-H2 and demonstrated that nm23 transfection alters phospholipid metabolism and pH in these breast tumors. Histologic analysis of lung sections from tumor-bearing animals was performed to confirm decreases in metastatic behavior of these breast tumors following transfection with nm23-H1 and nm23-H2. These studies have provided further understanding of the cellular functions of nm23 and of the mechanisms of action of nm23-1 and nm23-2 genes and their role in metastatic dissemination of tumor cells.

## MATERIALS AND METHODS

Coding sequences of normal nm23-H1 and nm23-H2 proteins were cloned into the eucaryotic expression vector pBalPstNeo under control of a constitutive HCMV promoter (11,12). The vector contains an neo resistance gene under control of a simian virus 24 (SV40) promoter. MDA-MB-435 breast carcinoma cells were transfected with nm23 constructs by using a Lipofectin kit (BRL-Life Technologies, Inc., Gaithersburg, MD), and selection of trans-

<sup>1</sup>Oncology Section-Division of Magnetic Resonance Research, Department of Radiology, The Johns Hopkins University School of Medicine, Baltimore, Maryland.

<sup>2</sup>Department of Biochemistry, University of Arizona, Tucson, Arizona.

<sup>3</sup>Department of Microbiology and Immunology, New York Medical College, Valhalla, New York.

Grant sponsor: USAMRMC; Grant numbers: DAMD17-96-1-6131, DAMD17-94-4368, CA58881-03, and DAMD17-96-6078.

Charmaine E. Mendola is currently at the Department of Pharmacology, UMDNJ-R.W. Johnson Medical School, Piscataway, NJ 08854.

\*Correspondence to: Zaver M. Bhujwalla, Department of Radiology, The Johns Hopkins University School of Medicine, Room 208C Traylor Building, 720 Rutland Avenue, Baltimore, MD 21205. E-mail: zaver@mri.jhu.edu

Received 28 September 1998; revised 16 December 1998; accepted 26 December 1998.

© 1999 Wiley-Liss, Inc.

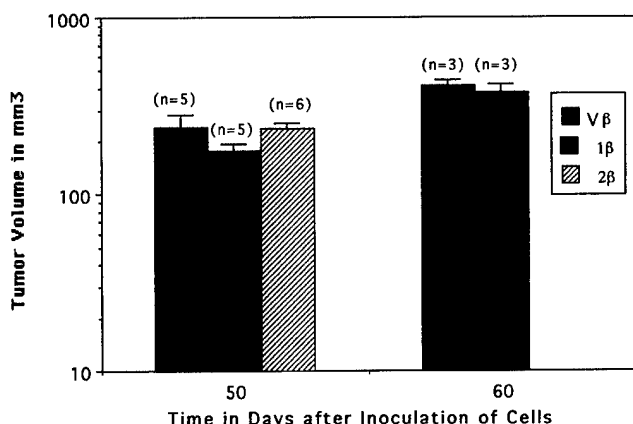


FIG. 1. Tumor volumes following inoculation of identical cell numbers ( $10^6$  cells in 0.05 ml of Hank's balanced salt solution) in the mammary fat pad for the groups of animals used in the study. Bars represent  $\pm 1$  standard error of the mean (S.E.M.).

fected clones was performed in the presence 800  $\mu\text{g}/\text{ml}$  G418. Nm23-transfected pooled clones of MDA-MB-435 were then transfected with p1Zsp- $\beta$ gluc (puro), a mammalian expression vector containing bacterial  $\beta$ -glucuronidase under control of a constitutive HCMV promoter and puromycin-resistance gene under control of an SV40 promoter (gift from Dr. T. Jones, Lederle Laboratories). Selection of clones expressing bacterial  $\beta$ -glucuronidase was performed in the presence of 0.375  $\mu\text{g}/\text{ml}$  puromycin and 800  $\mu\text{g}/\text{ml}$  G418. Pooled clones of double-transfected cells named MDA-MB-435-V $\beta$ , MDA-MB-435-1 $\beta$ , and MDA-MB-435-2 $\beta$  (for vector/ $\beta$ -glucuronidase, nm23-H1/ $\beta$ -glucuronidase, and nm23-H2/ $\beta$ -glucuronidase transfections, respectively) were maintained in the presence of 0.375  $\mu\text{g}/\text{ml}$  puromycin and 200  $\mu\text{g}/\text{ml}$  G418 in Dulbecco's minimum essential medium (Sigma Ltd., St. Louis, MO) containing 10% fetal bovine serum (Sigma Ltd.). Presence of transgenes was confirmed by polymerase chain reaction (PCR) analysis, Western blot analysis, and staining with 5-bromo-4-chloro-3-indol 1 glucuronide (X-glu). Cell doubling times were determined by counting cells plated in 10 mm Petri dishes (three plates per cell line) using a hemacytometer. Cells were counted 48 hr after plating  $5 \times 10^4$  cells per Petri dish. Cell doubling times were approximately 1.5–2.5 days, with no significant differences between the cell lines. Mean values  $\pm 1$  standard error of the mean (S.E.M.) for the three lines were as follows: 2.3 days  $\pm 0.4$  (MDA-MB-435-V $\beta$ ), 1.5 days  $\pm 0.1$  (MDA-MB-435-1 $\beta$ ), and 2.4 days  $\pm 0.6$  (MDA-MB-435-2 $\beta$ ).

MDA-MB-435-V $\beta$ , MDA-MB-435-1 $\beta$ , and MDA-MB-435-2 $\beta$  cells were inoculated in the upper left thoracic mammary fat pad of SCID mice, and  $10^6$  cells were inoculated in 0.05 ml of Hank's balanced salt solution (Sigma Ltd.). The experimental protocol was approved by the Institutional Animal Care and Use Committee. Mice were anesthetized with ketamine (50 mg/kg; Aveco Ltd.) and acepromazine (5 mg/kg; Aveco Ltd.). Tumor volumes, which were measured just prior to performing the  $^{31}\text{P}$  NMR spectroscopic studies, were calculated from caliper measurements of tumor axes (a,b,c) by using the equation for an elliptical volume ( $\pi/6$ )abc. Volumes used in this study were of the order of 300 mm<sup>3</sup>.

$^{31}\text{P}$  NMR spectroscopic studies were performed on a GE CSI 4.7 T instrument (General Electric, Fremont, CA) equipped with shielded gradients. Spectra were obtained with home-built solenoidal coils fitted around the tumor. Because the coil design allowed the probe to be tuned to the proton frequency for shimming, proton images were acquired with the coil to ascertain that only the tumor (and skin) was in the sensitive volume of the coil. Animal body temperature was maintained at 37°C by heat generated

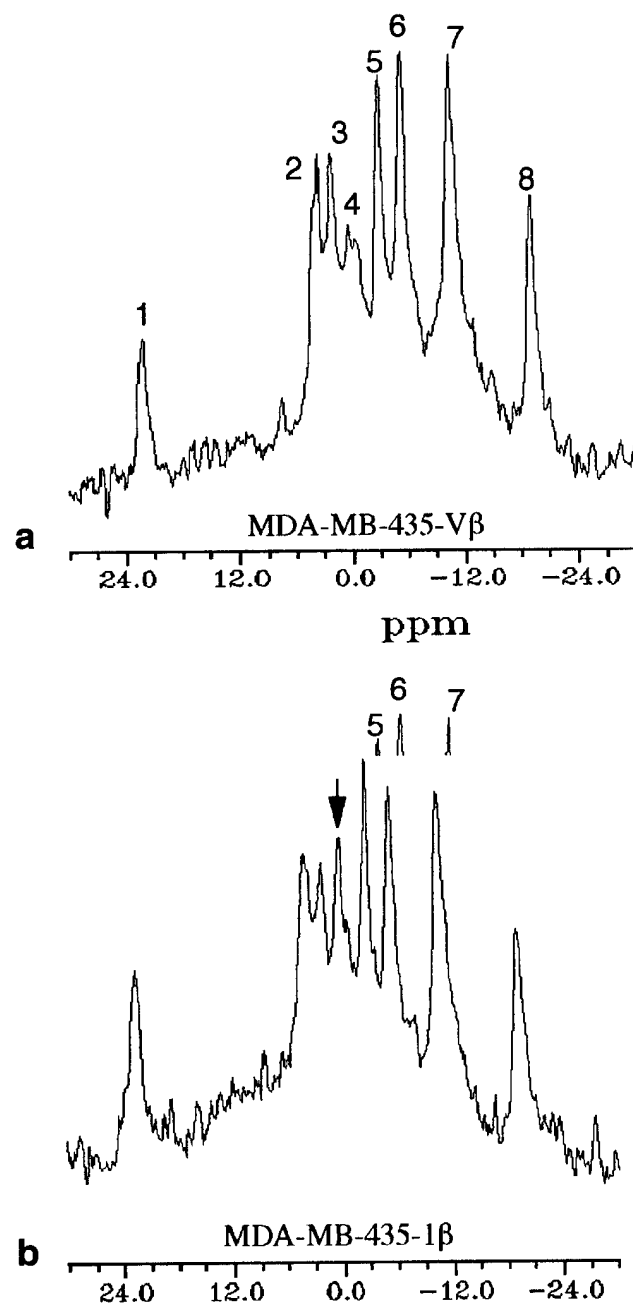


FIG. 2. Representative fully relaxed  $^{31}\text{P}$  nuclear magnetic resonance (NMR) spectra obtained from an MDA-MB-435-V $\beta$  tumor (a) and from an MDA-MB-435-1 $\beta$  tumor (b). Peak assignments are 1) 3-aminopropylphosphonate (3-APP); 2) phosphomonoester (PME); 3) inorganic phosphate (Pi); 4) phosphodiester (PDE); 5) phosphocreatine (PCr); 6)  $\gamma$ -nucleoside triphosphate (NTP); 7)  $\alpha$ -NTP (set to -10 ppm); and 8)  $\beta$ -NTP.

from a pad circulating with warm water. For the  $^{31}\text{P}$  NMR studies, mice were injected intraperitoneally with a solution of the extracellular pH marker 3-aminopropylphosphonate (3-APP; Sigma Ltd.) administered in a volume of 0.2 ml saline (480 mg/kg) following anesthetization. Fully relaxed  $^{31}\text{P}$  NMR spectra were obtained by using a 45° flip angle with 64 scans, a repetition of 5 sec, and a sweep width (SW) of 10000 Hz. Parameters were determined from two spectra obtained per tumor. NMR examinations were completed within 20 min. Extracellular pH ( $\text{pHe}$ ) was obtained from the chemical shift of 3-APP (13), and intracellular pH ( $\text{pHi}$ ) was obtained from the chemical shift of inorganic phosphate ( $\text{Pi}$ ) (14) from the endogenous reference  $\alpha$ -nucleoside triphosphate (NTP) set to -7.57 ppm.  $\text{pHe}$  was calculated from the relationship  $\text{pH} = 6.91 + \log [(\delta_{\text{3-APP}} - 21.11)/(24.30 - \delta_{\text{3-APP}})]$ , and  $\text{pHi}$  was calculated from the relationship  $\text{pH} = 6.66 + \log [(\delta_{\text{Pi}} - 0.65)/(3.11 - \delta_{\text{Pi}})]$ . Data sets were processed by using an exponential line-broadening factor of 22 Hz. Peak areas were determined in the time domain by using an in-house, nonlinear, least-squares, curve-fitting routine for MR data analysis written by Dr. D.C. Shungu.

High-resolution spectra of perchloric acid (PCA) extracts from tumors and cell lines were obtained to resolve the components of the peak in the phosphodiester (PDE) and the phosphomonoester (PME) regions. Mice were anesthetized, and tumors were excised and immediately freeze clamped. Neutralized PCA extracts of tumors were lyophilized and resuspended in  $\text{D}_2\text{O}$ . High-resolution  $^{31}\text{P}$  NMR spectra of tumor extracts were acquired at 11.7 T (MSL-500 spectrometer; Bruker) with a 10-mm high-resolution probe. Spectra were acquired with a 45° flip angle, an SW of 8000 Hz, a repetition time of 5 sec, a block size of 4 K, and 3600 scans.

PCA extracts were obtained from equal numbers of cells for all of the lines used in the study. Cell volumes of the lines were identical. Cells from approximately eight flasks with similar confluence for each cell line were trypsinized, and the action of trypsin was blocked with ice-cold growth medium. Cells were fed approximately 3 hr prior to trypsinization. Cells were washed twice with cold 0.9% NaCl solution and extracted with ice-cold 8% (volume/volume) PCA. The supernatant was neutralized (with 3 M  $\text{K}_2\text{CO}_3$ /1 M KOH), lyophilized, and resuspended in  $\text{D}_2\text{O}$ .

Phosphorus spectra of the extracts were obtained at 11.7 T with a 10-mm high-resolution probe. Spectral acquisition parameters were 45° flip angle, SW = 8000 Hz, 5 sec repetition time, 4 K block size, and scans = 32000–128000.

Lungs from tumor-bearing animals were excised at the end of the NMR experiments and fixed in 10% buffered formalin. Three 5- $\mu\text{m}$ -thick, paraffin-embedded sections were obtained from each pair of lungs and stained with hematoxylin and eosin. Lung sections were examined under an optical microscope and evaluated for incidence, number, and size of metastatic nodules.

Statistical analysis of the data was performed by using StatView II software (version 1.04; Abacus Concepts, Inc., Berkeley, CA). One factorial analysis of variance (ANOVA) was used to evaluate the statistical significance of the in vivo data.

## RESULTS

All of the cell lines were tumorigenic in SCID mice, with a latent period of 5–6 weeks. Growth rates for control and transgene tumors were similar, with a volume-doubling time of 10–14 days. Tumor volumes for groups of animals inoculated at the same time are shown in Figure 1. These data demonstrate the absence of any significant differences in growth rate or “silent interval” following inoculation of the different cell lines in the mammary fat pad.

The most striking difference between  $^{31}\text{P}$  NMR spectra of control (Fig. 2a) and transgene tumors (Fig. 2b) was a marked increase of the peak in the PDE region relative to the PME region in spectra of transgene tumors. The components of the PME region were identified as the membrane precursors phosphocholine (PC) and phosphoethanolamine (PE), and those of the PDE region were identified as the membrane breakdown products glycerophosphocholine (GPC) and glycerophosphoethanolamine (GPE). These components were identified from the high-resolution  $^{31}\text{P}$  NMR spectra of tumor extracts by using the spectral assignments of Evanochko et al. (15). Elevation of the PDE peak relative to the PME peak was observed consistently for all transgene tumors but not for MDA-MB-435-V $\beta$  control tumors. An example of a high-resolution spectrum obtained from PCA extracts of MDA-MB-435-1 $\beta$  tumors

### MDA-MB-435-1 $\beta$ tumor extract

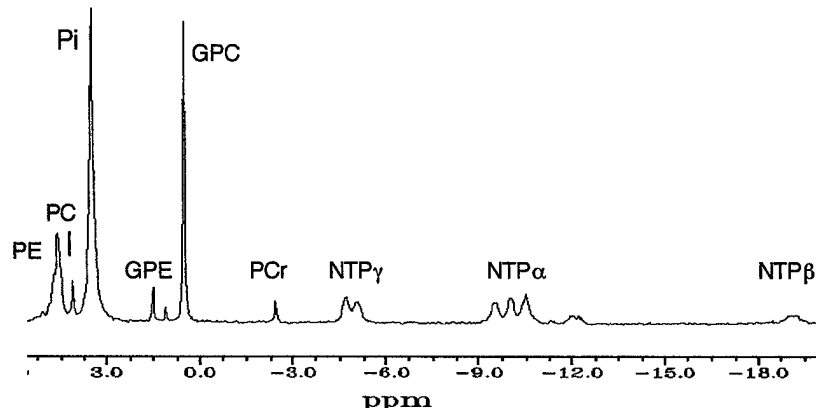


FIG. 3. High-resolution  $^{31}\text{P}$  NMR spectrum from MDA-MB-435-1 $\beta$  tumor extract (obtained from three pooled tumors). Spectral acquisition parameters for in vivo tumors and extract are detailed in Materials and Methods. GPC, glycerophosphocholine; GPE, glycerophosphoethanolamine; PC, phosphocholine; PE, phosphoethanolamine.

Table 1

Nuclear Magnetic Resonance Parameters and Tumor Volumes Obtained From In Vivo Tumors Derived From Control and Transgene MDA-MD-435 Cells

Solid tumor type	Transfection and nm23 levels	Tumor volume (mm <sup>3</sup> )	PDE/PME = [GPE + GPC] / [PE + PC]	pHi	pHe
Control MDA-MB-435-V $\beta$ (n = 7)	Vector/ $\beta$ -glucuronidase transfection (low nm23-H1, H2)	324 ± 42	0.60 ± 0.05	7.37 ± 0.07	6.8 ± 0.11
Transgene MDA-MB-435-1 $\beta$ (n = 6)	nm23-H1/ $\beta$ -glucuronidase transfection (high nm23-H1)	311 ± 45	1.45 ± 0.24*	7.16 ± 0.05*	7.17 ± 0.1*
Transgene MDA-MB-435-2 $\beta$ (n = 6)	nm23-H2/ $\beta$ -glucuronidase transfection (high nm23-H2)	255 ± 19	1.36 ± 0.14*	7.15 ± 0.06*	7.09 ± 0.08*

\*Ninety-five percent confidence limit ( $P < 0.05$ ), analysis of variance, Fisher's protected least significant difference test. Values represent mean ± 1 standard error of the mean; n represents number of animals for each group; PDE, phosphodiester; PME, phosphomonoester; GPE, glycerophosphoethanolamine; GPC, glycerophosphocholine; PE, phosphoethanolamine; PC, phosphocholine; pHi, intracellular pH; pHe, extracellular pH.

with the corresponding peak assignments is shown in Figure 3.

The in vivo results for all of the animals in the study are summarized in Table 1 and show that the PDE/PME ratio was significantly higher for the transgene tumors compared with control tumors. Significant differences in pHi and pHe also were detected for the transgene tumors. pHi was significantly lower, whereas pHe was significantly higher for nm23-H1- and nm23-H2-transfected tumors compared with those derived from cells transfected with vector only (Table 1). No significant differences in NTP/Pi were detected between the cell lines.

$^{31}\text{P}$  NMR high-resolution spectra of isolated cell extracts obtained from cells growing in tissue culture flasks for each of the transfected cell lines and the control cell line are shown in Figure 4. PDE/PME ratios obtained from cell extracts are summarized in Table 2. Observations made in

vivo also were apparent in the spectra of cell extracts, suggesting that differences in PME and PDE peaks for the transgene tumors are due to intrinsic cellular properties arising from transfection of cells with nm23 rather than in vivo physiologic effects related to tumor vascularization or the fraction of necrosis.

For the evaluation of metastasis, we analyzed the lungs of five animals bearing MDA-MB-435-V $\beta$  tumors and six animals with MDA-MB-435-1 $\beta$  tumors. Because the two nm23 genes (nm23-H1 and nm23-H2) are 88% to 90% identical in their amino acid sequences, respectively, we analyzed the lungs of two randomly picked animals with MDA-MB-435-2 $\beta$  tumors that showed no evidence of lung metastasis. Data from microscopic analysis of the lung specimens obtained from tumor bearing mice are presented in Table 3. Lungs obtained from animals bearing transgene tumors showed a reduction in the incidence as well as the number and size of metastatic nodules compared with control tumors (Fig. 5).

## DISCUSSION

The metastatic cascade is a complex phenomenon. To establish metastatic colonies at a site distant from the primary tumor, a cancer cell should pass successfully through the following stages: invasion, intravasation, arrest of cancer cells, extravasation, and, finally, neovascular-

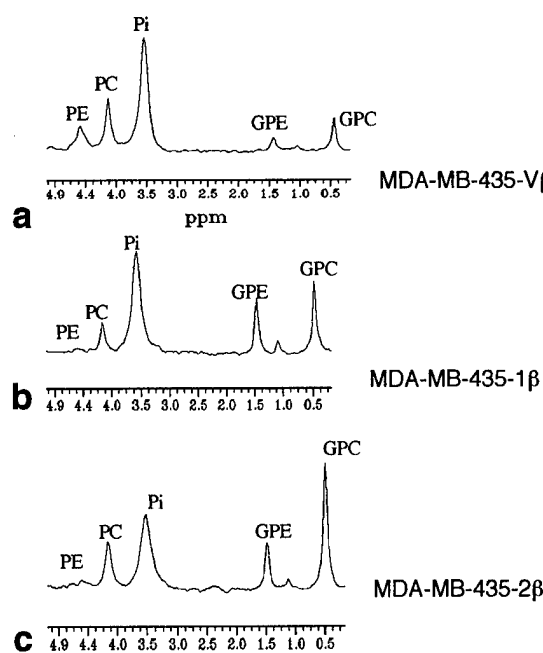


FIG. 4. High-resolution  $^{31}\text{P}$  NMR spectra of cells from MDA-MB-435-V $\beta$  (a), MDA-MB-435-1 $\beta$  (b), and MDA-MB-435-2 $\beta$  (c) cell lines maintained in tissue culture flasks. Spectra are expanded to focus on the phospholipid region. Spectral acquisition parameters are detailed in Materials and Methods.

Table 2  
Phosphodiester/Phosphomonoester Ratios of Control and Transgene Cells

Tumor cell type	Transfection and nm23 levels	(PDE/PME) = [GPE + GPC] / [PE + PC] <sup>a</sup>
Control MDA-MB-435-V $\beta$	Vector/ $\beta$ -glucuronidase transfection (low nm23-H1, 2)	0.53
Transgene MDA-MB-435-1 $\beta$	nm23-H1/ $\beta$ -glucuronidase transfection (high nm23-H1)	1.96
Transgene MDA-MB-435-2 $\beta$	nm23-H2/ $\beta$ -glucuronidase transfection (high nm23-H2)	1.7

<sup>a</sup>Values obtained from eight flasks per cell line. Cells were obtained from a total of eight T-150 flasks for each cell line.

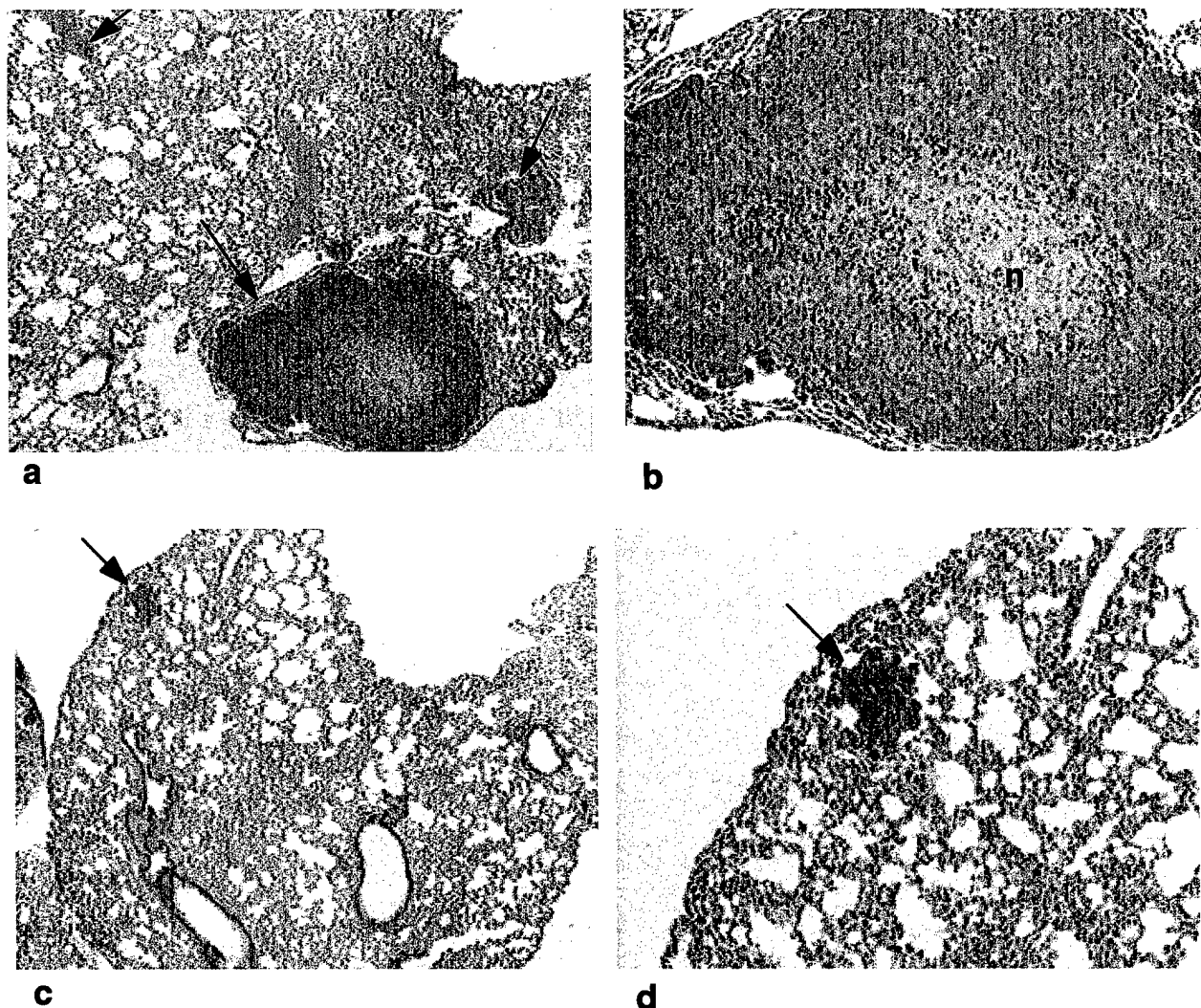


FIG. 5. Photomicrographs demonstrating the marked differences in metastatic nodules in lung sections obtained from mice bearing MDA-MB-435-V $\beta$  and MDA-MB-435-1 $\beta$  tumors. **a,b:** Low- and high-power photomicrographs, respectively, from lung sections obtained from a mouse with an MDA-MB-435-V $\beta$  tumor. **c,d:** Low- and high-power photomicrographs, respectively, from lung sections obtained from a mouse with an MDA-MB-435-1 $\beta$  tumor. Metastatic nodules are marked by arrows, and n denotes a region of necrosis in the metastatic nodule shown in b. No nodules were observed in lung sections that were examined for mice bearing MDA-MB-435-2 $\beta$  tumors.

ization. Attenuation of metastasis may occur at any of these stages. Histologic analyses of lung sections from tumor-bearing animals demonstrated that control tumors and transgene tumors formed by derivatives of MDA-MB-435 human breast carcinoma cells transfected with *nm23* constructs showed different metastatic potential.  $^{31}\text{P}$  NMR spectra of primary tumors in SCID mice revealed significant differences in the phospholipid composition, pH<sub>i</sub>, and pHe of control and transgene tumors. Because transgene tumors were formed by pooled, transfected cells, these alterations were not due to properties of individual clones. These differences in  $^{31}\text{P}$  NMR spectra have provided an insight into how the loss of the *nm23* gene induces metabolic and physiologic alterations that may facilitate metastatic dissemination.

Transgene tumors *in vivo* formed by wild type forms of *nm23-H1* and *nm23-H2* exhibited a significantly higher amount of PDE relative to PME levels compared with control tumors. These differences in phospholipid metabo-

**Table 3**  
Incidence, Number, and Size of Metastatic Nodules Detected in Histologic Sections Obtained from Lungs of Tumor-Bearing Animals

Tumor type	Incidence of metastatic nodules <sup>a</sup>	Number of metastatic nodules averaged for all animals	Range of sizes of metastatic nodules
Control MDA-MB-435-V $\beta$	5/5	20	50–3000 $\mu\text{m}^{\text{b}}$
Transgene MDA-MB-435-1 $\beta$	4/6	2	50–700 $\mu\text{m}^{\text{c}}$
Transgene MDA-MB-435-2 $\beta$	0/2	0	—

<sup>a</sup>Number of animals with lungs containing metastatic nodules/number of animals with lungs examined (three histologic sections were analyzed for each lung specimen).

<sup>b</sup>Mean nodule diameter averaged over all the sections was 800  $\mu\text{m}$ .

<sup>c</sup>Only one nodule was 700  $\mu\text{m}$  in diameter. The remaining nodules were less than 100  $\mu\text{m}$  in diameter.

lism also were detected in cultured cell extracts. The higher PDE levels, including an elevation of GPC, detected for the transgene tumors therefore appeared to be due to cellular characteristics rather than to *in vivo* physiologic characteristics, such as vascularization or necrosis. GPC is formed by degradation of membrane phospholipids by the enzyme phospholipase A<sub>2</sub> (PLA<sub>2</sub>), and this mechanism of PLA<sub>2</sub> on membrane phospholipids provides precursors for eicosanoids when the cleaved fatty acid is arachidonic acid (16). Arachidonic acid-derived eicosanoids include important lipid mediators in signal transduction and tumor promotion, such as prostaglandins, thromboxanes, and leukotrienes (17). These oxygenated fatty acids can have diverse effects on cancer cell motility, invasion, and metastasis (17–20), and the changes in phospholipid metabolism detected following nm23 transfection may reflect the involvement of the nm23 gene product in phospholipid-mediated signaling mechanisms regulating cell motility. This possibility is consistent with the observation by Kantor et al. (21) that murine melanoma and human breast carcinoma cells that are transfected stably with nm23-H1 do not migrate in response to chemoattractants.

The second significant metabolic effect was the difference in both pH<sub>i</sub> and pH<sub>e</sub> between the control and transgene tumors. Transgene tumors formed by MDA-MB-435-1 $\beta$  and MDA-MB-435-2 $\beta$  cells showed significantly lower steady-state pH<sub>i</sub> values compared with control tumors. Studies of cells within a bioreactor system have shown that low pH<sub>i</sub> can result in an increase of GPC and a decrease of PC, which is most likely due to inhibition of GPC/GPE phosphodiesterase activity (22). Inhibition of GPC/GPE phosphodiesterase activity may explain in part the differences in PDE and PME levels for the control and transgene cancer cells (23,24). In the bioreactor system, however, inhibition of GPC/GPE phosphodiesterase activity occurred only for pH<sub>i</sub> lower than 7. Because pH<sub>i</sub> values in all of the tumors in our study were greater than 7, inhibition of GPC/GPE phosphodiesterase activity cannot explain entirely the differences in PDE and PME observed. The lower pH<sub>e</sub> values of the control tumors and the higher pH<sub>e</sub> values of transgene tumors formed by MDA-MB-435-1 $\beta$  and MDA-MB-435-2 $\beta$  cells are particularly interesting, because low pH<sub>e</sub> may enhance the invasive behavior of human breast carcinoma cells. An acidic pericellular pH, for instance, was found to increase the secretion of the active form of the lysosomal protease cathepsin B over time for human breast carcinoma cells (25). Human melanoma cells have been observed to secrete a higher level of 90-kDa gelatinase (a Type IV collagenase) at a pH<sub>e</sub> of 6.8 compared with pH 7.3 (26). This acid-induced secretion of gelatinase was blocked by cycloheximide, indicating that the enzyme induction was due to *de novo* synthesis. Thus, pH-related mechanisms may also play a role in facilitating invasion and metastasis *in vivo* for breast carcinoma cells that lack the nm23 gene.

Although the physiologic and metabolic effects detected in our study may alter invasive and metastatic behavior independently, it is also possible that they may be synergistic or necessary but not sufficient without the other. The results obtained here may open new opportunities for diagnosis/prognosis of metastatic dissemination as well as potential targeting of phospholipid metabolism and pH

regulation for antimetastatic therapeutics. This is the first *in vivo* observation that links activity of a putative metastasis suppressor nm23 gene to metabolic processes. The results also demonstrate the potential of noninvasive NMR to detect forms of gene therapy for suppression of metastasis that may involve transfection of cells with nm23.

## ACKNOWLEDGMENTS

We thank Mr. G. Cromwell for transplanting the tumors and maintaining the cell lines and Ms. Noriko Mori for her assistance with preparing the extracts. This work was supported by USAMRMC grant DAMD17-96-1-6131 (Z.M.B.), DAMD17-94-4368 and CA58881-03 (R.J.G.), and DAMD17-96-6078 (J.M.B.).

## REFERENCES

- Aznavoorian S, Murphy AN, Stetler-Stevenson WG, Liotta LA. Molecular aspects of tumor cell invasion and metastasis. *Cancer* 1993;71:1368–1383.
- Steeg PS, Bevilaqua G, Kopper L, Thorgeirsson UP, Talmadge JE, Liotta LA, Sobel ME. Evidence for a novel gene associated with low tumor metastatic potential. *J Natl Cancer Inst* 1988;80:200–204.
- De La Rosa A, Williams RL, Steeg PS. Nm23/nucleoside diphosphate kinase: toward a structural and biochemical understanding of its biological functions. *Bioessays* 1995;17:53–62.
- MacDonald NJ, De La Rosa A, Steeg PS. The potential role of nm23 in cancer metastasis and cellular differentiation. *Eur J Cancer* 1995;31A:1096–1100.
- Urano T, Takamiya K, Furukawa K, Shiku H. Molecular cloning and functional expression of the second mouse nm23/NDP kinase gene, nm23-M2. *FEBS Lett* 1992;309:358–362.
- Rosengard AM, Krutzsch HC, Shearn A, Biggs JR, Barker E, Margulies IMK, King CR, Liotta LA, Steeg PS. Reduced NM23/Awd protein in tumor metastasis and aberrant *Drosophila* development. *Nature* 1989;342:177–180.
- Stahl JA, Leone A, Rosengard AM, Porter L, King CR, Steeg PS. Identification of a second human nm23 gene, nm23-H2. *Cancer Res* 1991;51:445–449.
- Ishikawa N, Shimada N, Munakata Y, Watanabe K, Kimura N. Isolation and characterization of a gene encoding rat nucleoside diphosphate kinase. *J Biol Chem* 1992;267:14366–14372.
- Shimada N, Ishikawa N, Munakata Y, Toda T, Watanabe K, Kimura N. A second form (b isoform) of nucleoside diphosphate kinase from rat. *J Biol Chem* 1993;268:2583–2589.
- Kelsell D, Black D, Solomon E, Spur NK. Localization of a second nm23 gene, NM22, to chromosome 17q21–22. *Genomics* 1993;17:522–524.
- Backer JM, Mendola CE, Kovacs I, Fairhurst JL, O'Hara B, Shows TB, Mathews S, Murty VVS, Chaganti RSK. Chromosomal localization and nucleoside diphosphate kinase activity of human metastasis-suppressor NM23-1 and NM23-2. *Oncogene* 1993;8:497–502.
- Backer JM, Mendola CE, Price J, Hamby CV. Effects of overexpression of nm23/NDPKs and their catalytically inactive mutants in MDA-MB-435 human breast carcinoma cells. In: Proceedings of the 87th Annual Meeting of American Association for Cancer Research. Washington, DC; 1996. Volume 37, p 78.
- Gillies R, Liu Z, Bhujwalla ZM.  $^{31}\text{P}$  MRS measurements of extracellular pH of tumors using 3-aminopropylphosphonate. *Am J Physiol* 1994;267:C195–C203.
- Moon RB, Richards JH. Determination of intracellular pH by  $^{31}\text{P}$  magnetic resonance. *J Biol Chem* 1973;248:7276–7278.
- Evanochko WT, Sakkai TT, Ng TC, Krishna NR, Kim HD, Zeidler RB, Ghanta VK, Brockman RW, Schiffer LM, Braunschweiger PG, Glickson JD. NMR study of *in vivo* RIF-1 tumors: analysis of perchloric acid extracts and identification of  $^1\text{H}$ ,  $^{31}\text{P}$  and  $^{13}\text{C}$  resonances. *Biochim Biophys Acta* 1984;805:104–116.
- Dennis E. Diversity of group types, regulation and function of phospholipase A<sub>2</sub>. *J Biol Chem* 1994;269:13057.
- Honn KV, Chen YQ. Prostacyclin, hydroxy fatty acids and cancer

metastasis. In: Rubanyi GM, Vane J, editors. Prostacyclin: new perspectives for basic research and novel therapeutic indications. Amsterdam: Elsevier Science; 1992. p 181–200.

- 18. Chen YO, Liu B, Tang DG, Honn KV. Fatty acid modulation of tumor cell-platelet-vessel wall interaction. *Cancer Metast Rev* 1992;11:389–410.
- 19. Fulton AM. The role of eicosanoids in tumor metastasis. *Prostaglandins Leukotrienes Essential Fatty Acids* 1988;34:229–237.
- 20. Karmali RA, Choi K, Otter G, Schmit F. Eicosanoids and metastasis: experimental aspects in Lewis lung carcinoma. *Cancer Biochem Biophys* 1986;9:97–104.
- 21. Kantor JD, McCormick B, Steeg PS, Zetter BR. Inhibition of cell motility after nm23 transfection of human and murine tumor cells. *Cancer Res* 1993;53:1971–1973.
- 22. Galons JP, Job C, Gillies RJ. Increase of GPC levels in cultured mammalian cells during acidosis: a  $^{31}\text{P}$  MR spectroscopic study using a continuous bioreactor system. *Magn Reson Med* 1995;33:422–426.
- 23. Daly PF, Lyon RC, Faustino PJ, Cohen JS. Phospholipid metabolism in cancer cells monitored by  $^{31}\text{P}$  NMR spectroscopy. *J Biol Chem* 1987;262:14875–14878.
- 24. Daly PF, Zugmaier G, Sandler D, Carpen M, Myers CE, Cohen JS. Regulation of the cytidine phospholipid pathways in human cancer cells and effects of 1-beta-D-arabinofuranosylcytosine: a noninvasive  $^{31}\text{P}$  nuclear magnetic resonance study. *Cancer Res* 1990;50:552–557.
- 25. Rozhin J, Sameni M, Ziegler G, Sloane BF. Pericellular pH affects distribution and secretion of cathepsin B in malignant cells. *Cancer Res* 1994;54:6517–6525.
- 26. Kato Y, Nakayama Y, Umeda M, Miyazaka K. Induction of 103 kDa gelatinase/type IV collagenase by acidic culture conditions in mouse metastatic melanoma cell lines. *J Biol Chem* 1992;267:11424–11430.

## Advances in Brief

# Intratumoral Conversion of 5-Fluorocytosine to 5-Fluorouracil by Monoclonal Antibody-Cytosine Deaminase Conjugates: Noninvasive Detection of Prodrug Activation by Magnetic Resonance Spectroscopy and Spectroscopic Imaging<sup>1</sup>

Eric O. Aboagye,<sup>2</sup> Dmitri Artemov, Peter D. Senter, and Zaver M. Bhujwalla

The Johns Hopkins University School of Medicine, Department of Radiology, Oncology Section, Division of MR Research, Baltimore, Maryland 21205 (E. O. A., D. A., Z. M. B.), and Bristol-Myers Squibb Pharmaceutical Research Institute, Seattle, Washington 98121 (P. D. S.)

## Abstract

The monitoring of antibody-directed enzyme-prodrug therapies requires evaluation of drug activation within the tissues of interest. We have demonstrated the feasibility of noninvasive magnetic resonance spectroscopy and spectroscopic imaging (chemical shift imaging) to detect activation of the prodrug 5-fluorocytosine (5-FCyt) to the cytotoxic species 5-fluorouracil (5-FU) by monoclonal antibody-cytosine deaminase (CD) conjugates. *In vitro*, L6-CD but not 1F5-CD selectively metabolized 5-FCyt to 5-FU on H2981 human lung adenocarcinoma cells because of the presence and absence of cell surface L6 and CD20 antigens, respectively. After pretreatment of H2981 tumor-bearing mice with L6-CD, *in vivo* metabolism of 5-FCyt to 5-FU within the tumors was detected by <sup>19</sup>F magnetic resonance spectroscopy; the chemical shift separation between 5-FCyt and 5-FU resonances was ~1.2 ppm. 5-FU levels were 50–100% of 5-FCyt levels in tumors 10–60 min after 5-FCyt administration. Whole body <sup>19</sup>F chemical shift imaging (6 × 6 mm in-plane resolution) of tumor-bearing mice demonstrated the highest signal intensity of 5-FU within the tumor region. This study supports further development of noninvasive magnetic resonance methods for preclinical and clinical monitoring of CD enzyme-prodrug therapies.

## Introduction

Present therapeutic modalities for treating cancer are frequently ineffective because of the lack of specificity of the agents for cancer cells. The ensuing toxicity to normal tissues can severely limit the dose of drug administered. A promising new approach for increasing therapeutic index of anticancer therapy, ADEPT,<sup>3</sup> is based on the delivery to cancer cells of a nontoxic antibody-enzyme conjugate. After a suitable time to allow for clearance of the unbound conjugate, a nontoxic prodrug is administered that is selectively converted to a toxic compound. This paradigm is exemplified by systemic administration of the monoclonal antibody-CD conjugate, L6-CD, which renders tumor cells susceptible to the nontoxic prodrug 5-FCyt (1, 2). The L6-CD contains a yeast enzyme, CD, which converts 5-FCyt to a potent cytotoxic agent, 5-FU. The specificity of this therapeutic approach to cancer cells is based on selective binding of the L6 monoclonal antibody portion of the conjugate to a cell surface antigen strongly expressed on most human carcinomas (3, 4). A similar

approach that involves delivery of a gene that codes for bacterial CD has also been reported by other investigators (5–9).

Unlike traditional chemotherapeutic approaches for cancer that can be monitored by analysis of the drug and metabolite levels in blood, clinical monitoring of enzyme-prodrug therapies requires evaluation of drug activation within the tissue of interest, *e.g.*, tumor. A clinically applicable noninvasive method for monitoring drug activation in target tissue will allow evaluation of drug activation profiles and selectivity for tumors *versus* normal tissues. Such methods may be more acceptable to patients than multiple biopsies, leading to increased compliance to the therapeutic protocols. In this study, we have demonstrated the feasibility of noninvasive MRS and spectroscopic imaging, CSI, for monitoring L6-CD/5-FCyt therapy *in vitro* and in mice bearing human lung cancer (H2981) xenografts. To our knowledge this constitutes the first report of its kind and is also applicable to the alternative approach involving delivery of a “suicide” gene that codes for CD (5–9). MRS of natural abundant fluorine, <sup>19</sup>F MRS, has been used successfully to monitor the pharmacokinetics and metabolism of 5-FU in both experimental animals and patients (10–14). <sup>19</sup>F MRS offers several advantages such as a spin of 1/2, 100% natural abundance, high detection sensitivity (0.83% that of protons), and low background signal. The technique is, therefore, suitable for monitoring *in vivo* levels of fluorinated compounds and their metabolites, particularly when such compounds are administered at high doses (>100 mg/kg body weight) as is the case for 5-FCyt (1, 5). In this study, we have shown that <sup>19</sup>F MRS and CSI can be used to monitor signal intensities of 5-FCyt and 5-FU in tumors as well as their whole body biodistribution in mice. Issues relating to the use of these techniques to evaluate patient tumors are also discussed.

## Materials and Methods

**Materials.** Antibody conjugates L6-CD and 1F5-CD and 13B anti-idiotype antibody were obtained from Bristol-Myers Squibb (Seattle, WA). L6 (IgG2a) binds to a ganglioside antigen expressed on the surface of human carcinomas (4); 1F5 (IgG2a) binds to the CD20 antigen expressed on both normal and neoplastic B cells but not on carcinomas (2, 15); 13B anti-idiotype antibody recognizes and binds to the L6 portion of circulating L6-CD but not of bound L6-CD and enhances the clearance of unbound conjugate (1, 16). The human lung adenocarcinoma cell line H2981 as well as tumor sections derived from this cell line and maintained by *in vivo* passage were also obtained from Bristol-Myers Squibb (3). 5-FU and 5-FCyt were purchased from Sigma Chemical Co. (St. Louis, MO).

**In Vitro Studies.** H2981 cells were cultured in Iscove's modified Dulbecco's medium (Sigma) supplemented with 10% fetal bovine serum, 200 units/ml penicillin, and 0.1 mg/ml streptomycin. To demonstrate the ability of MRS to detect selective drug activation *in vitro*, subconfluent H2981 cells (~2 × 10<sup>7</sup> cells; 4 repeats) were incubated for 30 min with growth medium alone or with medium containing 10 µg/ml L6-CD or 1F5-CD. Cells were then washed three times with PBS and incubated for 1 h with medium containing 5-FCyt. Cells

Received 6/9/98; accepted 7/30/98.

The costs of publication of this article were defrayed in part by the payment of page charges. This article must therefore be hereby marked *advertisement* in accordance with 18 U.S.C. Section 1734 solely to indicate this fact.

<sup>1</sup> Supported in part by USAMRMC Grant DAMD17-96-1-6131.

<sup>2</sup> To whom requests for reprints should be addressed, at Department of Radiology, MR Research, The Johns Hopkins University School of Medicine, 211 Traylor Building, 720 Rutland Avenue, Baltimore, MD 21205.

<sup>3</sup> The abbreviations used are: ADEPT, antibody-directed enzyme prodrug therapy; CD, cytosine deaminase; L6-CD, L6-CD conjugate; 1F5-CD, 1F5-CD conjugate; 5-FCyt, 5-fluorocytosine; 5-FU, 5-fluorouracil; MR, magnetic resonance; MRS, magnetic resonance spectroscopy; CSI, chemical shift imaging; NMR, nuclear magnetic resonance.

Fig. 1. Metabolism of 5-FCyt by H2981 cells pretreated with either L6-CD (*a* and *b*) or 1F5-CD (*c* and *d*). The vertical scale is proportional to the signal intensity, which was normalized to display comparable signal-to-noise levels for cell extracts (*a* and *c*) or media (*b* and *d*). Cells were incubated with conjugate for 30 min followed by three cycles of washing and, finally, were incubated with 5-FCyt for 1 h. Extraction and analysis of samples were performed as reported in "Materials and Methods."

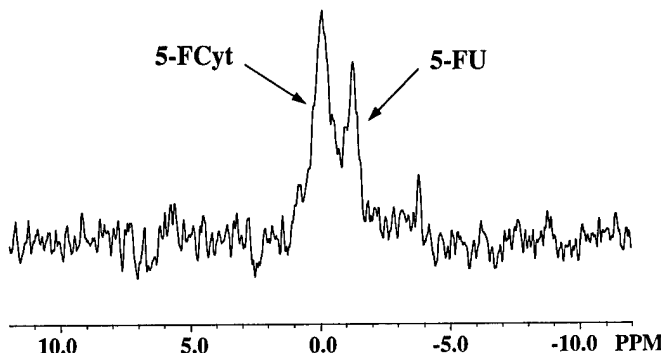
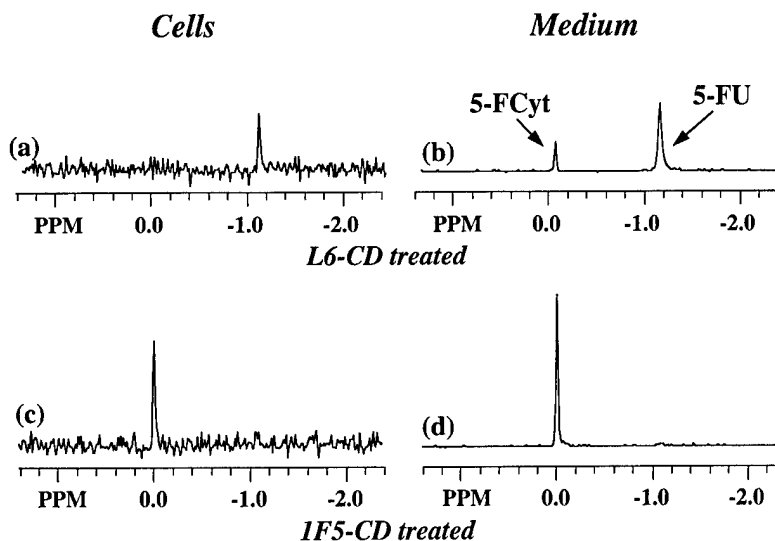


Fig. 2. Typical *in vivo*  $^{19}\text{F}$  spectrum obtained from a H2981 tumor 60 min after 5-FCyt injection (400 mg/kg i.p.). Mice were pretreated with L6-CD and 13B anti-idiotype antibody at 48 and 24 h, respectively, before the MRS study. Data were processed with a line broadening of 25 Hz.

incubated with medium alone were treated with either 5-FCyt or 5-FU. Media containing 5-FCyt and 5-FU were collected after incubation and frozen in liquid nitrogen. Cells were washed three times, trypsinized, and frozen. The cells were homogenized, centrifuged to remove cell debris (15,000 rpm; 4°C; 15 min), and lyophilized. Both incubation media (0.5 ml) and lyophilized cell extracts dissolved in 0.5 ml of distilled water were analyzed for fluorine-related compounds on a Bruker 500-MHz NMR spectrometer. Spectra were acquired using a one-pulse sequence with a flip angle of 45°, 5 s repetition time, 16,384-block size, 22,000-Hz sweep width, and 16/64 scans.

**Tumors.** H2981 tumor sections of approximately 32 mm<sup>3</sup> were implanted s.c. in the right flank of female BALB/cAnNCr-nu nude mice (National Cancer Institute, Frederick, MD). Mice were given laboratory chow and water *ad libitum*. Tumor sizes of 500–600 mm<sup>3</sup> were used for the MR experiments. The experimental protocol was approved by the Institutional Animal Care and Use Committee. Mice were anesthetized by i.p. injection of a mixture of ketamine (25 mg/kg; Aveco Ltd., Fort Dodge, IA), acepromazine (2.5 mg/kg; Aveco), and 0.9% NaCl solution (1:1:2 by volume).

**In Vivo Studies.** *In vivo* experiments were performed to demonstrate: (*a*) activation of 5-FCyt within tumors by MRS; and (*b*) whole body distribution of 5-FCyt and 5-FU by CSI. H2981 tumor-bearing mice were treated i.v. with L6-CD (300 µg/25 g mouse) 48 h before the experiment. To eliminate unbound circulating conjugate, 13B anti-idiotype antibody (200 µg/25 g mouse) was injected i.p. in the same mice 24 h before the experiment. Control animals did not receive antibody treatment. MRS experiments were performed on GE CSI 4.7T and 9.4T NMR spectrometers with a two-turn solenoidal coil tunable to  $^1\text{H}$  or  $^{19}\text{F}$  frequency. Mice were anesthetized and a catheter to deliver 5-FCyt was placed i.p. before commencing the MRS studies. Body temperature was maintained within the magnet by a thermostat-regulated

heating pad. For MRS studies, 5-FCyt was injected as a single bolus dose of 400 mg/kg after acquisition of baseline spectra. To evaluate drug activation in tumors, serial  $^{19}\text{F}$  spectra were acquired every 5 min for 1 h using a one-pulse sequence (60° flip angle, 3-s repetition time, 1,024-block size, 10,000-Hz sweep width and 32/64 scans).

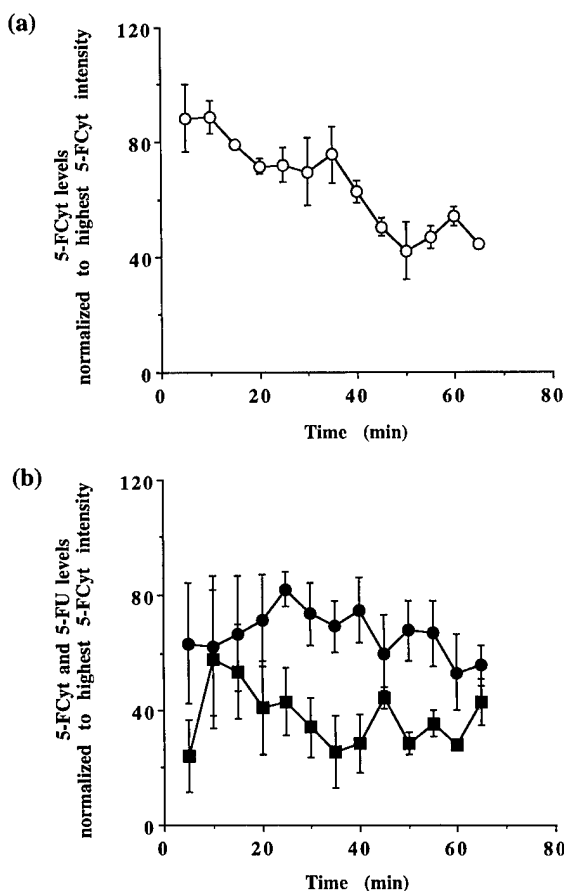


Fig. 3. Profile of 5-FCyt and 5-FU in H2981 tumors following treatment with 400 mg/kg 5-FCyt (i.p.). *a*, control mice not receiving conjugate ( $n = 3$ ), in which the conversion of 5-FCyt ( $\circ$ ) to 5-FU was not detected by MRS. *b*, L6-CD and 13B anti-idiotype antibody-pretreated mice ( $n = 5$ ), in which the conversion of 5-FCyt ( $\bullet$ ) to 5-FU ( $\blacksquare$ ) was detected by MRS. Mice were pretreated with L6-CD and 13B anti-idiotype antibody at 48 and 24 h, respectively, before 5-FCyt injection. Data are means  $\pm$  SE (error bars).

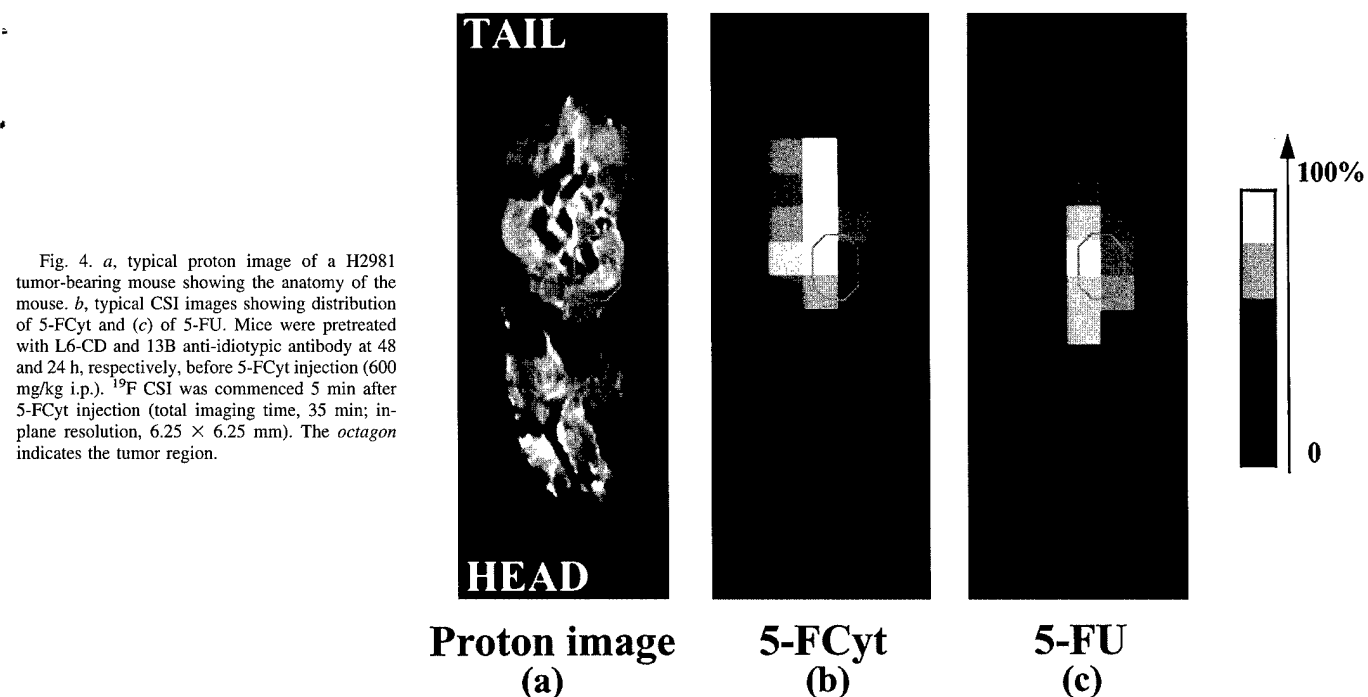


Fig. 4. *a*, typical proton image of a H2981 tumor-bearing mouse showing the anatomy of the mouse. *b*, typical CSI images showing distribution of 5-FCyt and *(c)* of 5-FU. Mice were pretreated with L6-CD and 13B anti-idiotype antibody at 48 and 24 h, respectively, before 5-FCyt injection (600 mg/kg i.p.).  $^{19}\text{F}$  CSI was commenced 5 min after 5-FCyt injection (total imaging time, 35 min; in-plane resolution,  $6.25 \times 6.25$  mm). The octagon indicates the tumor region.

Biodistribution studies were performed on a 4.7T spectrometer with a home-built  $^{19}\text{F}/^1\text{H}$  whole body loop-gap resonator constructed to fit the mice. Mice were treated as above except with 600 mg/kg 5-FCyt. As a prelude to CSI experiments, multislice proton images from 2-mm slices were acquired with a two-dimensional spin echo  $^1\text{H}$  imaging pulse sequence to define mouse anatomy (100-mm field of view, 1-s repetition time, 18-ms echo time, 4 scans, and  $256 \times 128$  matrix size).  $^{19}\text{F}$  CSI experiments were started 5 min after drug injection with a total imaging time of 35 min. A two-dimensional spin echo CSI pulse sequence (17) was used (thick slice, 100-mm field of view, 4 scans,  $16 \times 16$  phase-encoding steps, 2-s repetition time, 9-ms echo time). Intensity distribution of each  $^{19}\text{F}$  peak (5-FCyt or 5-FU) was obtained by image reconstruction using in-house software (dOs) written by Dr. D. C. Shungu.

## Results

Both 5-FCyt and 5-FU resonances, which have a chemical shift difference of 1.2 ppm, were detected by  $^{19}\text{F}$  NMR spectroscopy. Using this technique, the selectivity of L6-CD binding to H2981 cells was demonstrated *in vitro* (Fig. 1*a-d*). After incubation of H2981 cells with L6-CD and three washing cycles, the cells were able to convert 5-FCyt rapidly to 5-FU. Levels of 5-FU in cells and media (mean  $\pm$  SD) after 1 h incubation with 3 mM 5-FCyt were  $0.3 \pm 0.03 \mu\text{mol}/2 \times 10^7$  cells and  $1.62 \pm 0.03$  mM, respectively. 5-FCyt was only observed in the medium at this time point ( $0.4 \pm 0.05$  mM). In contrast, conversion of 5-FCyt to 5-FU did not occur in cells treated with 1F5-CD. Levels of 5-FCyt in cells and media after 1-h incubation with 3 mM 5-FCyt were  $0.42 \pm 0.02 \mu\text{mol}/2 \times 10^7$  cells and  $2.50 \pm 0.08$  mM, respectively. When incubated directly with 5-FCyt, 1F5-CD was equally capable of activating 5-FCyt to 5-FU (data not shown). This means that 1F5-CD did not bind to antigens on H2981 cells and was, therefore, eliminated during the washing cycles. In control experiments in which cells were not incubated with conjugate, the levels of 5-FCyt in cells and medium after incubation with 3 mM 5-FCyt for 1 h were  $0.43 \pm 0.02 \mu\text{mol}/2 \times 10^7$  cells and  $2.95 \pm 0.42$  mM, respectively. Corresponding control experiments with 3 mM 5-FU gave values of  $0.36 \pm 0.02 \mu\text{mol}/2 \times 10^7$  cells and  $1.96 \pm 0.16$  mM for cells and media, respectively. Of interest was the finding that no other signals from 5-FU catabolites or anabolites were observed in these experiments within the experimental time used.

Both 5-FCyt and 5-FU resonances were detected noninvasively in tumors of mice treated with L6-CD/13B/5-FCyt with adequate spectral resolution (Fig. 2). Only the 5-FCyt peak was detected in control mice. For each mouse, resonance intensities of 5-FCyt or 5-FU were normalized to the highest 5-FCyt intensity. The mean intensities are illustrated in Fig. 3, *a* and *b*. In control mice, maximum tumor levels of 5-FCyt occurred early at 10 min after 5-FCyt injection and decreased to 50% of maximum levels at 60 min ( $n = 3$ ). In L6-CD/13B-treated mice, maximum 5-FCyt tumor levels occurred at 25 min and were 60% of maximum levels at 60 min ( $n = 5$ ). Maximum 5-FU tumor levels occurred early at 10 min, and the 5-FU/5-FCyt ratio (an index of CD activity) ranged between 0.5 and 1.0 within the study time (60 min). On the basis of previous studies using the L6-CD/13B/5-FCyt approach (1), these results imply that tumor concentrations of 5-FU will be 0.5–1.0 molar equivalent of intratumoral 5-FCyt when  $\sim 8.7 \mu\text{g}$  of L6-CD (specific activity, 80.6 units/mg) are present in 1 g of a H2981 tumor. Again, no other signals from 5-FU catabolites or anabolites were observed in these experiments.

Initial "phantom" studies demonstrated that it was possible to spatially resolve peaks derived from 5-FCyt and 5-FU resonances by CSI.<sup>4</sup> We used this technique to study the biodistribution of 5-FCyt and 5-FU in L6-CD-treated mice. Fig. 4*a* shows a typical proton image (0.4  $\times$  0.8 mm in-plane resolution) illustrating the anatomy of a mouse. Corresponding CSI data from 5-FCyt and 5-FU resonances in the same mouse are displayed in Fig. 4, *b* and *c*. Signals from 5-FCyt were mainly observed in the abdominal and thoracic regions including tumor (Fig. 4*b*). Importantly, the highest 5-FU intensity was observed within the tumor region (Fig. 4*c*).

## Discussion

5-FU is frequently used in combination therapy for the treatment of adenocarcinomas of the colon, breast, and lung. Both antibody-CD conjugates and genes coding for CD have been previously used to generate 5-FU from 5-FCyt (1, 2, 5–9). These novel approaches are capable of generating high and sustained levels of 5-FU selectively

<sup>4</sup> E. O. Aboagye, D. Artemov, P. D. Senter, and Z. M. Bhujwalla, unpublished data.

within mouse tumors and are, therefore, associated with dramatic cytotoxicity, tumor regression, and even cures (2, 5). A critical issue that may influence the clinical applicability of these approaches is the ability to detect drug activation and target tissue selectivity. To facilitate this, we have applied MR methods to detect selective prodrug activation *in vitro* as well as to define the magnitude and location of CD enzyme activity in mouse tissues after systemic administration of an antibody-enzyme conjugate.

In this study, we showed that MRS and CSI methods are capable of detecting conversion of 5-FCyt to 5-FU *in vitro* and *in vivo*. 5-FCyt and 5-FU resonances were adequately resolved (~1.2 ppm). This implies that one can monitor the levels of these compounds directly without resorting to methods that measure total signal after washout of the original compound. This is particularly important since the metabolism of 5-FCyt by CD was rapid, and both prodrug and metabolite had similar elimination profiles within the time interval studied (1 h). We demonstrated the selectivity of using L6-CD *in vitro*. L6-CD but not 1F5-CD activated 5-FCyt to 5-FU when H2981 human lung adenocarcinoma cells were incubated with 5-FCyt. 1F5-CD binds to CD20 antigen expressed on both normal and neoplastic B cells but not to L6 antigens (2, 15). Thus, after three cycles of washing, no enzyme conjugate was available for metabolic activation of 5-FCyt. In contrast, binding of L6-CD to L6 antigens enabled metabolic activation even after three washing cycles. It is possible that 5-FU is further metabolized in H2981 cells, but despite a reduction in 5-FU levels of >30% after 1-h incubation of cells with 5-FU, no metabolites were detected within 20 ppm up- or down-field of the 5-FU resonance. This may be due to the low levels of these multiple putative 5-FU metabolites.

*In vivo* studies were performed by pretreating tumor-bearing mice with L6-CD followed by 13B anti-idiotypic antibody 24 h after having received L6-CD. 13B binds to and clears circulating L6-CD but not the conjugate that is tumor-associated. This has been shown previously (1) to lead to high tumor:blood conjugate ratios (42:1) and has enabled large doses of 5-FCyt to be subsequently administered. In H2981 tumors pretreated with L6-CD/13B, metabolic activation of 5-FCyt to 5-FU was detected and monitored for 60 min. Metabolic activation was rapid and 5-FU levels were between 50 and 100% of 5-FCyt tumor levels. No activation was observed in control mice. CSI experiments demonstrated that 5-FCyt localized mainly in the abdominal and lower thoracic regions of the mice after i.p. injection. The highest 5-FU levels were observed in the tumor region, supporting the selectivity of this ADEPT approach for tumors. However, other regions showed signal from 5-FU. This may be caused by the diffusion of 5-FU out of the tumor region and/or partial volume averaging, although we cannot completely rule out contribution from nonspecific activation. The absence of the hepatic catabolite of 5-FU, fluoro- $\beta$ -alanine, in *in vivo* spectra suggests that there were low levels of circulating 5-FU in the blood. The absence of anabolites of 5-FU, however, may be caused by the short observation time of 1 h and/or by low levels of such metabolites. The results obtained in these experiments are in general agreement with those obtained by removing the tumors from the animals and analyzing the drug concentrations by high-performance liquid chromatography (1).

These MR methods for detecting conversion of 5-FCyt to 5-FU will aid in the clinical testing of CD-based prodrug therapies. Clinical applicability at the present widely available magnetic field strength of 1.5 tesla may be hampered by low spectral resolution. This problem will be solved by employing high-field magnets such as 3, 4, and 9

tesla presently available in some institutions. MR methods are inherently insensitive. However, at the 5-FCyt dose (400 mg/kg) and the magnetic field strength (4.7 tesla) used, the compounds are easily detected. Lower doses of 5-FCyt (100 mg/kg) can be detected at this field strength, and sensitivity/spatial resolution can be further enhanced by increasing the number of scans or imaging time. In conclusion, we have demonstrated feasibility for using MRS and CSI methods to noninvasively detect the activation of 5-FCyt to 5-FU by ADEPT. These MR methods can be applied to the preclinical and early clinical testing of CD/5-FCyt therapy. In addition MRS and CSI may have applications in a variety of other enzyme-prodrug combinations of clinical interest.

### Acknowledgments

We gratefully acknowledge the assistance of Dr. V. P. Chacko in the MR experiments.

### References

- Wallace, P. M., MacMaster, J. F., Smith, V. F., Kerr, D. E., Senter, P. D., and Cosand, W. L. Intratumoral generation of 5-fluorouracil mediated by an antibody-cytosine deaminase conjugate in combination with 5-fluorocytosine. *Cancer Res.*, 54: 2719–2723, 1994.
- Senter, P. D., Su, P. C. D., Katsuragi, T., Sakai, T., Cosand, W. L., Hellstrom, I., and Hellstrom, K. E. Generation of 5-fluorouracil from 5-fluorocytosine by monoclonal antibody-cytosine deaminase conjugates. *Bioconjugate Chem.*, 2: 477–451, 1991.
- Hellstrom, I., Horn, D., Linsley, P. S., Brown, J. P., Brankovan, V., and Hellstrom, K. E. Monoclonal antibodies raised against human lung carcinoma. *Cancer Res.*, 46: 3917–3923, 1986.
- Marken, J. S., Schieven, G. L., Hellstrom, I., Hellstrom, K. E., Aruffo, A. Cloning and expression of the tumor-associated antigen L6. *Proc. Natl. Acad. Sci. USA*, 89: 3503–3507, 1992.
- Trinh, Q. T., Austin, E. A., Murray, D. M., Knick, V. C., and Huber, B. E. Enzyme/prodrug gene therapy: comparison of cytosine deaminase/5-fluorocytosine versus thymidine kinase/ganciclovir enzyme/prodrug systems in a human colorectal carcinoma cell line. *Cancer Res.*, 55: 4808–4812, 1995.
- Harris, J. D., Gutierrez, A. A., Hurst, H. C., Sikora, K., and Lemoine, N. R. Gene therapy for cancer using tumor-specific prodrug activation. *Gene Ther.*, 1: 170–175, 1994.
- Mullen, C. A., Kilstrop, M., and Blaese, R. M. Transfer of the bacterial gene for cytosine deaminase to mammalian cells confers lethal sensitivity to 5-fluorocytosine: a negative selection system. *Proc. Natl. Acad. Sci. USA*, 89: 3519–3523, 1992.
- Huber, B. E., Austin, E. A., Richards, C. A., Davis, S. T., and Good, S. S. Metabolism of 5-fluorouracil in human colorectal tumor cells transduced with the cytosine deaminase gene: significant antitumor effects when only a small percentage of tumor cells express cytosine deaminase. *Proc. Natl. Acad. Sci. USA*, 91: 8302–8306, 1994.
- Hanna, N. N., Mauceri, H. J., Wayne, J. D., Hallahan, D. E., Kufe, D. W., and Weichselbaum, R. R. Virally directed cytosine deaminase/5-fluorocytosine gene therapy enhances radiation response in human cancer xenografts. *Cancer Res.*, 57: 4205–4209, 1997.
- Findlay, M. P., and Leach, M. O. *In vivo* monitoring of fluoropyrimidine metabolites: magnetic resonance spectroscopy in the evaluation of 5-fluorouracil. *Anticancer Drugs*, 5: 260–280, 1994.
- Kamm, V. J., Rietjens, I. M., Vervoort, J., Heerschap, A., Rosenbusch, G., Hofs, H. P., and Wagener, D. J. Effect of modulators on 5-fluorouracil metabolite patterns in murine colon carcinoma determined by *in vitro*  $^{19}\text{F}$  nuclear magnetic resonance spectroscopy. *Cancer Res.*, 54: 4321–4326, 1994.
- Schlemmer, H. P., Bachert, P., Semmler, W., Hohenberger, P., Schlag, P., Lorenz, W. J., and van Kaick, G. Drug monitoring of 5-fluorouracil: *in vivo*  $^{19}\text{F}$  NMR study during 5-FU chemotherapy in patients with metastases of colorectal adenocarcinoma. *Magn. Reson. Imaging*, 12: 497–511, 1994.
- Presant, C. A., Wolf, W., Waluch, V., Wiseman, C., Kennedy, P., Blayney, D., and Brechner, R. R. Association of intratumoral pharmacokinetics of fluorouracil with clinical response. *Lancet*, 343: 1184–1187, 1994.
- Brix, G., Bellenmann, M. E., Zabel, H. J., Bachert, P., and Lorenz, W. J. Selective  $^{19}\text{F}$  MR imaging of 5-fluorouracil and  $\alpha$ -fluoro- $\beta$ -alanine. *Magn. Reson. Imaging*, 11: 1193–1201, 1993.
- Clark, E. A., Shu, G., and Ledbetter, J. A. Role of the Bp35 cell surface polypeptide in human B cell activation. *Proc. Natl. Acad. Sci. USA*, 82: 1766–1770, 1985.
- Hellstrom, K. E., Yelton, D. E., Fell, H. P., Beaton, D., Gayle, M., MacLean, M., Kahn, M., and Hellstrom, I. Epitope mapping and use of anti-idiotypic antibodies to the L6 monoclonal antibodies raised against human lung carcinoma. *Cancer Res.*, 50: 2449–2454, 1990.
- Brown, T. R., Kincaid, B. M., and Ugurbil, K. NMR chemical shift imaging in three dimensions. *Proc. Natl. Acad. Sci. USA*, 79: 3523–3526, 1982.

DJM/Amy 1-12

PROD. #100301

844  
LMM

## DUPLICATE

*Topics in Magnetic Resonance Imaging*  
00(0): 000-000  
© 1999 Lippincott Williams & Wilkins, Inc., Philadelphia

### Review

## Tumor Angiogenesis, Vascularization, and Contrast-Enhanced Magnetic Resonance Imaging

MD., Ph.D.

Ph.D.

1 (1)

Zaver M. Bhujwalla, Ph.D., Dmitri Artemov, and James Glockner

**Summary:** Angiogenesis, the process by which new blood vessels are generated, occurs during wound healing, in the female reproductive system during ovulation and gestation, and during embryonic development. The process is carefully controlled with positive and negative regulators, because several vital physiological functions require angiogenesis. The consequences of abnormal angiogenesis are either excessive or insufficient blood vessel growth. Ulcers, strokes, and heart attacks can result from the absence of angiogenesis normally required for natural healing, whereas excessive blood vessel proliferation may favor tumor growth and dissemination, blindness, and arthritis. In this review, the process of angiogenesis and the characteristics of the resulting tumor vasculature are outlined. Contrast-enhanced magnetic resonance imaging techniques that currently are available for basic research and clinical applications to study various aspects of tumor angiogenesis and neovascularization are discussed. **Key Words:** Angiogenesis—Vascularization—Cancer—Contrast-enhanced magnetic resonance imaging.

### BRIEF HISTORICAL PERSPECTIVE OF TUMOR VASCULATURE

Of all the complexities and protean facets that cancer displays, the ability of a colony of cancer cells to recruit, form, establish, and maintain a vascular network is one of the most fascinating. Interest in tumor vasculature has existed since the 1920s and earlier. For instance, in 1907, Goldmann (1) noted that the development of a tumor in the liver, stomach, or any other organ resulted in "chaotic irregularity" of the blood vessels and that a growing tumor exhibited an extensive formation of blood vessels that was most apparent in the zone of proliferation that for infiltrating tumors, is at the periphery. He also observed that necrosis occurred in highly vascularized growths, and he

From the Oncology Section, Division of MR Research, Department of Radiology, The Johns Hopkins University School of Medicine, Baltimore, Maryland, U.S.A.

Address correspondence and reprint requests to Dr. Zaver M. Bhujwalla, Oncology Section, Division of MR Research, Department of Radiology, The Johns Hopkins University School of Medicine, Rm 208C Taylor Building, 720 Rutland Avenue, Baltimore, MD 21205, U.S.A.; or zaver@mri.jhu.edu.

made the unique suggestion that areas of necrosis were "the battlefield on which assailant and defendant both perished." Similarly, it was recognized as early at 1945 by Algire et al. (2) that malignant cells provoked a continued vascular proliferation.

Research through the subsequent decades has only served to further reveal the undeniable importance of tumor vasculature not only for tumor growth and hematogenous dissemination, but also for cancer therapy. Observations that had a significant impact on the field of radiation therapy were made by Thomlinson and Gray (3) on human specimens of bronchogenic carcinoma in 1955. In histologic sections of bronchogenic carcinoma, necrosis was found to occur at a distance of 160  $\mu\text{m}$  or greater from the nearest vessel. This distance corresponded closely to the diffusion distance calculated by them, where the concentration of oxygen would approach zero. Their observations provided some of the earliest indirect evidence of the existence of hypoxia and hence radioresistant cells in the tumors (4).

Characteristic "hallmarks" of tumor vasculature have emerged from numerous studies, which now span almost a century (for reviews see references 5–7). Notable among

Casarett

(2)

these characteristics of tumor vasculature are (1) spatial heterogeneity and chaotic structures; (2) arteriovenous shunts; (3) acutely collapsed vessels and transiently collapsing vessels; (4) poorly differentiated, fragile, and leaky vessels lacking in smooth muscle cell lining; and (5) vasculature that frequently is unable to match the rapid growth of cancer cells, resulting in areas of hypoxia and necrosis. In an influential review, Rubin and Casarett (8) pointed out that although the ability of a tumor cell to survive depends on its distance from the capillary from which essential substrates and oxygen diffuse, necrosis is not always due to absence of vascularization or due to the tumor outgrowing its blood supply, a sentiment first expressed by Goldmann (1) in 1907. Acute vascular collapse due to high tumor interstitial pressure (6,9,10), the immune-related destruction of cells, and the release of toxic agents (11) have been cited as some of the other causes.

Vascular properties of tumors have always been considered important because of their role in the delivery of therapeutic agents, and because radioresistant hypoxic cells may be a potential source of treatment failure following radiation therapy. The recent overwhelming interest in tumor vascularization and angiogenesis, however, has arisen due to two findings. One of these is that high vascular density in histologic specimens may be predictive of the disposition of the tumor to metastasize (12-16). Because angiogenesis is critical for tumor growth, antiangiogenic treatment as well as antineovasculature therapies have been proposed and investigated for cancer treatment (17,18). The second finding, related to antiangiogenic therapy, is that repeated treatment cycles with the angiogenesis inhibitor endostatin induced tumor dormancy without inducing tumor drug resistance in at least three experimental tumor models (19).

#### TUMOR ANGIOGENESIS

Although it was recognized from very early on that tumor cells secrete substances to induce vascularization (20), Folkman and his colleagues (21) were the first to isolate a tumor angiogenic factor in 1971. Studies using transgenic mice now suggest a model of tumorigenesis in which mutated oncogenes and tumor repressor genes induce cell proliferation and hyperplasia. There appears to be a secondary set of events after cell proliferation leading from hyperplasia to neoplasia (17,22,23). The induction of angiogenesis is one of the critical events or "switches" in this progression, given that the prevascular phase can persist for years with limited growth of the lesion (23).

Tumor growth to about 1 mm can be accomplished in the absence of neovascularization, because all essential nutrients and waste products can diffuse across this dis-

tance; however, once a tumor has reached this threshold stage of growth, vascularization is essential for additional growth and progression (17,22,23). The normal proliferation rate of endothelial cells is very low compared to many other cell types in the body, and the turnover time of these cells can exceed 1,000 days. In contrast, tumor capillary endothelial cells have a potential doubling time of 2.14 to 13 days (24,25).

Tumor cells, as mentioned earlier, have the ability to induce neovascularization through the release of angiogenesis factors (17,22,23). However, not only cancer cells but also inflammatory cells that infiltrate the tumor and the extracellular matrix can be a source of angiogenesis factors (26). Also as mentioned earlier, there are positive and negative regulators of angiogenesis. Several factors have now been identified as angiogenic promoters and angiogenic inhibitors (26), and several of these promoters and inhibitors are listed in Table 1. The phenomenon of tumor angiogenesis begins with the degradation of the basement membrane of the parent vessel by proteases secreted by activated endothelial cells that migrate and proliferate, leading to the formation of solid endothelial cell sprouts into the stromal space in response to the angiogenic factors. Vascular loops are formed and capillary tubes develop, with formation of tight junctions and deposition of new basement membrane (17,22,23,26).

An angiogenic factor that has attracted significant interest is vascular endothelial growth factor (VEGF). Of all the various angiogenesis promoters and inhibitors, VEGF appears to be the most responsive to the abnormal physiological environments of hypoxia, extracellular acidosis, and substrate deprivation that occur in solid tumors (27). Current information on VEGF has been reviewed extensively by Neufeld et al. (28). VEGF induces angiogenesis

(11)

TABLE 1.

Angiogenesis promoters	Angiogenesis inhibitors
Fibroblast growth factors	Thrombospondin 1
Placental growth factor	Angiostatin
Vascular endothelial growth factor	Endostatin
Transforming growth factor $\alpha$	Prolactin 16-kD fragment
Transforming growth factor $\beta$	Metalloproteinase inhibitors
Angiogenin	Platelet factor 4
Interleukin 8	Genistein
Hepatocyte growth factor	Transforming growth factor $\beta$ (?)
Platelet-derived endothelial cell growth factor	Interferon $\alpha$
Angiopoietin 1	Placental proliférin-related protein
Granulocyte colony-stimulating factor	Fumagillo
Wound fluid	Retinoids
Epidermal growth factor	Protamine
Tumor necrosis factor $\alpha$	
Prostaglandins	

CONTRAST-ENHANCED MRI AND TUMOR ANGIOGENESIS

3

(29,30) and is a potent vascular permeability factor (31). There are five isoforms of VEGF (with 121, 145, 165, 189, and 206 amino acids) generated from alternative splicing of the VEGF gene that are distinguishable by their heparin and heparin-surface binding properties, water solubility, and target receptors (28). The various forms of VEGF bind to two tyrosine-kinase receptors ( $\text{Flt-1}$ ) and ( $\text{KDR/Flk-1}$ ), which are expressed almost exclusively on endothelial cells. In addition, endothelial cells express neuropilin-1 and neuropilin-2 coreceptors, which bind selectively to the 165 amino acid form of VEGF. Of the various isoforms of VEGF, the 121 and 165 forms predominate, although the 189 form also is found in most VEGF-producing cell types (32). Expression of VEGF145 is restricted to cells derived from reproductive organs (28). Hypoxia-mediated transcription of VEGF is thought to occur through the binding of the hypoxia-inducible factor 1 (HIF-1 $\alpha$ ) to an HIF-1 binding site located in the VEGF promoter (33). Hypoxia also promotes the stability of VEGF mRNA through binding proteins (34). There appears to be a dependence of VEGF expression on COX-2 and iNOS that is mediated through prostaglandin E<sub>2</sub> and nitric oxide (35). Under hypoxic conditions, which are typical for most solid tumors, VEGF expression is regulated by pH and glucose concentration (36,37). VEGF expression also can be modulated by oncogenes (28) and by the tumor suppressor gene p53 (39,40) although results to the contrary have been observed (41).

NON MAGNETIC  
SOME ASPECTS OF NONMAGNETIC  
RESONANCE BIOASSAYS FOR MEASURING  
ANGIOGENESIS AND VASCULARIZATION

The most commonly used bioassays for angiogenesis are (1) the developing chick chorioallantoic membrane (CAM), (2) the corneal pocket assay, and (3) the transparent Millipore chamber model grown in the rabbit ear or hamster cheek pouch (20,42,43). The CAM bioassay is carried out in fertilized chick eggs in which a window is prepared by removal of a section of egg shell or in which the shell is totally removed and the egg cultured in a Petri dish. Test substances are placed onto the chick chorionic membrane of 8- to 10-day-old fertilized chick egg on filters or coverslips. Neovascularization is monitored visually, 1-2 days after implantation, and the membranes are fixed and evaluated histologically. In the rabbit corneal assay, test substances are incorporated into sustained release polymer pellets that are implanted into a surgical pocket prepared in the cornea. With a positive response there is directional growth of new capillaries from the limbal blood vessel toward the implant. The bioassay can be quantified by measuring the rate of vessel growth, as well as the length

and the density of the new blood vessels. Angiogenesis in the transparent Millipore chamber is evaluated similarly. These techniques have been used for pioneering studies in angiogenesis, but some of the disadvantages are the limitations on the number of samples that can be assayed and the difficulty in quantifying the results.

The initial angiogenic stimulus results in the formation of tumor neovasculature necessary to establish the solid tumor and deliver substrates and nutrients. Angiogenesis, continues to occur through the life time of the tumor, because new vasculature has to be continually generated with tumor growth. An example of this is shown in Fig. 1. Thus, at any given time in the history of a growing solid tumor, there will be established vasculature and vasculature in the process of being formed. Three quantities, tumor blood flow, tumor vascular volume, and vascular permeability, have mainly been used to characterize tumor vasculature. Several methods are available to measure tumor blood flow quantitatively; however, most of these methods, with the exception of positron emission tomography are either invasive or lack spatial information. The reader is referred to three excellent reviews on measurement and characterization of tumor blood flow (7,27,44).

Some of the earliest measurements of percent vascular volume were obtained by morphometric estimation of vessels in histologic sections (2,45). The functionality of vessels cannot be evaluated in histologic sections, and it may be that a fraction of the vessels may be nonfunctional. This may result in a discrepancy between results obtained using morphometric analysis and results obtained using magnetic resonance imaging (MRI) (discussed later), which measures vasculature into which the contrast agent can be delivered. This issue becomes increasingly important as immunoperoxidase staining of molecules such as CD31 and CD34 (46), which are present on the surface of endothelial cells, are used to identify vessels. It also should be mentioned here that in studies that have shown a dependence of metastasis on microvessel density, the analysis usually is performed by identifying the area of highest neovascularization within the section and obtaining microvessel counts in those areas. In the study by Weidner et al. (12), for patients with invasive breast carcinomas with any metastases, the mean microvessel counts for the areas of highest neovascularization were 101 (at 200 $\times$  field) compared to 45 in carcinoma from patients without metastases. Thus, the number of microvessels in the regions of highest neovascularization determines risk of metastasis. Several macroscopic and microscopic methods of measuring vascular volume have been developed (47), that usually require administration of radioactive tracers and excision of the tumor (48).

Different mathematical formulae have been used to

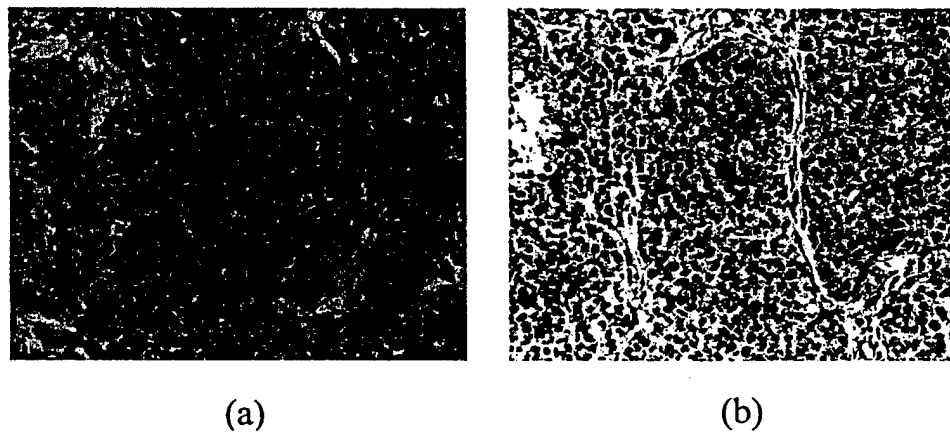


FIG. 1. High-power micrograph (x400) of sprouting endothelial cells in two adjacent 5- $\mu$ m thick sections stained (A) with hematoxylin and eosin and (B) immunostained for VEGF expression. Sections were obtained from a 10-mm-diameter MDA-MB-231 human breast cancer model growing in the flank of a SCID mouse.

compute vessel permeability (5). Usually an effective "permeability-surface area" product (PS), also referred to as "capillary-diffusion capacity," is obtained by determining the rate of extravasation of the test substance into the tumor. PS values quoted in literature depend on the molecular size of the test substance used; the reader is referred to excellent reviews on tumor vascular permeability (5,48).

#### MRI OF ANGIOGENESIS AND VASCULARIZATION

Angiogenesis is a dynamic process. A method to quantitate neovascularization *in situ* without perturbing or excising the tumor would be useful to examine the temporal relationship between neovascularization and tumor growth and determine the effects of antiangiogenic therapy. A noninvasive method of obtaining an index of vascularization or microvessel density also would be advantageous clinically to (1) determine the effects of preoperative hormonal deprivation on vascularization, (2) determine the aggressiveness of the lesion, and (3) play a role in the selection and monitoring of patients treated with antiangiogenic drugs. MRI is suitable for these purposes because MR images can be obtained noninvasively with an inplane resolution on the order of 100  $\mu$ m. Vascularization can be evaluated using intrinsic endogenous contrast (49) or with exogenous paramagnetic contrast agents. Gadolinium chelates are the contrast agents frequently used for MRI. These agents are tightly bound complexes of the rare earth

element gadolinium (Gd) and various chelating agents. The seven unpaired electrons of Gd produce a large magnetic moment that results in paramagnetic properties when the ion is placed in a magnetic field and creates contrast in an MR image. Paramagnetic agents shorten both T1 (spin-lattice relaxation time) and T2 (spin-spin relaxation time), but because tissue T2 values are intrinsically short, the T1 effect of the contrast agent predominates; tissues that take up a paramagnetic agent are brightened (positive enhancement). Susceptibility effects of Gd-based contrast agents resulting in enhancement of T2 and T2\* relaxation have been used to measure vascular volume and flow in clinical studies in brain (50). These studies have been reviewed elsewhere (51) and are not discussed here because their application to tumors is limited due to leaky vasculature and relatively slow perfusion rate in tumors.

The tissue concentration of Gd-based agents can be calculated from changes in T1 obtained from quantitative T1 maps or T1-weighted images. Several Gd complexes are under development or in use. Low-molecular-weight Gd-DTPA compounds (0.57 kD) are used in clinics for contrast enhancement of various lesions including malignant tumors. Macromolecular contrast agents, such as albumin-(Gd-DTPA), remain in the intravascular space with a half-life of several hours because of their large molecular weight (approximately 65 kD). Thus, analysis of relaxivity changes induced by an intravascular agent can be used to determine blood or vascular volume and vascular permeability (52,53). A novel and promising area is the design of receptor-targeted contrast agents where the re-

## CONTRAST-ENHANCED MRI AND TUMOR ANGIOGENESIS

5

sulting contrast is dependent on the density of receptor expression (54). In the following sections we present brief descriptions of current MR methods used to characterize tumor vascularization based on the physical properties of the contrast agent used. Of the three parameters mainly used to characterize tumor vasculature, currently only vascular volume and vascular permeability can be quantified with contrast-enhanced proton imaging. Quantitative blood flow measurements have been obtained using deuterium MRI with D<sub>2</sub>O as the blood flow tracer (55,56). A detailed discussion of this technique is beyond the scope of the present review which is restricted to proton imaging.

### Assessment of angiogenesis with gradient-echo MRI

Detection of tumor vasculature using the intrinsic T<sub>2\*</sub> contrast produced by deoxygenated hemoglobin in tumor capillaries (49) is based on the BOLD technique originally proposed by Ogawa et al. (57) for brain imaging. The functional dependence of T<sub>2\*</sub> is given by Equation 1:

$$1/T_{2^*} \propto (1 - Y)b, \quad (1)$$

where  $Y$  is the fraction of oxygenated blood and  $b$  is the partial vascular or blood volume fraction. In hypoxic tumors where  $0 < Y < 0.2$ , the contrast produced by the method is primarily dependent on  $b$ , which permits rapid *in vivo* determination of vessel densities in tumors. The method works best in poorly oxygenated tumors such as subcutaneous models and human xenografts with random orientation of sprouting capillaries. The technique has been used to detect changes in tumor vascularization following induction of angiogenesis by exogenous angiogenic compounds (49) and to obtain "functional vascular" maps of genetically modified HIF-1 (+/+ and -/-) animal tumor models (58). The method provides fast and truly noninvasive measurement of tumor vascularization because it does not require injection of contrast agent. However, it cannot provide quantitative measurements of tumor vascular volume, and it cannot measure vascular permeability or blood flow.

### MRI detection of tumor angiogenesis by receptor-targeted contrast agents

The feasibility of imaging newly formed vasculature in squamous cell carcinoma in rabbits was demonstrated recently by Sipkins et al. (54) using a paramagnetic contrast agent targeted to the endothelial  $\alpha_v\beta_3$  integrin. The contrast agent was composed of Gd-labeled polymerized liposomes conjugated with biotinylated antibodies targeted against  $\alpha_v\beta_3$  receptors on endothelial cells. A selective enhancement of the tumors was demonstrated without any significant binding of the contrast agent to normal muscle

vasculature adjacent to the tumor. The large particle diameter of 300–350 nm provided a prolonged life time of the contrast agent in plasma lasting approximately 8 h, allowing accumulation of the contrast agent at the  $\alpha_v\beta_3$  receptors. Image intensity proportional to the density of the receptors was obtained from standard T1-weighted images. The method provides information about the density of neovasculature, but dynamic vascular characteristics such as permeability or flow cannot be measured.

### Low-molecular-weight contrast agents

Because low-molecular-weight contrast agents are the only class of paramagnetic agents approved for routine clinical use, there are multiple reports describing applications of these agents to image a variety of tumors including breast tumors (59–61), brain tumors (51), and uterine cervical carcinomas (62). Similarly, several theoretical models have been developed to derive and quantify tumor vascular parameters for these agents.

A frequently used theoretical model of analysis for low-molecular-weight contrast agents is that of Tofts (63), which mainly relies on the existence of vascular and interstitial compartments with uniform tracer concentrations within the compartments. The model also assumes that transport of the agent across the capillary wall is not flow limited. The model ultimately derives influx and outflux transfer constants and extravascular extracellular space. The arterial input function required by the model can be measured separately or defined in real time using voxels localized within large blood vessels. The analytical solution of the model can be derived by approximating the arterial input function to a multiexponential decay as first described by Ohno et al. (64). The concentration of Gd-DTPA is measured from changes in the T1 relaxation rate assuming that water is in fast exchange.

If the flow rate is low and unable to replenish the leak of contrast agent from the vasculature and the extraction fraction of the agent is high, i.e., the fraction of agent leaving the vasculature during a single pass of blood through the tissue is close to 1, which is likely for low-molecular-weight compounds and highly permeable tumors, then only the product of (*blood flow · extraction fraction*) can be defined using the model (65). However, if flow can be measured independently then the extraction fraction (E) and PS can be defined and quantified. Kovar et al. (66) recently used this approach where the freely diffusible tracer D<sub>2</sub>O was used to measure flow independently of Gd-DTPA-dimeglimine, which was used to determine the extraction fraction. The method is somewhat restricted by the low sensitivity of deuterium MRI resulting in low spatial resolution and because D<sub>2</sub>O cannot be used clinically. Combining MRI with an imaging modality

such as positron emission tomography can provide an alternative approach for quantitative measurements of PS in human tumors.

Another approach, developed by Degani et al. (61), uses a three-time-point method to obtain wash-in and wash-out patterns of the contrast agent. The patterns are displayed as an artificial color map with the intensity and hue of the colors proportional to the patterns. The method is based on the two-compartment flow-independent model proposed by the authors previously (60). In the current version the method is model-free and can be used to differentiate between malignant and benign breast lesions, even for situations where the original kinetic model fails to characterize the contrast uptake curves. The method requires obtaining three T1-weighted maps (one precontrast and two postcontrast) that can be acquired with high spatial resolution. However, using the hue and intensity of the color maps to independently quantify vascular permeability, vascular volume or flow rate currently is not feasible.

#### Macromolecular contrast agents

Quantitative determination of parameters of tumor vasculature with low-molecular-weight contrast agent is complicated by fast extravasation of the contrast agent from leaky capillaries in tumors. The availability of high-molecular-weight contrast agents such as albumin-Gd-DTPA complexes or synthetic compounds such as polylysine-Gd-DTPA and gadomer-17 provides a unique opportunity for quantitative determination of tumor vascular volume and vascular PS for molecules of comparable sizes (52,67). The relatively slow leakage of these agents from the vasculature results in a long half-life time and complete equilibration of plasma concentrations within the tumor independently of blood flow, which in this case is large compared with PS. Assuming fast exchange of water between all the compartments in the tumor (plasma, interstitium, and cells), the concentration of the contrast agent within any given voxel is proportional to changes in relaxation rate ( $1/T_1$ ) before and after administration of the contrast. Relaxation rates can be measured either directly using fast single-shot T1 methods (53) or from T1-weighted steady-state experiments (68) that provide better temporal resolution but are susceptible to experimental artifacts caused by variations in  $T_2$  and  $T_{2^*}$  relaxation times. Pixel-by-pixel maps can be reconstructed from the acquired data and processed with an appropriate model to obtain spatial maps of tumor vascular volume and vascular permeability surface area product.

A simple linear compartment model describing uptake of the contrast agent from plasma postulates a negligible reflux of contrast agent from the interstitium back to the blood compartment. Blood concentrations of the contrast

agent can be approximated to be constant for the duration of the MR experiment, and, under these conditions, contrast uptake is a linear function of time (48,69,70). On a plot of contrast agent concentration versus time, the slope of the line provides the parameter PS, and the intercept of the line with the vertical axis at time zero provides vascular volume. For quantitative determination of these parameters, the change in relaxation rate of the blood also should be quantified. Changes in blood  $T_1$  can be obtained separately for blood samples taken before injection of the contrast agent and at the end of the experiment. The method is analogous to the measurement of vascular volume using radiolabeled proteins, usually  $^{125}\text{I}$ -albumin (48, 69,70). However, as pointed out by Tozer and Morris (71), the invasive method requires excision of the tumor, and there may be a possibility of overestimating vascular volume because the protein may already have extravasated within 2 min usually required for equilibration of the protein within plasma.

A more complex two-compartment model, which takes into account reflux of the contrast agent and changing concentrations of the contrast agent in plasma, was developed by Su et al. (72) and Brasch et al. (68). The model used by Su et al. (72) derives three parameters—vascular volume, vascular permeability, and a reflux constant. Brasch et al. (68) use a simple exponential approximation of clearance of the contrast agent from blood, and their model does not require determining the arterial input function. Five parameters (vascular volume, fractional leakage, reflux rates, the initial concentration of contrast agent in plasma, and the fractional turnover rate or clearance of the contrast agent from blood) can be derived from the non-linear fitting of tissue concentrations of the contrast agent obtained experimentally. PS can be obtained from the product of (vascular volume · fractional leakage rate). Blood concentrations of the contrast agent can be defined from large blood vessels within the field of view of the image (68), serial blood samples collected from an arterial line at different time points (72), or from signal enhancement of reference tissue such as liver (73).

For large macromolecular agents such as albumin Gd-DTPA (molecular weight approximately 65 kD), blood concentrations equilibrate within 2–3 min and do not change for at least 60 min after intravenous bolus injection. Tissue concentrations of the agent for a time period starting 5 min after the bolus required for plasma equilibration and up to 40 min after the bolus increase linearly with time. The simple linear model is preferable for analysis of intrinsically noisy relaxation data, because this model is much more stable in comparison with non-linear fitting algorithms required for the two-compartment models discussed earlier. Accuracy of measurement of the

CONTRAST-ENHANCED MRI AND TUMOR ANGIOGENESIS

7

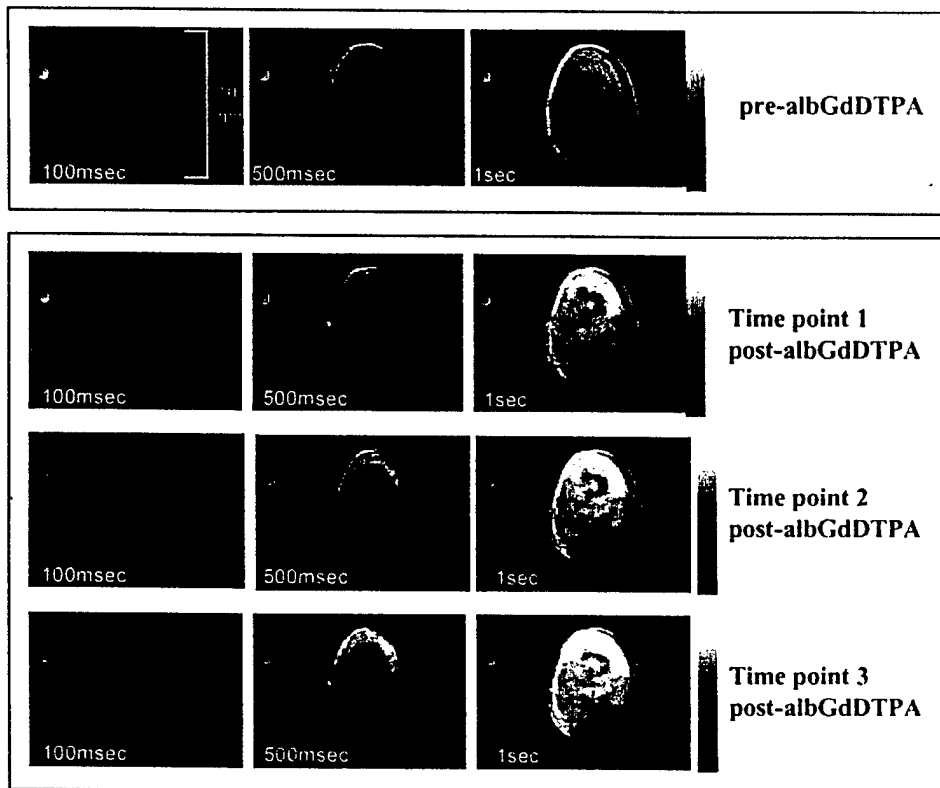


**FIG. 2.** Saturation recovery spin-echo images showing the uptake and distribution of albumin Gd-DTPA in a subcutaneous flank MDA-MB-231 tumor (volume 154 mm<sup>3</sup>) before and at 18, 34, and 50 min after injection (IV) of albumin-Gd-DTPA. A small glass capillary containing water doped with Gd-DTPA can be observed in the images. Images are displayed for three saturation recovery time intervals (100 ms, 500 ms, 1 sec) for a 700-μm sagittal slice through the center of the tumor (field of view = 16 mm; 128 × 128 matrix; number of averages = 2; sweep width = 20,000; in-plane resolution = 125 μm; repetition time = 100 ms; echo time = 16 ms). Images are displayed scaled so that the capillary intensity is constant in all the images to allow easier comparison of the image intensities.

tissue vascular volume does depend, however, on the water exchange rate between the vascular and extracellular compartments. Using a simplified model of fast exchange where there may be intermediate-to-slow exchange can lead to significant underestimation of vascular volume. Experimental approaches to minimize these errors are based on observations that the initial slope of the relaxation curve is independent of the exchange rate (74,75).

Large-molecular-weight contrast agents potentially may be used to measure tumor blood flow by detecting the first pass of the agent through tumor vasculature, similar to the method described previously (50,51), although this approach may not be feasible when the heart beat is very

rapid, as for rodents. Studies exploring the feasibility of such an approach are yet to be performed.

In our laboratory, we used the dynamic distribution of the intravascular paramagnetic contrast agent albumin-Gd-DTPA to quantitate vascular volume and permeability and related the images obtained to the distribution of VEGF and cell morphology in histologic sections obtained from the imaged slice. Vascular volume and permeability were characterized for two different tumor models (MDA-MB-231 human breast cancer line in severe combined immune deficient (SCID) mice and RIF-1 in C3H mice) with the primary aim of determining the ability of the technique to detect differences in these parameters

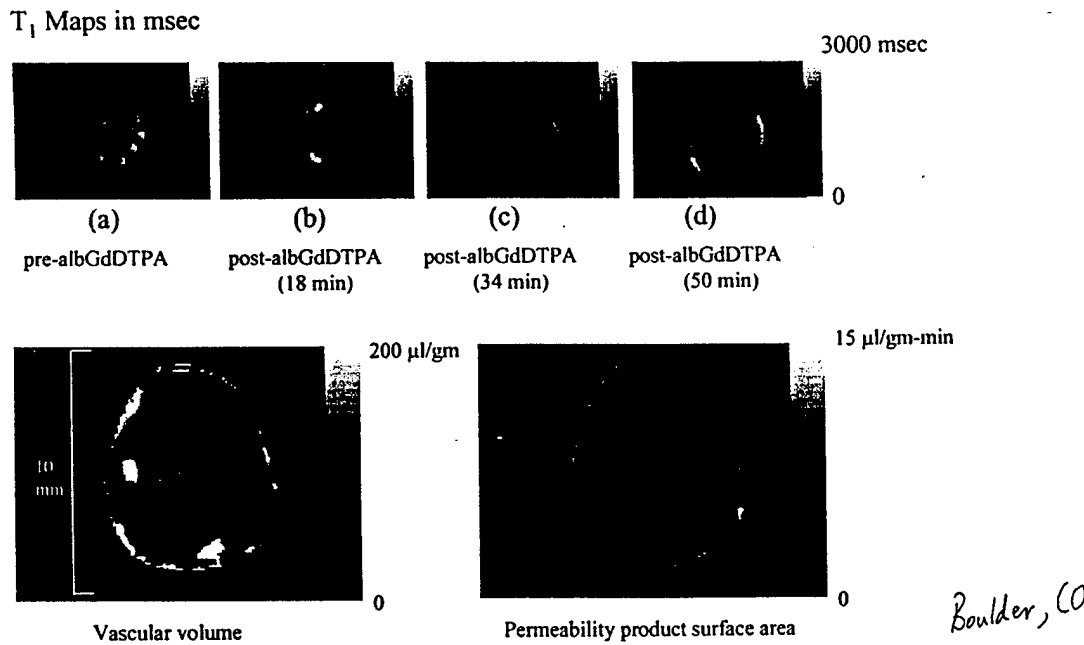


FIG. 3. T<sub>1</sub> maps and maps of vascular volume and permeability generated from the images shown in Fig. 1. Vascular volume and permeability product surface area (PS) maps were generated from the ratio of  $\Delta(1/T_1)$  values in the images to that of blood using an IDL (Interactive Data Language, Research Systems, Inc.) program. The slope of  $\Delta(1/T_1)$  ratios versus time in each pixel was used to compute PS, and the intercept of the line at zero time was used to compute vascular volume. The gray scale is labeled with the minimum and maximum values of vascular volume and permeability.

for these two models. Such a technique then may be applied to determine the correlation between vascular volume and permeability for tumors derived from clones with different metastatic capacity. We detected significant differences in vascular volume generated by the MDA-MB-231 breast cancer line compared to the RIF-1 cell line. We also detected significant differences in vascular permeability for MDA-MB-231 tumors growing in the mammary fat pad compared to MDA-MB-231 tumors growing in the flank. These latter results confirm previous observations made for brain tumor cells (76) that the tumor microenvironment can dictate the permeability of the vasculature.

T<sub>1</sub> maps were obtained for a 700-μm sagittal slice through the center of the tumor using a progressive saturation recovery technique for saturation recovery time intervals of 100 ms, 500 ms, and 1 sec followed by spin-echo imaging for each phase encoding step. A 0.2-ml bolus of a solution of 60 mg/ml albumin-Gd-DTPA made up in saline was injected through the tail vein (dose of 500 mg/kg). T<sub>1</sub> maps were obtained before and for three to

five time points after the intravenous injection. At the end of the imaging studies, the animal was sacrificed, 0.5 ml of blood was withdrawn from the inferior vena cava to measure blood T<sub>1</sub>, and the tumors were excised and fixed in 10% buffered formalin for sectioning and staining. Pre-contrast blood T<sub>1</sub> values were obtained from a separate tumor-bearing group of four SCID and three C3H mice. T<sub>1</sub> values of blood collected in a tube were measured using inversion recovery with 10 recovery time points. Five 5-μm-thick, paraffin-embedded histologic sections were obtained from the imaged slice and immunohistochemically stained for VEGF expression (Santa Cruz Biotechnology, Santa Cruz, CA, U.S.A.) (16). Adjacent sections were stained with hematoxylin and eosin for morphologic information.

A representative dataset demonstrating the raw images, obtained in this case for an MDA-MB-231 flank tumor, is shown in Fig. 2. The corresponding T<sub>1</sub> maps as well as maps of vascular volume and permeability generated from these images are shown in Fig. 3. Both vascular volume and permeability were spatially heterogeneous, and this

CONTRAST-ENHANCED MRI AND TUMOR ANGIOGENESIS

9

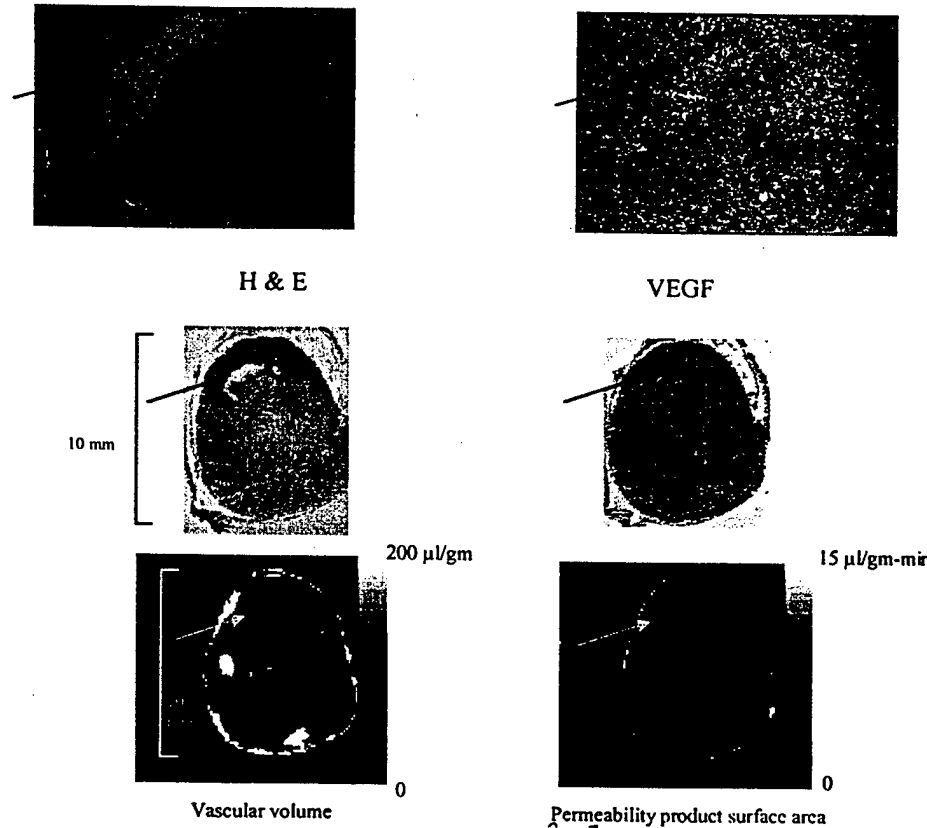


FIG. 4. Adjacent 5- $\mu$ m-thick, histologic sections obtained from the imaged slice in Figs. 1 and 2. The arrow in both sections indicates an area containing necrotic cells. The necrotic area is shown at a higher magnification within the inset of each section. One section is stained with hematoxylin and eosin (section marked H & E in figure); the other section is stained for vascular endothelial growth factor (VEGF) expression using immunoperoxidase staining (section marked VEGF in figure). Regions with an increased brown stain indicate higher levels of VEGF expression. Maps of vascular volume and permeability are included for comparison.

was observed for all the tumors examined. Most tumors showed a higher vascular volume around the periphery, which was consistent with the presence of higher vessel density in the histologic sections and consistent with previous observations that peripheral vascularization is one of two basic patterns of tumor vascularization, the other being central vascularization (8). Regions with the highest vascular volume usually did not exhibit high permeability. Two adjacent tumor sections obtained from the imaged slice (shown in Figs. 1 and 2) and stained with hematoxylin and eosin and immunostained for VEGF expression are displayed in Fig. 4 with the corresponding maps of vascular volume and permeability included for comparison.

(F-4)

Regions of low vascular volume in the MRI maps frequently contained necrotic foci (see magnified inset in Fig. 4) in the histologically stained sections: the regions corresponding to low vascular volume usually were more permeable, as can be observed by comparing the regions marked by an arrow in Fig. 4. A possible explanation, consistent with the necrotic foci observed in these areas, is that areas with low vascular volume may contain the most leaky and nonfunctional vasculature. VEGF staining was most intense around necrotic areas (see arrow in Fig. 4). A coarse spatial agreement was observed between areas with high VEGF expression in the histologic section and areas of high permeability observed in the MR images. Vascular

volumes of MDA-MB-231 mammary fat pad tumors ( $46.6 \pm 9 \mu\text{l/g}$ ,  $n = 6$ ) were significantly higher ( $p < 0.05$ ) than RIF-1 tumors ( $18.7 \pm 4 \mu\text{l/g}$ ,  $n = 4$ ); values represent mean  $\pm$  1 SEM. MDA-MB-231 tumor vasculature was significantly ( $p < 0.016$ ) more permeable in the flank ( $1.64 \pm 0.26 \mu\text{l/g} \cdot \text{min}$ ,  $n = 4$ ) compared to the mammary fat pad ( $0.85 \pm 0.13 \mu\text{l/g} \cdot \text{min}$ ,  $n = 6$ ). Despite the lower vascular volume, the volume doubling time of the RIF-1 tumor model was 3 days compared to 14 days for the MDA-MB-231 model, yet RIF-1 tumors at the volumes studied here do not exhibit necrosis. These data demonstrate the complex balance that exists among vascular volume, tumor growth, and necrosis. Cell cycle time, cell loss factor, the rate of dead cell clearance, the ability of cells to generate an angiogenic response, the endothelial cell proliferation rate, the growth fraction, and the energy and oxygen requirements of cells all play a role in this balance (25,77).

play

### CONCLUSION

The undoubted advantage of contrast-enhanced MRI lies in its ability to obtain vascular parameters noninvasively with in-plane spatial resolutions on the order of 200  $\mu\text{m}$  or less. Thus, it is possible to determine the relationship between vascular volume and vascular permeability within a single pixel and to study the dynamics of this relationship as well as other vascular properties with tumor growth and therapy. Using MRI to study transgenic tumors with specific genetic alterations, in combination with immunostaining of specific molecules not only on endothelial cells but targeted at various stages of the angiogenic pathway, will provide an even greater versatility for understanding tumor angiogenesis and vascularization especially when combined with three-dimensional interactive visualization software (78). With three-dimensional MRI maps, or multislice imaging, it should be possible to measure regions with the highest vascular volume and permeability, as well as the total tumor areas or volumes associated with these high vascular volume and permeability to understand the relationship between vascularization and metastasis. Clinically, some of the major foreseeable applications of contrast-enhanced MRI are to increase the specificity for detecting malignant lesions and for the prognosis of malignant lesions, to detect the efficiency of antiangiogenic treatments as they become clinically available, and equally importantly to use the uptake and distribution of contrast agents to predict the efficiency of delivery of therapeutic agents of similar size to the tumor (79).

**Acknowledgments:** Support from the USAMRMC (DAMD17-96-1-6131), from the Susan G. Komen Breast Can-

cer Foundation, and from the NIH (R01 CA73850) is gratefully acknowledged.

### REFERENCES

1. Goldmann, E. The growth of malignant disease in man and the lower animals, with special reference to the vascular system. *Proc R Soc Med* 1907;1:1-13.
2. Algire GH, Chalkley HW, Legallais FY, Park HD. Vascular reactions of normal and malignant tissues in vivo. I. Vascular reactions of mice to wounds and to normal and neoplastic transplants. *J Natl Cancer Inst* 1945;6:73-85.
3. Thonlinson RH, Gray LH. The histological structure of some human lung cancers and the possible implications for radiotherapy. *Br J Cancer* 1955;9:539-49.
4. Alper T, Howard-Flanders P. Role of oxygen in modifying the radiosensitivity of *E. coli* B. *Nature* 1956;178:978-9.
5. Jain RK. Transport of molecules across tumor vasculature. *Cancer Metastasis Rev* 1987;6:559-93.
6. Jain RK. Transport of molecules in the tumor interstitium: A review. *Cancer Res* 1987;47:3039-51.
7. Jain RK. Determinants of tumor blood flow: A review. *Cancer Res* 1988;48:2641-58.
8. Rubin P, Casaretti G. Microcirculation of tumors, part I: Anatomy, function, and necrosis. *Clin Radiol* 1966;17:220-9.
9. Wiig H, Tveit E, Hultborn R, Reed RK, Weiss L. Interstitial fluid pressure in DMBA-induced rat mammary tumours. *Scand J Clin Invest* 1982;42:59-4.
10. Tozer GM, Lewis S, Michalowski A, Aber V. The relationship between regional variations in blood flow and histology in a transplanted rat fibrosarcoma. *Br J Cancer* 1990;61:250-7.
11. Falk P. Differences in vascular pattern between spontaneous and the transplanted C3H mouse mammary carcinoma. *Eur J Cancer* 1982; 18:155-65.
12. Weidner N, Semple JP, Welch WR, Folkman J. Tumor angiogenesis and metastasis—Correlation in invasive breast carcinoma. *N Engl J Med* 1991;324:1-8.
13. Horak ER, Leek R, Klenk N, et al. Angiogenesis, assessed by platelet/endothelial cell adhesion molecule antibodies, as indicator of node metastases and survival in breast cancer. *Lancet* 1992;340: 1120-4.
14. Hall MC, Zagars GK, Troncoso P, et al. Significance of tumor angiogenesis in clinically localized prostate carcinoma treated with external beam radiotherapy. *Urology* 1994;44:869-75.
15. Siegal JA, Uu E, Brower MK. Topography of neovascularity in human prostate carcinoma. *Cancer* 1995;75:2545-51.
16. Takahashi Y, Kitadai Y, Bucana CD, Cleary KR, Ellis LM. Expression of vascular endothelial growth factor and its receptor, KDR, correlates with vascularity, metastasis, and proliferation of human colon cancer. *Cancer Res* 1995;55:3964-8.
17. Folkman J. Anti-angiogenesis: New concept for therapy of solid tumors. *Ann Surg* 1972;2:409-16.
18. Denekamp J. Review article: Angiogenesis, neovascular proliferation and vascular pathophysiology as targets for cancer therapy. *Br J Radiol* 1993;66:181-96.
19. Boehm T, Folkman J, Browder T, O'Reilly MS. Antiangiogenic therapy of experimental cancer does not induce drug resistance. *Nature* 1997;390:404-7.
20. Greenblatt M, Shubik P. Tumor angiogenesis: Transfilter diffusion studies in the hamster by the transparent chamber technique. *J Natl Cancer Inst* 1968;41:111-24.
21. Folkman J, Merler E, Abernathy C, Williams G. Isolation of a tumor factor responsible for angiogenesis. *J Exp Med* 1971;133:275-88.
22. Folkman J. How is blood vessel growth regulated in normal and neoplastic tissue? *Cancer Res* 1986;46:467-73.
23. Folkman J, Watson K, Ingber D, Hanahan D. Induction of angiogenesis during carcinogenesis. *Science* 1992;255:1154-60.

(5) 175

CONTRAST-ENHANCED MRI AND TUMOR ANGIOGENESIS

11

genesis during the transition from hyperplasia to neoplasia. *Nature* 1989;339:58-61.

24. Tannock IF. Population kinetics of carcinoma cells, capillary endothelial cells, and fibroblasts in a transplanted mouse mammary tumor. *Cancer Res* 1970;30:2470-6.
25. Hirst DG, Denekamp J, Hobson B. Proliferation kinetics of endothelial and tumour cells in three mouse mammary carcinomas. *Cell Tissue Kinetics* 1982;15:251-61.
26. Moses MA. The role of vascularization in tumor metastasis. In: F. William Orr Buchanan, M.R., L. Weisfelds, *Microcirculation in cancer metastasis*. Boca Raton: CRC Press, 1991:257-76.
27. Vaupel P, Kallinowski F, Okunieff P. Blood flow, oxygen and nutrient supply, and metabolic microenvironment of human tumors: A review. *Cancer Res* 1989;49:6449-65.
28. Neufeld G, Cohen T, Gengrinovitch S, Poltorak Z. Vascular endothelial growth factor (VEGF) and its receptors. *FASEB J* 1999;13:9-22.
29. Gospodarowicz D, Abraham JA, Schilling J. Isolation and characterization of a vascular endothelial cell mitogen produced by pituitary-derived folliculo stellate cells. *Proc Natl Acad Sci USA* 1989;86:7311-5.
30. Ferrara N, Henzel WJ. Pituitary follicular cells secrete a novel heparin-binding growth factor specific for vascular endothelial cells. *Biochem Biophys Res Commun* 1989;161:851-8.
31. Senger DR, Galli SJ, Dvorak AM, Perruzzi CA, Harvey VS, Dvorak HF. Tumor cells secrete a vascular permeability factor that promotes accumulation of ascites fluid. *Science* 1983;219:983-5.
32. Bacic M, Edwards NA, Merrill MJ. Differential expression of vascular endothelial growth factor (vascular permeability factor) forms in rat tissues—Short communication. *Growth Factors* 1995;12:11-5.
33. Levy AP, Levy NS, Wegner S, Goldberg MA. Transcriptional regulation of the rat endothelial growth factor gene by hypoxia. *J Biol Chem* 1995;270:13333-40.
34. Claffey KP, Shih SC, Mullen A, et al. Identification of a human VPF/VEGF 3' untranslated region mediating hypoxia-induced mRNA stability. *Mol Biol Cell* 1998;9:469-81.
35. Chiarugi V, Magnelli L, Gallo O, Cox-2, iNOS and p53 as players of tumor angiogenesis (Review). *Int J Mol Med* 1998;2:715-9.
36. Brooks SE, Gu X, Kaufmann PM, Marcus DM, Caldwell RB. Modulation of VEGF production by pH and glucose in retinal Muller cells. *Curr Eye Res* 1998;17:875-82.
37. Shweiki D, Neeman M, Itin A, Keshet E. Induction of vascular endothelial growth factor expression by hypoxia and by glucose deficiency in multicell spheroids: Implication for tumor angiogenesis. *Proc Natl Acad Sci USA* 1995;92:768-72.
38. Feldkamp MM, Lau N, Rak J, Kerbel RS, Guha A. Normoxic and hypoxic regulation of vascular endothelial growth factor (VEGF) by astrocytoma cells is mediated by Ras. *Int J Cancer* 1999;81:118-24.
39. Mukhopadhyay D, Tsikots I, Sukhatme VP. Wild-type p53 and v-src exert opposing influences on human vascular endothelial growth factor gene expression. *Cancer Res* 1995;55:6161-5.
40. Bouvet M, Ellis LM, Nishizaki M, et al. Adenovirus-mediated wild type p53 gene transfer down-regulates vascular endothelial growth factor expression and inhibits angiogenesis in human colon cancer. *Cancer Res* 1998;58:2288-92.
41. Agani F, Kirsch DG, Friedman SL, Kastan MB, Semenza GL. p53 does not repress hypoxia-induced transcription of the vascular endothelial growth factor gene. *Cancer Res* 1997;57:4474-7.
42. Ausprunk DH, Knighton DR, Folkman J. Vascularization of normal and neoplastic tissues grafted to the chick chorioallantois: Role of host and preexisting graft blood vessels. *Am J Pathol* 1975;79:597-628.
43. Gimbrone MA, Cotran RS, Leapman SB, Folkman J. Tumor growth and neovascularization: An experimental model using the rabbit cornea. *J Natl Cancer Inst* 1974;52:413-27.
44. Jain RK, Ward-Hartley KA. Tumor blood flow: Characterization, modification and role in hyperthermia. *IEEE Trans* 1984;SU-31:504-26.
45. Chalkley HW. Method for the quantitative morphologic analysis of tissues. *JNCI* 1943;4:47-53.
46. Kacemi A, Vervelle C, Uzan S, Challier JC. Immunostaining of vascular, perivascular cells and stromal components in human placental villi. *Cell Mol Biol* 1999;45:101-13.
47. Song CW, Levitt SH. Quantitative study of vascularity in Walker carcinoma 256. *Cancer Res* 1971;31:587-89.
48. Peterson H-I. Vascular and extravascular spaces in tumors: Tumor vascular permeability. In: Peterson H-I, ed. *Tumor blood circulation: Angiogenesis, vascular morphology and blood flow of experimental and human tumors*. Boca Raton: CRC Press, 1979:77-85.
49. Abramovitch R, Frenkel D, Neeman M. Analysis of subcutaneous angiogenesis by gradient echo magnetic resonance imaging. *Magn Reson Med* 1998;39:813-24.
50. Ostergaard L, Weisskoff RM, Chesler D, Gyldensted C, Rosen BR. High resolution measurement of cerebral blood flow using intravascular tracer bolus passages. Part I: Mathematical approach and statistical analysis. *Magn Reson Med* 1996;36:715-25.
51. Sorensen AG, Tieovsky AL, Ostergaard L, Weisskoff RM, Rosen BR. Contrast agents in functional MR imaging. *J Magn Reson Imaging* 1997;7:47-5.
52. Schmidli U, Ogan M, Paajanen H, et al. Albumin labeled with Gd-DTPA as an intravascular, blood pool-enhancing agent for MR imaging: biodistribution and imaging studies. *Radiology* 1987;162:205-10.
53. Schwarzbauer C, Syha J, Haase A. Quantification of regional blood volume by rapid T1 mapping. *Magn Reson Med* 1993;29:709-12.
54. Sipkins DA, Cheresh DA, Kazemi MR, Nevin LM, Benderski MD, Li KCP. Detection of tumor angiogenesis in vivo by avb3-targeted magnetic resonance imaging. *Nature Med* 1998;4:623-6.
55. Larcombe McDowell JB, E. JL. Deuterium nuclear magnetic resonance imaging of tracer distribution in  $D_2O$  clearance measurements of tumor blood flow in mice. *Cancer Res* 1990;50:363-9.
56. Evelhoch JL. Measurement of tumor blood flow by deuterium NMR and the effects of modifiers. *NMR Biomed* 1992;5:290-5.
57. Ogawa S, Lee T-M, Nayak AS, Glynn P. Oxygenation-sensitive contrast in magnetic resonance image of rodent brain at high magnetic fields. *Magn Reson Med* 1990;14:68-78.
58. Carmeliet P, Dor Y, Herbert J-M, et al. Role of HIF-1 $\alpha$  in hypoxia-mediated apoptosis, cell proliferation and tumor angiogenesis. *Nature* 1998;394:485-90.
59. Sinha S, Lucas-Quesada FA, DeBruhl ND, et al. Multifeature analysis of Gd-enhanced MR images of breast lesions. *J Magn Reson Imaging* 1997;7:1016-26.
60. Furman-Haran E, Margalit R, Grobgeld D, Degani H. Dynamic contrast-enhanced magnetic resonance imaging reveals stress-induced angiogenesis in MCF7 human breast tumors. *Proc Natl Acad Sci USA* 1996;93:6247-51.
61. Degani H, Gusin V, Weinstein D, Fields S, Strano S. Mapping pathophysiological features of breast tumors by MRI at high spatial resolution. *Nature Med* 1997;3:780-2.
62. Hawighorst H, Knapstein PG, Weikel W, et al. Angiogenesis of uterine cervical carcinoma: characterization by pharmacokinetic magnetic resonance parameters and histological microvessel density with correlation to lymphatic involvement. *Cancer Res* 1997;57:4777-86.
63. Tofts PS. Modeling tracer kinetics in dynamic Gd-DTPA MR imaging. *J Magn Reson Imaging* 1997;7:91-101.
64. Ohno K, Pettigrew KD, Rapoport SI. Local cerebral blood flow in the conscious rat as measured with 14C-antipyrine, 14C-iodoantipyrine and 3H-nicotine. *Stroke* 1979;10:62-7.
65. Larsson HBW, Stuegaard M, Frederiksen JL, Jensen M, Henriksen O, Paulson OB. Quantitation of blood-brain barrier defect by magnetic resonance imaging and gadolinium-DTPA in patients with multiple sclerosis and brain tumors. *Magn Reson Med* 1990;16:117-31.
66. Kovar DA, Lewis MZ, River JN, Lipton MJ, Karczmar GS. In vivo

(2) OK

Evelhoch  
(3) JL

imaging of extraction fraction of low molecular weight MR contrast agents and perfusion rate in rodent tumors. *Magn Reson Med* 1997; 38:259-68.

67. Ogan MD, Schmiedl U, Mosley ME, Grodd W, Paajanen H, Brasch RC. Albumin labeled with Gd-DTPA; an intravascular contrast enhancing agent for magnetic resonance blood pool imaging: preparation and characterization. *Invest Radiol* 1987;22:665-71.

68. Brasch R, Pham C, Shames D, et al. Assessing tumor angiogenesis using macromolecular MR imaging contrast media. *J Magn Reson Imaging* 1997;7:68-74.

69. Braunschweiger P, Schiffer LM. Effect of dexamethasone on vascular function in RIF-1 tumors. *Cancer Res* 1986;46:3299-303.

70. Braunschweiger P. Effect of cyclophosphamide on the pathophysiology of RIF-1 solid tumors. *Cancer Res* 1988;48:4206-10.

71. Tozer GM, Morris CC. Blood flow and blood volume in a transplanted rat fibrosarcoma: Comparison with various normal tissues. *Radiother Oncol* 1990;17:153-66.

72. Su M-Y, Muhler A, Lao X, Nalcioglu O. Tumor characterization with dynamic contrast-enhanced MRI using contrast agents of various molecular weights. *Magn Reson Med* 1998;39:259-69.

73. Su M-Y, Wang Z, Roth GM, Lao X, Samoszuk MK, Nalcioglu O. Pharmacokinetic changes induced by vasomodulators in kidneys, livers, muscles, and implanted tumors in rats as measured by dynamic Gd-DTPA-enhanced MRI. *Magn Reson Med* 1996;36:868-77.

74. Schwickert HC, Roberts TPL, Shames DM, et al. Quantification of liver blood volume: Comparison of ultra short T1 inversion recovery echo planar imaging (ULSTIR-EPI), with dynamic 3D-gradient recalled echo imaging. *Magn Reson Med* 1995;34:845-52.

75. Donahue KM, Weisskoff RM, Chesler DA, et al. Improving MR quantitation of regional blood volume with intravascular T1 contrast agents: Accuracy, precision, and water exchange. *Magn Reson Med* 1996;36:858-67.

76. Yuan F, Salehi AA, Boucher Y, Vasthare US, Tuma RF, Jain RK. Vascular permeability and microcirculation of gliomas and mammary carcinomas transplanted in rat and mouse cranial windows. *Cancer Res* 1994;54:4564-8.

77. Steel GG. *Growth kinetics of tumours: Cell population kinetics in relation to the growth and treatment of cancer*. Oxford: Clarendon Press, 1977.

78. Bhujwalla ZM, Artemov D, Solaiyappan M, Mao D, Backer JP. Comparison of vascular volume and permeability for tumor derived from metastatic human breast cancer cells with and without the metastasis suppressor gene nm23. In: *Proceedings of 7th Scientific Meeting of the ISMRM*, Philadelphia, 1999.

79. Artemov D, Bhujwalla ZM. Drug delivery to tumors: Potential of MR for measurement and prediction. In *Proceedings of 7th Scientific Meeting of the ISMRM*. Philadelphia, 1999.

breast

NUMBER \_\_\_\_ OF \_\_\_\_

## AUTHOR QUERIES

DATE 6/28/99

JOB NAME TMRI

JOB NUMBER 10206

ARTICLE 3 (100301)

QUERIES FOR AUTHOR Bhujwalla et al.

THIS QUERY FORM MUST BE RETURNED WITH ALL PROOFS FOR CORRECTIONS

- 1) AU: Highest academic degree of last two authors? Dmitri Artemov, Ph.D., and James Glockner, M.D., Ph.D.
- 2) AU: Verify spelling vs Casarett in reference 8. Casarett
- 3) AU: Changed spelling to match references 21-23 OK? OK
- 4) AU: Expansion of PGE2 and NO correct? OK
- 5) AU: Volume? Volume No. 175
- 6) AU: Please clarify initials and surnames. In: F. William Orr, M.R. Buchanan, L. Weiss
- 7) AU: Please expand. OK
- 8) AU: Provide/clarify names and initials. Evelhoch JL
- 9) AU: Location? Boulder, CO

# 3-Dimensional Interactive Registration of MRI Images and Histological Data

Dmitri Artemov, Meiyappan Solaiyappan and Zaver M. Bhujwalla

Oncology Section-Division of MR Research, Dept. of Radiology, The Johns Hopkins University School of Medicine, Baltimore, MD 21205, USA.

**INTRODUCTION:** Magnetic Resonance Imaging and spectroscopy techniques are continually evolving to address critical issues in tumor physiology such as parameters of tumor vascularization. Consequently there is a necessity to develop visualization software able to analyze the MR information and relate it to data obtained from the same tumor with other technologies such as immunostaining, autoradiography and/or PET. Such a multi-modal approach will allow a high level of versatility in probing the disease and may result in revealing of new information hidden in the original data. Here we present results obtained with our novel visualization software which we are developing for these purposes.

**METHODS:** 3D maps of blood volume and vascular permeability obtained from a tumor as described in (1) were compared with three dimensional histological maps reconstructed from tissue slices stained with hematoxylin eosin (H&E) and for VEGF expression. Briefly, multislice T<sub>1</sub> images were obtained from prostate cancer MLL xenografts in SCID mouse with Turbo-FLASH saturation recovery technique (64x64 resolution, 8 slices, 100ms, 500ms, and 1s recovery delays) with an experimental time of 7 min per multislice map. An M<sub>0</sub> image used for pixel by pixel reconstruction of T<sub>1</sub> maps was acquired once at the beginning of the experiment with a recovery delay of 7s. Images were obtained before and for 32 min after i.v. administration of 0.2ml of 60 mg/ml albumin-GdDTPA in saline (dose of 500mg/kg), starting 10 min after the injection. At the end of the imaging studies, the animal was sacrificed, 0.5 ml of blood was withdrawn from the inferior vena cava, and tumors marked for referencing to the MRI images were excised, and fixed in 10% formalin for sectioning and staining. Permeability product surface area (PS) and vascular volume [VV] maps were generated on a pixel by pixel basis from the slope and intersect at zero time of the linear plots of ratios of  $\Delta(1/T_1)$  values in the images to that of blood vs. time (1). Ten pairs of adjacent 5 $\mu$ m histological sections obtained at 500  $\mu$ m intervals through the tumor were stained with H&E and immunostained for VEGF expression (2). Sections were digitized with a Sanyo CCD camera attached to an optical microscope. 3-D reconstruction and coregistration of MRI and histological sections was performed using the Clinical Microscope Visualization software that we are developing as a research tool for our investigation. The software consists of two sets of routines. The first module builds volume images from 2-D multislice histology images and optionally provides stitching of high resolution image 'tiles' acquired from the histological sections with the microscope at high magnification. The tiles stitched along the overlapping borders produce a large 'virtual' field of view that represents the full cross section which could not be acquired otherwise in a single actual field of view at the selected high resolution. This virtual image can be panned around, zoomed in, to look at selected regions at the full resolution in which they were acquired. The second module of the software performs visualization of the volumetric model in suitable 3-D perspective. The volume images can be interactively rendered using the volumetric visualization software. The transfer functions that control the voxel transparency and intensity characteristics of various structures of interest can be interactively adjusted to delineate them from the surrounding structures. Interactive registration of the MR data with histology data is done by rendering the two volume data sets together using individual transfer function to control the overlapping of the voxels from each volume so that the two volumes can be visualized together. Each volume can be independently manipulated in the 3D space to achieve better registration. The software system is developed around Silicon Graphics Inc., Workstation systems, taking full advantage of the hardware accelerated graphics capabilities such as 2- and 3-D Textures to provide interactive rendering results.

**RESULTS:** Figures 1 and 2 demonstrate 3-dimensional coregistration of 3D images of blood volume and vascular permeability with 3D histological maps stained with H&E and for VEGF expression respectively.

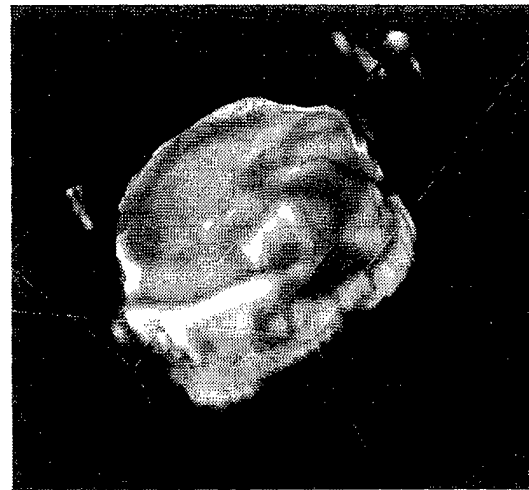


Figure 1: 3D superimposed maps of vascular volume and H&E staining obtained from a tumor.

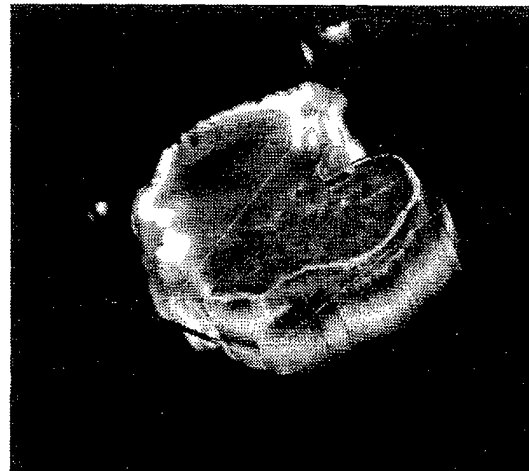


Figure 2: 3D map of vascular permeability and VEGF expression obtained from the tumor shown in Figure 1.

**DISCUSSION:** The 3D multi-modal volume rendering provides unique information about the relationship between vascular volume, permeability and histology maps. The rendering algorithm preserves the color encoding in the histology maps and uses gray scales for MR maps, which allows us to simultaneously display both images and navigate through them for direct comparison of functional parameters of tumor vasculature with cellular characteristics of the tumor. We are currently investigating other approaches to combine multiple volumes, such as using the separate color channels for MR maps and histology intensity data with suitable color space transformations to identify regions of spatial correspondence.

## References

1. Solaiyappan, M., et al., *Proc. ISMRM*, 56, 1998.
2. Takahashi, Y., et al., *Canc. Res.*, 55, 3964, 1995

**Acknowledgments:** This work was supported by USAMRMC grant DAMD17-96-1-6131 and NIH Grant 1R01 CA73850. We thank Mr. G. Cromwell for transplanting the tumors. We gratefully acknowledge the support of Dr. E. A. Zerhouni.

**Comparison of Vascular Volume and Permeability for Tumors Derived from Metastatic Human Breast Cancer Cells with and without the Metastasis Suppressor Gene nm23**

Z. M. Bhujwalla, D. Artemov, M. Solaiyappan, D. Mao and J. P. Backer<sup>†</sup>

Oncology Section - Division of MR Research, Dept. of Radiology, The Johns Hopkins University School of Medicine, Baltimore, MD 21205; <sup>†</sup>Dept. of Microbiology & Immunology, New York Medical College, Valhalla, NY 10595.

**INTRODUCTION:** Our ongoing studies are directed towards understanding the role of vascularization and permeability in metastatic dissemination. The nm (nonmetastatic)23 gene is related to suppression of metastasis [1]. Two highly homologous and evolutionarily conserved nm23 genes, nm23-H1 and nm23-H2 have been identified in humans. These genes encode 17kDa proteins identified as nucleoside diphosphate kinases (NDPK) A and B. We recently detected significant differences in the metabolic and physiological characteristics of metastatic MDA-MB-435-V $\beta$  tumors containing the vector only, and less metastatic MDA-MB-435-1 $\beta$  transgene tumors containing the nm23-H1 gene [2]. Here we have used MRI to quantitate vascular volume and permeability of metastatic MDA-MB-435-V $\beta$  and less metastatic MDA-MB-435-1 $\beta$  tumors, to further understand the impact of the loss of the nm23 gene on tumor vascular characteristics. We have related multi-slice MRI data of vascular volume and permeability to maps of VEGF expression and cellular morphology.

**METHODS:** Multi-slice experiments, relaxation rates ( $T_1^{-1}$ ) were obtained by a saturation recovery method combined with fast  $T_1$  SNAPSHOT-FLASH imaging (flip angle of 50°, echo time of 2 msec). Images of 8 slices (slice thickness of 1mm) acquired with an in-plane spatial resolution of 250 $\mu$ m (64x64 matrix, 16mm field of view, NS=16) were obtained for 3 relaxation delays (100msec, 500msec, and 1sec) for each of the slices. Thus, 64x64x8  $T_1$  maps were acquired within 7 minutes. An  $M_0$  map with a recovery delay of 7s was acquired once at the beginning of the experiment. Images were obtained before i.v. administration of 0.2ml of 60 mg/ml albumin-GdDTPA in saline (dose of 500mg/kg) and repeated every 8 minutes, starting 10 minutes after the injection, up to 32 minutes. Relaxation maps were reconstructed from data sets for three different relaxation times and the  $M_0$  data set on a pixel by pixel basis. At the end of the imaging studies, the animal was sacrificed, 0.5 ml of blood was withdrawn from the inferior vena cava, and tumors were marked for referencing to the MRI images, excised, and fixed in 10% formalin for sectioning and staining. Vascular volume and permeability product surface area (PS) maps were generated from the ratio of  $\Delta(1/T_1)$  values in the images to that of blood. The slope of  $\Delta(1/T_1)$  ratios versus time in each pixel was used to compute (PS) while the intercept of the line at zero time was used to compute vascular volume (V). Thus, vascular volumes were corrected for permeability of the vessels. Adjacent 5 $\mu$ m thick histological sections obtained at 500  $\mu$ m intervals through the tumor were stained with hematoxylin eosin or for VEGF distribution using a rabbit polyclonal anti-VEGF antibody (Santa Cruz Biotechnology, Santa Cruz, CA). Sections were digitized with a Sanyo CCD camera attached to an optical microscope. 3-D reconstruction of both MRI and histological sections was performed using the Clinical Microscope Visualization software we are developing as a research tool for our studies. The software system is developed around our Silicon Graphics Inc. Octane Workstation, taking full advantage of hardware accelerated graphics capabilities such as 2- and 3-D Textures to provide interactive rendering results.

**RESULTS:**

Vascular Permeability

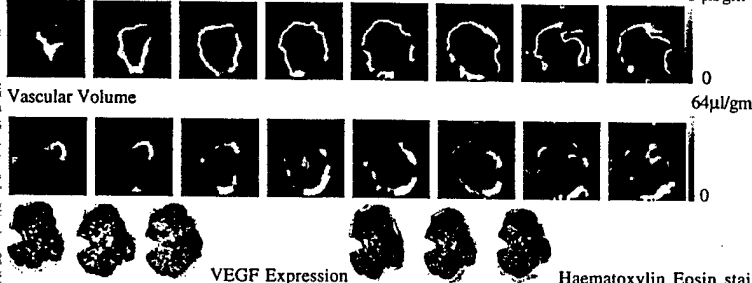


**FIGURE 1**

(PLEASE CHECK):

- The authors certify that any work with human or animal subjects complies with the guiding policies of their national or institutional regulatory bodies.
- Not applicable.
- The authors have submitted this abstract electronically in addition to this form.
- Prefer Oral Presentation but willing to present as a poster
- Video required (available only for Oral Presentations)
- Prefer Poster but willing to make Oral Presentation
- Poster only

For office use only

Control #

TOPIC CATEGORIES  
(PLEASE FILL IN BOTH):

Enter "old" category number: \_\_\_\_\_

Enter "new" category numbers: \_\_\_\_\_

For office use only

Program #

A \_\_\_\_\_ / B \_\_\_\_\_ / C \_\_\_\_\_ / D \_\_\_\_\_ / E \_\_\_\_\_

To be notified of abstract status, the name and complete mailing address of the first author must be typed below:

Name: Z. M. Bhujwalla \_\_\_\_\_  
Rm 208C Traylor Bldg., 720  
Address: Rutland Ave., JHU SOM, Radiology

Baltimore, MD 21205 Postal Code: \_\_\_\_\_ Country: USA

Tel.: (410)-955-9698 \_\_\_\_\_

FAX: (410)-614-1948 \_\_\_\_\_

E-mail: zaver@mri.jhu.edu \_\_\_\_\_

Typical multi-slice data of vascular volume and permeability together with histological sections stained with haematoxylin and eosin and VEGF expression, obtained from an MDA-MB-435-1 $\beta$  tumor (tumor volume = 370 mm $^3$ ) are shown in Figure 1. The corresponding 3D reconstructed maps of (a) vascular volume (b) vascular permeability (c) Haematoxylin Eosin stained map and (d) VEGF expression are shown in Figure 2.

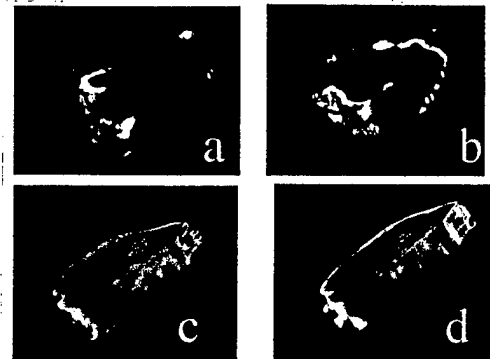


**FIGURE 2**

The table below shows Mean  $\pm$  S.E.M. values of vascular volume and permeability obtained for a group of tumors; n = number of animals.

Tumor Type	Tumor Volume in mm $^3$	Vascular Volume ( $\mu$ l/gm)	Vascular Permeability ( $\mu$ l/gm-min)
V $\beta$ (n=6)	349	6.7 $\pm$ 1.2	0.39 $\pm$ 0.15
1 $\beta$ (n=6)	460	9.04 $\pm$ 1.8	1.03 $\pm$ 0.3*

\* p < 0.05, unpaired t-test

No significant differences in vascular volumes averaged over the whole tumor were detected between the metastatic MDA-MB-435-V $\beta$  and the less metastatic MDA-MB-435-1 $\beta$  transgene tumor. Thus average vascular volume does not appear to be affected by the loss of the nm23 gene. Significant differences, however, were detected for vascular permeability; the less metastatic MDA-MB-435-1 $\beta$  tumors were significantly more permeable compared to the V $\beta$  tumors. These values, however, include regions of necrosis. We are currently using our interactive software to analyze vascular volume and permeability of viable regions only. A visual comparison of VEGF expression in histological sections obtained from a tumor in the V $\beta$  group (0.3  $\mu$ l/gm-min) and the most permeable tumor in the 1 $\beta$  group (1.6  $\mu$ l/gm-min) showed no significant differences in VEGF staining intensity. This suggests that the presence of nm23 may alter vascular permeability independently of VEGF expression. Most of these tumors (V $\beta$  and 1 $\beta$ )

exhibit necrosis (see histological sections in Fig. 1 and 2) and therefore must contain stressed environments. Since the stress response of normal tissues is also characterized by increased permeability (3), our working hypothesis is that loss of the nm23 gene in metastatic breast cancer may result in a reduction of stress induced increase of vascular permeability.

**REFERENCES:** 1. Steeg, P. et al., JNCL, 80, 1988; 2. Bhujwalla et al., ISMRM Proceedings, 1998; 3. Maeda, H. et al. Biochem., 67, 1998.

**ACKNOWLEDGEMENTS:** This work is supported by the Komen Foundation and USAMRMC grant DAMD17-96-16131. We thank Mr. G. Cromwell for maintaining the cell lines. We thank Dr. E. A. Zerhouni for his support.

The Anti-Inflammatory Agent Indomethacin Reduces the Malignant Phospholipid Phenotype of Metastatic Human Breast Cancer Cells

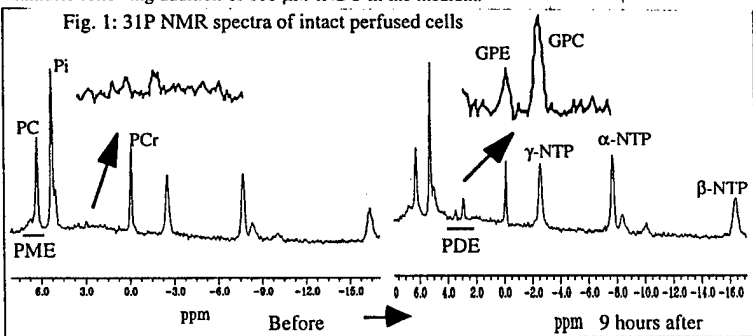
Z. M. Bhujwalla, K. Natarajan, E. O. Aboagye, N. Mori, D. Artemov, U. Pilatus and V. P. Chacko.

Oncology Section - Division of MR Research, Dept. of Radiology, The Johns Hopkins University School of Medicine, Baltimore, MD 21205.

**INTRODUCTION:** We recently demonstrated that human mammary epithelial cells exhibit alterations in choline phospholipids with progression to the malignant phenotype (1). The most striking changes detected in proton spectra of cell extracts were an increase of glycerophosphocholine (GPC) relative to phosphocholine (PC) for the non-malignant lines and a progressive increase in PC levels with increasingly malignant phenotype. Further evidence of the role of the choline phospholipid compounds in breast cancer progression also comes from our studies of the metastatic human breast cancer line MDA-MB-435 following transfection with the non metastatic gene nm23; lowly metastatic tumors derived from nm23 transfected cells exhibited a significantly higher phosphodiesters (PDE) relative to phosphomonoesters (PME) compared to control metastatic tumors derived from cells transfected with vector only (2). Several studies have shown that the nonsteroidal anti-inflammatory agent indomethacin (INDO) can inhibit the invasive and metastatic behaviour of human breast cancer cells. Our question here was: Does treatment of highly malignant breast cancer cells with INDO alter the PDE/PME ratios consistent with predictions from our observations of the 'invasive/metastatic phospholipid phenotype'? We studied intact human MDA-MB-435 (wild type) breast cancer cells immobilized on microcarrier beads in our NMR cell perfusion system and also obtained proton spectra from extracts of cells growing in tissue culture flasks.

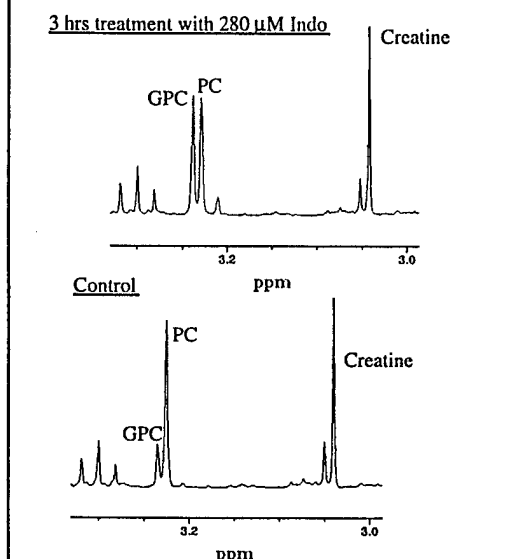
**METHODS:** For the  $^{31}\text{P}$  NMR experiments of intact cells, 2 - 3 ml of  $10^7$  MDA-MB-435 breast cancer cells/ml of microcarrier beads were transferred into a 10 mm screw cap NMR tube. The cells were continuously perfused at a rate of 1.5 ml/min with growth medium consisting of RPMI supplemented with 10% FCS and containing 15 mM HEPES. The medium was equilibrated with 95%  $\text{O}_2$  and 5%  $\text{CO}_2$ .  $^{31}\text{P}$  NMR spectra (45° flip angle; 1 sec repetition time; na=4000) were obtained at 80 min intervals from these intact isolated perfused cells, prior to, and following treatment with 100  $\mu\text{M}$  INDO. Parallel control experiments of untreated cells were performed over the same time period. For the 1H NMR extract studies, cells were cultured in supplemented DMEM without HEPES but with bicarbonate buffer. Cells were fed with medium alone or medium plus 280  $\mu\text{M}$  INDO 3 hours prior to extraction and used at 70-80% confluence. Perchloric acid (PCA) extracts were obtained from approximately  $10^8$  cells. Cells were trypsinized and the action of trypsin was blocked by cold serum containing growth medium. Cells were then washed twice with normal saline and extracted with ice cold 8% (v/v) PCA. Supernatants were neutralized with 3M  $\text{K}_2\text{CO}_3$ /1M KOH, lyophilized, and resuspended in  $\text{D}_2\text{O}$ . Trimethylsilyl propionate (TSP) was used as internal standard. Fully-relaxed water-suppressed proton spectra of the extracts were acquired on a 11.7T Bruker 500MHz NMR spectrometer with a 5 mm probe. Spectral acquisition parameters were 30° flip angle, SW = 6000 Hz, 4.7 sec repetition time, 32 K block size, and number of scans = 512.

**RESULTS:** Treatment with INDO resulted in a significant increase of GPC and glycerophosphoethanolamine (GPE); control spectra obtained over a similar time period showed no changes in the PDE region. The increase in GPC (shown at 9 hrs in Figure 1) was evident within 80 minutes following addition of 100  $\mu\text{M}$  INDO in the medium.



Proton spectra obtained from cell extracts of MDA-MB-435 cells (Figure 2) also showed a significant increase of GPC relative to PC following incubation with 280  $\mu\text{M}$  INDO for 3 hrs. There were no significant differences in cell viability for the treated and control flasks.

Figure 2:  $^1\text{H}$  NMR spectra of MDA-MB-435 cell extracts



**DISCUSSION:** Treatment with INDO altered the phospholipid profile of highly malignant breast cancer cells towards a less malignant phenotype. Recently, we have also detected similar changes following INDO for MDA-MB-231 cells. Since INDO is a cyclooxygenase (COX) inhibitor, these results suggest that the altered phospholipid profile of highly malignant cells may partly be related to alterations of the COX-1/COX-2 pathway. COX-1 and COX-2 are rate-limiting enzymes which convert arachidonic acid to prostanooids; COX-2 is an inducible enzyme and its constitutive expression has been shown to enhance the invasive and metastatic behaviour of colorectal cancer cells (3). Our results provide direct evidence for the first time that the phospholipid peaks in NMR spectra of breast cancer cells can be modulated by a cyclooxygenase inhibitor and indicate the utility of NMR in understanding the role of anti-inflammatory agents in cancer treatment.

**REFERENCES:** 1. Aboagye, E. and Bhujwalla, Z. M. Cancer Research, 1999; 2. Bhujwalla et al., ISMRM Proceedings, 1998; 3. Tsuji, M. et al., PNAS, 1997.

**ACKNOWLEDGEMENTS:** This work is supported by the Komen Foundation and USAMRMC grant DAMD17-96-16131. We thank Dr. H. Shim for her assistance with the cell perfusion and Mr. G. Cromwell for maintaining the cell lines. We thank Dr. R. J. Gillics for useful discussions.

(PLEASE CHECK):

- The authors certify that any work with human or animal subjects complies with the guiding policies of their national or institutional regulatory bodies.
- Not applicable.
- The authors have submitted this abstract electronically in addition to this form.
- Prefer Oral Presentation but willing to present as a poster
- Video required (available only for Oral Presentations)
- Prefer Poster but willing to make Oral Presentation
- Poster only

For office use only
Control #

TOPIC CATEGORIES  
(PLEASE FILL IN BOTH):

Enter "old" category number:

Enter "new" category numbers:

A. 3 / B. 3 / C. 15 / D. 8 / E. 1

For office use only

Program #

To be notified of abstract status, the name and complete mailing address of the first author must be typed below:

Name: Z. M. Bhujwalla

Address: Dept. of Radiology

JHU School of Medicine

Rm 208C Traylor Bldg., 720, Rutla

Postal Code: 21205-MD Country: USA -nd Ave

Tel: Baltimore (410)-955-9698

FAX: (410)-614-1948

E-mail: zaver@mri.jhu.edu

# Characterization of Lactate Levels in Normal and Malignant Human Mammary Epithelial Cells

Eric O. Aboagye and Zaver M. Bhujwalla

Oncology Section - Division of MR Research, Department of Radiology,  
The Johns Hopkins University School of Medicine, Baltimore, MD 21205, USA

**INTRODUCTION:** Interest in lactate production by cancer cells and the role of lactate in tumors has existed since studies by Warburg in the 1930's [1]. Recently it was shown that patients with cervical cancers containing high lactate had a high risk of metastases [2]. Two possible explanations for the findings by Schwickert et al [2] are (i) A high glycolytic rate is part of the malignant invasive phenotype or (ii) High lactate is indicative of hypoxia and substrate deprivation which stimulates or promotes invasion and metastasis. Supporting the latter possibility are observations that glucose starvation, acidosis and hypoxia enhance the metastatic potential of murine tumor cells [3, 4]. In this study we have explored the first possibility for human breast cells by determining lactate levels in a series of human mammary epithelial cells (HMECs) including finite lifespan cells (normal, senescent), spontaneously or benzo(a)pyrene immortalized cells and tumor-derived cells. Our results indicate that malignant breast cancer cells produce a significantly higher amount of lactate compared to normal or immortalized HMECs.

**METHODS:** The epithelial cell lines used here have been previously described [5]. They include 184 and 48 finite lifespan cells, 184A1 and 184B5 which were derived from 184 by benzo(a)pyrene immortalization, spontaneously immortalized MCF12A cells, 185B5-erbB2 cells which were derived from 184B5 by oncogene transformation with erbB2, and the breast cancer cell lines SKBR3, MCF7, MDA-MB-231 and MDA-MB-435. Cells were cultured in MCDB 170 or DMEM/F12 with or without supplements as previously described [5]. For NMR measurements, cells were fed 24 hours prior to extraction and used at 70-80% confluence. Perchloric acid (PCA) extracts were obtained from  $10^7$  to  $10^8$  cells. Cells were trypsinized and the action of trypsin was blocked with cold serum containing growth medium. Cells were then washed twice with normal saline and extracted with ice cold 8% (v/v) PCA. Supernatants were neutralized (with 3M  $K_2CO_3$ /1M KOH), lyophilized and resuspended in  $D_2O$ . Trimethylsilyl propionate (TSP) was used as an internal standard. Fully-relaxed water-suppressed proton spectra of the extracts were acquired on a 11.7T Bruker 500MHz NMR spectrometer with a 5 mm probe. Spectral acquisition parameters were 30° flip angle, SW = 6000 Hz, 4.7 sec repetition time, 32 K block size, and number of scans = 512.

**RESULTS:** The lactate doublet was detected by  $^1H$  NMR spectroscopy of PCA extracts of cells at a resonance frequency of 1.2ppm downfield of TSP. High resolution  $^1H$  NMR spectra with comparable signal to noise, of extracts obtained from immortalized MCF12A cells and malignant MDA-MB-231 cells are shown in Figure 1. A large difference in lactate levels is apparent between these cell lines. A summary of lactate levels calculated for each cell line and normalized to cell number and cell size is shown in Fig 2. Unlike the changes reported for choline metabolites [5], no gradual increase in lactate levels was observed in our model system. All tumor-derived cells, however, showed significantly higher levels of lactate compared to the normal, immortalized and oncogene transformed cells ( $p \leq 0.05$ ). There was no correlation between lactate levels and cell doubling time measured by the MTT assay. Lactate levels in tumors derived from MCF7, MDA-MB-231 and MDA-MB-435 correlated with the levels measured in cells. In addition to lactate levels, we also analyzed total creatine (at 3.04 ppm) for these lines (shown in Fig. 3). With the exception of the most malignant cell line, MDA-MB-435, all cell lines showed low levels of total creatine.

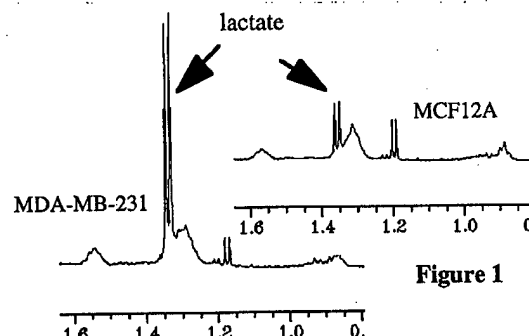


Figure 1

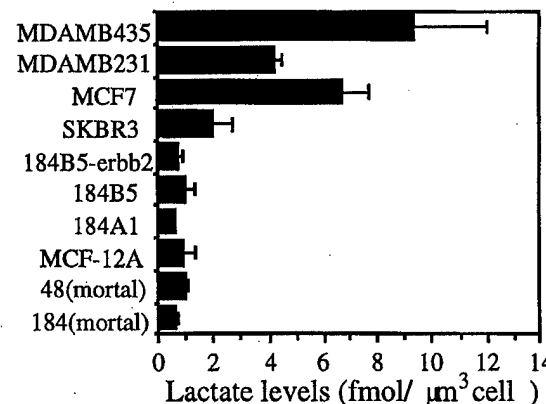


Figure 2: Lactate levels for cell lines representing various stages of malignant progression of HMECs. Bars represent  $\pm$  S.E.M. There was a statistically significant difference in lactate ( $p \leq 0.05$ ) for finite lifespan and immortalized versus tumor-derived cells ( $1\text{fmol}/\mu\text{m}^3 = 1\text{mM}$ ).

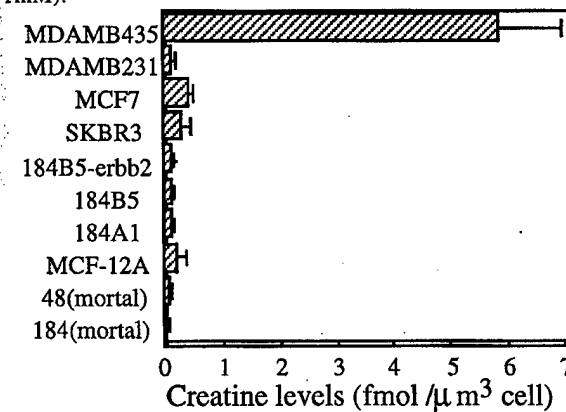


Figure 3: Creatine levels in a panel of cell lines representing various stages of malignant progression of HMECs. Bars represent  $\pm$  S.E.M.

**DISCUSSION:** Our results demonstrate that, unlike choline levels which gradually increased with malignant progression in this model system [5], lactate levels remained low in all normal, immortalized and oncogene transformed cells. Consistent with published data for human breast tumors versus uninvolved breast tissues [6], lactate levels were significantly higher for the malignant cell lines. Following malignant transformation, however, there appeared to be no further dependence of lactate levels with increasing invasive/metastatic behaviour (e.g. MCF-7 vs MDA-MB-231). Increased lactate levels may be due to increased expression of glycolytic enzymes such as lactate dehydrogenase and/or of glucose transporters. These data suggest that the increase in lactate levels, characteristic of most tumors, occurs late in carcinogenesis. Our data also demonstrate that, with the exception of the MDA-MB-435 line, mammary epithelial cells do not show an increase in creatine/phosphocreatine levels with malignant transformation. Given the importance of lactate levels in the diagnosis of cancer and prediction of tumor response, the results obtained here support further studies to understand the mechanism of regulation of lactate in breast epithelial cells.

**REFERENCES:** 1. Warburg, O., 1931; 2. Schwickert, G., et al., Cancer Res., 55, 4757, 1995; 3. Schlappack, O.K., et al., Brit. J. Cancer, 692, 1991; 4. Young, S.D. et al., PNAS., 85, 9533, 1988; 5. Aboagye and Bhujwalla, Cancer Res., 1, 1999; 6. Gribbestad, I.S. et al., Anticancer Res., 13, 1973, 1993.

**ACKNOWLEDGEMENTS:** We thank Dr. Martha Stampfer, Lawrence Berkeley Laboratories, for the normal and immortal 184 cell lines and gratefully acknowledge the assistance of Dr. V. P. Chacko. This work was supported by USAMRMC Grant DAMD17-96-16131.